[redacted]

68p

NASA TECHNICAL MEMORANDUM

NASA TM X-970

NASA TM X-970

X64 14566

(NASA-TM-X-97.) FREE-FLIGHT INVESTIGATION OF REENTRY HEAT TRANSFER AND ABLATION B. Rashis, et al (NASA) Jun. 1964 68 p

N72-73344

Unclas
00/99 32185

UNCLASSIFIED

TO

By Authority of TD 22-235 Date 6-7-72

FREE-FLIGHT INVESTIGATION OF REENTRY HEAT TRANSFER AND ABLATION AT VELOCITIES UP TO 22,500 FEET PER SECOND (U)

by Bernard Rashis and Brian J. O'Hare

Langley Research Center
Langley Station, Hampton, Va.

NATIONAL AERONAUTICS AND SPACE ADMINISTRATION • WASHINGTON, D. C. • JUNE 1964

[redacted]

[redacted]

FREE-FLIGHT INVESTIGATION OF REENTRY HEAT TRANSFER AND ABLATION AT VELOCITIES UP TO 22,500 FEET PER SECOND

By Bernard Rashis and Brian J. O'Hare

Langley Research Center
Langley Station, Hampton, Va.

NATIONAL AERONAUTICS AND SPACE ADMINISTRATION

[redacted]

[redacted]

FREE-FLIGHT INVESTIGATION OF REENTRY HEAT TRANSFER AND ABLATION AT VELOCITIES UP TO 22,500 FEET PER SECOND*

By Bernard Rashis and Brian J. O'Hare
Langley Research Center

SUMMARY

~~14566~~

A fifth propulsion stage incorporating a spherical rocket motor was added to the NASA Scout launch vehicle. This spherical rocket motor and its associated experiment envelope comprised the reentry vehicle which weighed 300 pounds prior to firing and provided an additional velocity increment of 5,000 fps. Measurements of heat transfer were obtained for a reentry velocity of 22,500 fps over an altitude range of 390,000 feet to 200,000 feet. During this reentry period, the penetration angle was -15° and the velocity package had a ballistic coefficient of approximately 150 lb/sq ft. Ablation measurements were obtained at velocities and altitudes that ranged from 22,000 fps at an altitude of approximately 180,000 feet to 4,200 fps at an altitude of approximately 60,000 feet.

Heat-transfer measurements were obtained with the use of a thin-wall inconel calorimeter to which thermocouples were attached. Ablation measurements were obtained with the use of a Teflon nose cap in which ablation sensors were imbedded. The Teflon was exposed to the airstream when the inconel cap melted off. In addition to these primary measurements, the angular rates and linear accelerations were measured. Also, the received signal strength from the telemeter transmitters and the forward and reflected transmission line voltages were measured.

Dynamic motion data indicated that during the test period the flight payload underwent large variations in angles of attack. A technique was developed which enabled the prediction of the heating with angle of attack. The predicted Teflon ablation at the center of the nose, when corrected for angle of attack, was 0.185 inch as compared with a predicted value of 0.1877 inch. The reentry blackout boundaries were determined from the changes in signal strength and the associated loss in the performance of the antennas.

author

INTRODUCTION

The Langley Research Center is currently conducting flight investigations at supercircular velocities for the purpose of advancing the state of the art

*Title, Unclassified.

[redacted]

of manned lunar technology with special emphasis on the problems of heating and thermal protection. The investigations will provide checks for the accuracy of analytical procedures and also assist the user in the interpretation of results obtained in ground research facilities where the models used are generally small, the velocities generally lower, and the test environment does not duplicate that encountered during reentry at supercircular velocities.

As an initial step in this investigation, a velocity package which incorporated a spherical rocket motor was added to the NASA Scout launch vehicle. The overall vehicle, known as the five-stage reentry Scout, is capable of launching relatively large payloads to supercircular reentry velocities and has a wide range of altitude and penetration angle. For the present flight, the velocity package, which weighed approximately 300 pounds, increased the maximum velocity capability for this Scout model to 26,500 fps.

The planned and actual impact location of the velocity package was near enough to Bermuda to permit use of radar at Bermuda, optical tracking equipment, and ground-based telemeter stations. Radio-telephone links between the launch site at the NASA Wallops Station and the Bermuda stations provided satisfactory means of communication and coordination.

The primary measurements, heat transfer and ablation rates, were obtained in two phases. The heat-transfer measurements were obtained by using a thin-wall inconel nose cap to which thermocouples were attached. The cap provided about 25 seconds of measurable temperature rise rates before melting. During this period the payload velocity was about 22,500 fps. The altitude ranged from approximately 400,000 feet to 200,000 feet.

The ablation measurements were obtained by using a Teflon nose cap in which ablation sensors were imbedded. The Teflon was exposed to the airstream when the inconel cap melted. During the ablation period, the payload velocity varied from about 22,000 fps to about 4,000 fps, and the altitude varied from approximately 180,000 feet to 60,000 feet.

In addition to these primary measurements, the angular rates and linear accelerations of the vehicle and payload were measured. The received signal strength from the telemeter transmitters and the forward and reflected transmission line voltages also were measured. These measurements indicated the telemeter blackout region boundaries for the flight test.

The purpose of this paper is to present the results and analysis of the heat-transfer and ablation measurements. Since analysis of the vehicle and payload dynamic motion data is beyond the scope of this paper, only the results directly pertinent to this paper are presented. The information on the blackout region is also presented, but these data should be considered as applicable strictly to this flight test.

[redacted]

SYMBOLS

a_l	longitudinal acceleration, g units
a_n	normal acceleration, g units
a_t	transverse acceleration, g units
h	heat-transfer coefficient, Btu/(sq ft)(sec)($^{\circ}$R)
$\bar{h}$	integrated average heat-transfer coefficient, Btu/(sq ft)(sec)($^{\circ}$R)
h_{eff}	effective heat of ablation, Btu/lb
H	enthalpy, Btu/lb
l	ablated length, in.
M	free-stream Mach number
N_{Pr}	Prandtl number
q	heating rate, Btu/(sq ft)(sec)
r_c	radius of curvature of nose, ft
r_{eff}	effective radius
r_n	normal distance from center line to corner (fig. 16), ft
s	distance measured from center of nose face along outside of skin, ft
T	temperature, $^{\circ}$R
t	time, sec
V	velocity, fps
α	angle of attack, deg
β	stagnation velocity gradient
μ	viscosity, lb/ft-sec
ρ	density, lb/cu ft
ϕ	angle of rotation (sketch 1 in appendix), deg

[redacted]

Subscripts:

aero	aerodynamic
as	aerodynamic stagnation point
aw	adiabatic wall
F	flight
f	forebody
gc	geometric center point of nose face
hs	hemisphere
o	sea level
s	stagnation
w	wall
∞	free stream

DESCRIPTION OF PAYLOAD AND VEHICLE

Velocity Package

The velocity package was a blunt cone approximately 3 feet in length, having a blunt face with $r_n/r_c = 1/3$ and a 9° half-angle conical forebody. The major components of the velocity package were the inconel calorimeter cap, the Teflon nose cap, the Teflon covered conical afterbody, the telemetry container, and the 17-inch spherical rocket motor. Figure 1 shows the details of the velocity package configuration and the location of the major components. The velocity package is also referred to as the payload.

Inconel Calorimeter

A thin wall inconel calorimeter, 0.055 inch thick on the nose and 0.029 inch thick on the afterbody, was used to obtain heat-transfer measurements. The inconel cap was fastened to the front end of a magnesium sleeve. The rear end of the sleeve was threaded to the cylindrical portion of the Teflon nose cap. The magnesium sleeve also supported a frangible shield of aluminum-covered fiber glass located between the inconel and Teflon nose caps. The frangible shield and magnesium sleeve were designed to remain in place until the entire inconel cap melted off the nose. The frangible shield prevented the heated inconel from damaging the thermocouple leads extending from the inconel and also prevented the molten inconel from damaging the front face of the Teflon cap.

Teflon Nose Cap

The Teflon nose cap, which became exposed to the airstream when the inconel cap melted, was machined from a single piece of Teflon and was backed, for additional strength, by a 1/8-inch-thick sheet of fiber glass that was bonded to the Teflon. The Teflon nose was threaded to a magnesium ring which in turn was threaded to the front end of the conical forebody.

Conical Forebody

The conical forebody consisted of a magnesium substructure that was covered by a 0.3-inch-thick shield of Teflon material. The substructure was made up of three 0.06-inch-thick magnesium sections that were held together by two fiber glass rings. The forward and aft magnesium sections were used as antennas. The fiber glass rings served as electrical insulators for the antenna sections. A magnesium flange attached to the center magnesium section served as a holding flange for the telemeter canister. The velocity package was isolated from the rest of the vehicle by a third fiber glass ring fastened to the rear of the aft antenna section. This ring also had a machined flange to which the 17-inch rocket motor was attached. The entire substructure was assembled as a unit prior to being covered by Teflon. The Teflon, which does not attenuate the radio transmissions, was constructed as a single piece and bonded to the substructure with epoxylite cement.

Telemetry

The telemetry instrumentation in the velocity package was an FM/FM system of 14 standard Inter-Range Instrumentation Group (IRIG) subcarrier frequency data channels which modulated two separate radio-frequency (RF) carrier links to ground receiving stations. One RF link telemetered data as it occurred (real-time data transmission); the other RF link telemetered the same data but the transmission was delayed approximately 56 seconds by means of a continuous loop tape recorder onboard the velocity package.

Normally, only one transmission system is required but a study of the trajectory indicated that a period of radio blackout (ionization at the antennas) would occur; therefore, in order that the data not be lost during this blackout period, the data from the second RF link were delayed for a period of time greater than the blackout duration. Thus, an overlay of the real-time data from the two transmissions to the ground stations provided continuous data for the entire flight even though reception was lost during ionization.

One of the subcarrier channels was a coded timing system which insured that the real-time data were accurately located on both the direct and delayed ground station records. In addition, because of variations in the tape speed of the recorder, a compensating signal subcarrier channel was included. With this signal recorded on the flight tape, the tape playbacks automatically compensate for variations in the tape speed.

Seven of the subcarrier channels were utilized to provide continuous in-flight measurements of the velocity package performance and attitude. The instruments consisted of three rate gyros (pitch, yaw, and roll) and four linear accelerometers (two longitudinal, one transverse, and one normal). Three of the channels, which were commutated, provided the thermocouple measurements. A fourth commutated channel provided the measurements of the ablation sensors. With the exception of the thermocouples and ablation sensors, the telemeter electronics and instruments were contained in a "sealed from the atmosphere" container.

Spherical Rocket Motor

The spherical rocket motor incorporated in the velocity package was a 17-inch-diameter Cetus-I. This motor has an internal nozzle constructed of graphite, an average thrust of approximately 860 pounds, and a burning time of approximately 43 seconds. The overall dimensions, the pertinent details, and some performance values for the motor are given in figure 2. In the nomenclature of this report, this motor is called the fifth stage.

Adaptor Connecting Fourth and Fifth Stages

An adaptor or transition section was used to connect the thrust face of the Scout fourth stage to the fifth-stage motor nozzle. Some of the instrumentation used prior to fifth-stage ignition was housed in this adaptor section. A C-band radar beacon with antennas, fifth-stage ignition batteries, and some instrumentation batteries were among the items carried in this section. Figure 3 shows the pertinent details of this section and the layout of the included apparatus; figure 4 shows the assembled velocity package and adaptor. The weights of the various components of the velocity package and adaptor are given in table I.

Scout Booster System

The Scout booster system consists of four stages of solid-propellant rocket motors. The configuration details and nomenclature are given in figure 5. The system is capable of three basic types of trajectories: orbital, high-altitude near-vertical probes, and ballistic reentry. The present flight test utilized the ballistic reentry capability.

The first-stage motor, Algol, is 30 feet long, 40 inches in diameter, and develops 115,000 pounds of thrust. It is fin stabilized and controlled in flight by jet vanes and by aerodynamic controls on the fin tips. The launcher connections, umbilical checkout and launch firing cable connections, and the hydraulic control system for the fins and jet vanes are located at the base of this stage designated base A in figure 5.

The second-stage motor, Castor, is 20 feet long, 30 inches in diameter, and develops approximately 50,000 pounds of thrust. The second stage is connected

[redacted]

to the first stage by two coupled sections designated transition B. These sections contain a reaction control system for the vehicle, a device to separate the second stage from the first stage, and components for the destruct system.

The third-stage motor, Antares, is 10 feet long, 30 inches in diameter, and develops approximately 14,000 pounds of thrust. The third stage is connected to the second stage by two coupled sections designated transition C. The transition sections provide housing for the hydrogen peroxide reaction control motors, telemetry equipment, the destruct system, and a separation device.

The fourth-stage motor, Altair, is 6 feet long, 18 inches in diameter, and develops 3,000 pounds of thrust. The fourth stage is joined to the third stage by a section designated transition D. This transition section houses the guidance system, the main guidance controls, a separation device, and a spin-up system. The fourth stage is spin stabilized prior to firing; thus, no guidance or control system is required for this stage.

A jettisonable nose cone over the velocity package and heat shields over the third- and fourth-stage motors provided aerodynamic streamlining and acceptable temperature environment during the exit portion of the flight. Figure 6 shows the overall vehicle just prior to launch.

TRAJECTORY AND TRAJECTORY MEASUREMENTS

Trajectory

The vehicle was launched from the NASA Wallops Station at an azimuth of 129° and an elevation angle of approximately 81°. After first-stage burnout, the vehicle coasted to an altitude of 130,000 feet, at which time the second stage was ignited and the third-stage heat shield jettisoned. The vehicle coasted over apogee and upon reaching a flight-path angle of -6°, the third stage was ignited. Just prior to third-stage ignition, the fourth-stage heat shield was jettisoned. Some 22 seconds after third-stage burnout, the fourth stage was ignited. Prior to this event, the spin motors were ignited and the fourth stage and velocity package spun. Approximately 23 seconds after fourth-stage ignition, the fifth stage ignited. The fifth-stage ignition was some 16 seconds earlier than planned.

From the onboard instrumentation records, it was noted that the fourth-stage cut-off (as indicated by the thrust accelerometer) was followed by large rate gyro oscillations. These oscillations lasted for 2.2 seconds, at which time the fifth stage ignited. Studies made of these oscillations indicated that if a suddenly applied moment had occurred in a plane oriented midway between the pitch and yaw planes, oscillations such as those measured would have resulted. A moment, as described above, could have resulted from a rupture in the fourth-stage-motor case. Such a rupture would result in premature cut-off of the fourth-stage thrust.

The failure resulted in a maximum velocity approximately 4,000 fps lower than that anticipated. Furthermore, the oscillations initiated were not damped

[redacted]

out by the beginning of the data period. As a consequence, the payload reentry occurred at angles of attack ranging from 10° to 40°. Onboard instrumentation, however, was not adversely affected and the increased aerodynamic forces resulting from the high angles of attack were not great enough to cause damage to the spacecraft structure. Although the planned maximum velocity of 26,500 fps was not achieved, the primary objectives of heat-transfer and ablation measurements were successfully obtained at a reentry velocity of 22,500 fps.

Trajectory Measurements

The trajectory parameters were obtained from ground-based radar installations at both Wallops Island, Va., and Bermuda, from a ground-based optical tracking installation at Bermuda, and from a dynamic trajectory analysis developed at the Langley Research Center, which incorporated as inputs the telemeter measurements of angular rates and linear accelerations. The telemeter information was received by ground stations at Wallops Island and at Bermuda. In addition, telemetry receiving equipped ships were stationed along the 129° azimuth approximately 10 international nautical miles and 150 international nautical miles downrange of the preflight-calculated payload impact point.

The payload motion measurements which were used as inputs for the dynamic trajectory analysis are shown in figures 7 and 8. The gyro measurements are shown in figure 7. The linear accelerometer measurements, referenced to the payload center of gravity, are shown in figure 8. Figures 7 and 8 cover the time period from fifth-stage burnout to the end of the data period, $t = 460$ seconds.

The optical tracking installation at the Bermuda station used a ballistic camera with a 6-inch-diameter f/5.6 lens. Time histories of the payload azimuth and elevation (relative to the optical tracking site) were obtained by this equipment. Although these measurements in themselves did not provide a trajectory, they enabled, along with some of the radar tracking data, a fix for the trajectory computed by the dynamic trajectory analysis. The closeness of this fix is indicated by figure 9. The optical tracking measurements of azimuth as a function of flight time are shown as the circular symbols in figure 9(a). The measurements of elevation as a function of flight time are shown as the square symbols in figure 9(b). The solid-line curves which were computed from the dynamic trajectory analysis fit the data closely.

Figure 10 shows the altitude-range measurements and calculations from lift-off to splash. The Wallops FPS-16 radar provided coverage from lift-off to the fourth-stage ignition. This coverage was assisted by a C-band beacon, located in transition D, which operated until the fourth stage separated from the third stage. The Bermuda FPS-16 radar provided coverage from about 8 seconds after third-stage burnout until fifth-stage ignition. After fifth-stage ignition, the Bermuda FPS-16 radar tracked the burned-out fourth stage. The Bermuda FPS-16 radar was also assisted by a C-band beacon located on the adaptor connecting the fourth and fifth stages. This adaptor was fixed to the fourth stage. The Wallops SPANDAR provided coverage (skin tracked) for about 37 seconds after fourth-stage ignition. However, the SPANDAR data are questionable

[redacted]

because of the low signal-to-noise ratio. The results of the dynamic trajectory analysis are shown as the solid-line curve. The preflight-calculated trajectory from lift-off to fourth-stage ignition is shown as the dashed-line curve.

The altitude and velocity time histories are shown in figures 11 and 12, respectively. For the portion of the trajectory up to fourth-stage ignition, the values of velocity were obtained from differentiation of the tracking data. After fourth-stage ignition, the values of velocity and altitude and the flight-path angles were computed from the dynamic trajectory analysis. For comparison, the preflight-calculated trajectory from lift-off to fourth-stage ignition is shown as a dashed line in figures 11 and 12.

TEST REGIME AND ENVIRONMENT

Figure 13 shows the variation of altitude with velocity for the flight test regime. The heat-transfer-data period denotes the regime during which the inconel calorimeter experienced measurable temperature rise rates. The velocity during this period changed from 21,050 fps at $t = 410$ seconds to 22,338 fps at $t = 435$ seconds for altitudes of 389,350 feet and 199,919 feet, respectively. During the period $t = 435$ seconds to $t = 438$ seconds, the inconel calorimeter cap was being melted.

The ablation test period denotes the regime during which the Teflon nose cap was exposed and undergoing ablation. The velocity during this period changed from 22,222 fps at $t = 438$ seconds to 4,204 fps at $t = 460$ seconds for altitudes of 176,648 feet and 57,825 feet, respectively.

Density-altitude and temperature-altitude measurements from sea level to an altitude of 94,000 feet were obtained by a radiosonde balloon. Density-altitude measurements from 120,000 feet to 210,000 feet were obtained by an Arcas sounding rocket. Both the radiosonde and Arcas were launched from Bermuda sites.

Figure 14 shows the free-stream density variation for the test altitudes. The square symbols are the measurements obtained with the radiosonde, and the circular symbols are the measurements obtained with the Arcas. The solid line represents the 1962 U.S. standard atmosphere (ref. 1). The dashed line indicates the fairing and assumed extrapolation of the measurements.

Figure 15 shows the free-stream temperature variation with the test altitudes. The square symbols are the radiosonde measurements, and the circular symbols are the values derived from the Arcas density measurements. The method used is described in reference 2. The 1962 U.S. standard atmosphere is shown as the solid line. The derived temperatures are only slightly less than the standard values and exhibit essentially the same trend.

[redacted]

TEMPERATURE AND ABLATION MEASUREMENTS

Temperature Measurements

Figure 16 shows the overall dimensions of the inconel cap, the thermocouple locations, and the inconel thickness at the thermocouple locations. The surface of the nose cap was polished to 5 microinches as determined from measurements made with an interference microscope. Nineteen thermocouples of No. 30 chromel-alumel wire were attached to the cap, and the two wires of each thermocouple were individually spot welded to the inside surface of the inconel cap. During flight, three standard voltages were commutated along with the thermocouples; these voltages were chosen to be equivalent to the lowest, middle, and highest temperatures that the inconel skin was expected to reach. This procedure enabled in-flight calibration of the temperature measuring system. The 19 thermocouples were recorded over two telemeter channels; one channel enabled 5 readings per second at each thermocouple station and the other, 10 readings per second at each station.

Temperature data were obtained from 15 of the 19 thermocouples attached to the inside surface of the inconel calorimeter. Thermocouples 12 and 18 were "open" prior to flight, and thermocouples 11 and 16 were inoperative. (See fig. 16 for location of thermocouples.) The temperature measurements for the inside surface of the inconel calorimeter are given in table II and a typical temperature time history is shown in figure 17. The technique for the derivation of heating rates used in this paper requires that the raw temperature data be smoothed or faired. From the smoothed inside values the outside surface temperature is then computed. Figures 18(a), 18(b), and 18(c) show the computed outside surface temperatures along the inconel nose face, corners, and afterbody, respectively. Temperature rise rates were obtained from $t = 410$ seconds to about $t = 435$ seconds. The last point for a thermocouple corresponds to the time that that thermocouple opened. The individual thermocouples within a grouping are consistent as to temperature levels and rise rates. Also, the temperature levels and rise rates of the afterbody grouping are substantially less than corresponding time values of the face and corners groupings.

In figure 19, the readings of a typical thermocouple (thermocouple 7) are shown from $t = 412$ seconds to $t = 452$ seconds. A temperature rise is indicated until $t = 432$ seconds at which time the thermocouple opens. The thermocouple remains open until approximately $t = 436$ seconds, at which time relatively high temperature readings are recorded by the thermocouple. The period of high temperature readings lasts until approximately $t = 447$ seconds. At this time, which is also the time radio blackout ends, the thermocouple reads open again, and continues to read open for the remainder of the flight.

The apparent anomaly, of an open thermocouple measuring high temperatures, occurred because the thermocouple wires, were exposed to an ionized air layer when the inconel cap melted off. Although the individual wires of each of the thermocouples were separated, the ionized air acted as a shunt between them, effectively creating a thermocouple junction. At $t = 447$ seconds, ionization ended; consequently, the wires were no longer shunted and the thermocouples read open again. Since all the thermocouples exhibited the shunt effect between $t = 436$ and $t = 437$ seconds, it is believed that the inconel cap melted off during this period, and that the first open indications were due to failure of the wires at the junctions and not to the cap coming off.

Ablation Measurements

Figure 20 shows the locations of the ablation sensors. The sensors were mounted so that their longitudinal axes were perpendicular to the blunted face. Details as to the design, construction, and calibration techniques are given in reference 3. The components of the sensor are shown in figure 21. These same type sensors were also used, with very good results, in a free-flight investigation at somewhat lower speeds (ref. 4). The five sensors and three standard frequencies were commutated in sequence as inputs to a capacitance sensitive subcarrier oscillator. Since the length changes of the sensors are recorded as frequencies, the standards enabled in-flight calibration of the ablation measuring system. Each sensor was recorded five times per second during flight.

The sensors were expected to provide in-flight measurements of the rate of length change of the Teflon. With the exception of sensor 1 which became defective prior to the flight, valid initial and final length measurements were obtained. Unfortunately, no length measurements were obtained during the period of Teflon ablation. Typical of the measurements obtained are those shown in figure 22. The values shown are for sensor 2 but are essentially of the same level and trend as the values for the other sensors. The measurements cover the period from $t = 420$ to $t = 480$ seconds, the times were chosen in order to show readings after ablation ends. No readings were obtained from approximately $t = 439$ to $t = 457$ seconds. Starting at $t = 457$ seconds, readings are obtained which indicate that the sensor is undergoing a rapid change in length. This period of apparent rapid change in length lasts for approximately 3 seconds, after which the readings are essentially constant.

Since the indicated results were not understandable, a test check was made of a sensor similar to those used in the flight test. A variable resistance was placed in parallel with the sensor. The varying impedance values were indicated as frequency levels by the oscillator. This circuit is the electrical analogy of an ablation sensor, the ablating surface of which is exposed to the air. By changing the shunt resistance, varying degrees of air ionization were simulated. A schematic diagram of the circuit and the results obtained in the investigation are shown in figure 23. The impedance changes have been shown as indicated capacitance of the sensor.

For very high shunt resistances, analogous to little or no ionization, the oscillator output was essentially unchanged. As the shunt resistance was decreased, analogous to increasing air ionization, the indicated capacitance values increased above the sensor initial value of approximately 430 micromicrofarads. For a shunt resistance of approximately 5,000,000 ohms, the oscillator output is approximately 530 micromicrofarads. This capacitance value was the upper limit of the present capacitance recording range of the flight test telemetry system. Thus, if the degree of air ionization was of a level corresponding to shunt resistances less than 5,000,000 ohms, the oscillator outputs should have been offscale and hence not recorded.

The results shown in figure 23 explain the inconsistencies of the measurements shown in figure 22. The reason no sensor measurements were recorded from the time of Teflon nose cap exposure until $t = 457$ seconds was that the shunt resistance level of the ionized air was less than 5,000,000 ohms and the oscillator readings were offscale. The rapid length change indicated by the measurements during the period from $t = 457$ to $t = 460$ seconds was because the shunt resistance level of the ionized air, although high enough (above 5,000,000 ohms) to allow onscale oscillator readings, was still low enough to appreciably affect the oscillator readings.

As a check on the results indicated by the circuit shown in figure 23, several tests were made in an arc-heated air jet. The tests were made with the use of a resistance-capacitance (R-C) oscillator such as used in the circuit shown in figure 23 and the present flight test, and also an inductance-capacitance (L-C) oscillator as was used in the flight test of reference 4. Offscale results were obtained with the R-C oscillator but not with the L-C oscillator, indicating that the sensors are capable of giving accurate measurements in ionized air.

Although the sensor measurements were affected by the ionized air until $t = 460$ seconds, the thermocouples were not affected after $t = 447$ seconds. The lesser degree of sensitivity of the thermocouple to ionized air was probably due to the thermocouple wire having a resistance of 10,000 ohms. Thus, a higher degree of air ionization would be required to shunt the thermocouples since the shunt resistance would have to be less than 10,000 ohms as compared to 5,000,000 ohms for the sensors.

RESULTS AND DISCUSSION

General

The time histories of the heating rates q along the inconel nose face, corners, and forebody are shown in figures 24(a), 24(b), and 24(c), respectively. The values of q were derived from the temperatures shown in figure 19, with the use of the one-dimensional heat-flow analysis of reference 5. Briefly, the analysis provides computed points of outside wall temperature at equal time increments. The time increment depends on the thermal capacity of the skin and the heating rate level and was 0.25 second for the present investigation. The computed outside temperature values were used to determine the net heat input values. The values of q shown in figure 24 are the net heat input values corrected for radiation from the inconel surface by assuming a surface emissivity of 0.7. Computations showed that conduction effects along the inconel skin were negligible. Figure 25 is a crossplot of the data presented in figure 24 for $t = 422$, 426, and 430 seconds.

[redacted]

From figure 25 the heating rates along the face, for the different thermocouple locations, are very nearly equal in numerical value. The four corner locations exhibit essentially the same heating-rate values as the face locations. The forebody locations indicate heating levels that, for corresponding times, are appreciably less than those shown by the face and corner locations.

Evaluation of the dynamic motion data indicated that during the heating period the spinning flight payload underwent large variations in angle of attack. Figure 26 shows these variations with flight time. In the appendix of this paper a technique is described, the use of which enables the determination of the effect of angle of attack on heating rates. The technique makes use of heat-transfer results obtained from wind-tunnel tests of scale models of the flight payload. These tests were conducted at Mach numbers of 5.96 and 9.6 and at angles of attack up to 30° (ref. 6). Although the tunnel models were not spinning, use of the integrated average of the circumferential heating distribution was assumed to yield the same results as a high spin rate.

Stagnation Heat Transfer

Unfortunately, the data obtained from the nose faces of the tunnel models were not adequate for the determination of the effect of angle of attack on heating rates at all locations on the flight payload blunt face. However, the tunnel data did provide the variation of the heating at the geometric center of the nose face with angle of attack as shown in figure 27. These results are also discussed in the appendix. This information enabled the converting of the flight geometric center point measurements to geometric center point values for $\alpha = 0^{\circ}$.

The blunt flight nose data were adjusted as follows to correspond to the analytical predictions which pertain to hemispherical nose shapes. The equivalent hemispherical nose radius r_{eff} of the blunt flight nose shape was calculated from the relation

$$r_{eff} = r_n \frac{\beta_{hs}}{\beta_F}$$

where r_n is the normal distance from the center line to the corner of the flight nose configuration. The β_{hs} and β_F terms are the stagnation velocity gradients corresponding to a hemisphere and to the flight nose, respectively. The Newtonian numerical value was used for β_{hs}, whereas the numerical value of β_F was derived from surface pressure measurements obtained from small-scale models tested in the tunnel at $M = 5.96$ and $M = 9.60$ (ref. 6). The numerical value of r_{eff} was determined to be 1.131 feet. The converted results are shown in figure 28 as the variation of the geometric center point heating-rate parameter

[redacted]

$$\frac{\left(q_{gc}\right)_{\alpha=0}\sqrt{r_{eff}}}{1 - \frac{H_w}{H_s}}$$

with the density-velocity parameter

$$\left(\frac{\rho_\infty}{\rho_o}\right)^{1/2}\left(\frac{V_\infty}{10^4}\right)^3$$

The flight data are for a free-stream velocity of about 22,500 fps and an altitude range of approximately 300,000 to 200,000 feet. The solid line represents values computed from the empirical relationship of reference 7. This relationship may be expressed as

$$\frac{q_{as}\sqrt{r_n}}{1 - \frac{H_w}{H_s}} = 17,600\left(\frac{\rho_\infty}{\rho_o}\right)^{1/2}\left(\frac{V_\infty}{25,900}\right)^{3.15}\left[\frac{H_s}{H_s - \left(H_w\right)_{540^\circ\ R}}\right]$$

The values from reference 7 vary nearly linearly with the density-velocity parameter as indicated by the solid-line curve which is a fairing of computed values. With the exception of the last datum point, the converted flight measurements also exhibit a linear trend but of slightly higher slope than the computations of reference 7.

Of interest is the comparison of the present flight test results with a relationship developed from basically theoretical considerations. Such a relationship is that of reference 8, which may be expressed as

$$\frac{q_{as}\sqrt{r_n}}{1 - \frac{H_w}{H_s}} = 0.767 N_{Pr}^{-0.6} H_s\left(\rho_s\mu_s\right)^{0.5}\left(\frac{\rho_w\mu_w}{\rho_s\mu_s}\right)^{0.07}\left(\beta_{hs} r_n\right)^{0.5}$$

The dashed line represents values computed from the relationship of reference 8. In computing these values, the real gas properties were read from a Mollier diagram for equilibrium air (ref. 9), and the transport properties were taken from reference 10. The values from reference 8 also vary linearly with the density-velocity parameter as indicated by the dashed line which is the fairing of the computations. Throughout the data range, the values of reference 8 are 15 to 20 percent lower than the converted flight values.

Forebody Heat Transfer

In addition to providing the variation of the heating with angle of attack at the geometric center point, the tunnel results at $M = 9.6$ also provided sufficient data to evaluate the effects of angle of attack at $s/r_n = 2.1$. The integrated average forebody heating for this location, normalized with respect to the geometric center point, as a function of angle of attack is shown in figure 29. The procedure for obtaining this curve is given in the appendix. Applying the variation shown in figure 29 to the angle-of-attack history shown in figure 26 results in the oscillating dashed-line curve shown in figure 30. The results are shown as the forebody heating rates, normalized with respect to the geometric center point heating rates, as a function of flight time. The solid-line curve is the integrated average of the dashed-line variation; the circular symbols are the flight derived measurements. The integrated average variation agrees closely with the flight measurements, and the oscillatory behavior with angle of attack resulted in a heating level on the afterbody of approximately twice that for zero angle-of-attack flight (ref. 6).

The flight measurements in ratio form are compared with an integrated average of the predicted ones from wind-tunnel tests. This was necessitated by the nature of the calorimeter-thermocouple measuring technique employed in the experiment. The calorimeter, by virtue of its heat capacity, tends to make no discrimination between a high frequency variation in heating rates and a constant heating rate whose magnitude is equal to the average heating rate over one of the high frequency cycles. Added to this is the fact that the flight thermocouple data were faired in order to compute the heating rates.

Ablation

The computed ablated length l as a function of flight time for the geometric stagnation point is shown in figure 31. The values were computed from the relationship

$$l = \frac{12}{\rho} \int_t \left(\frac{q_{gc}}{h_{eff}}\right) dt$$

where ρ is the Teflon specific density and q_{gc} and h_{eff} are the geometric stagnation point heating rate and Teflon effective heat of ablation, respectively.

The values of h_{eff} and q_{gc} used are shown in figure 32(a). The values of h_{eff} were obtained by using the quasi-steady-state analysis of reference 11. The relationship from reference 7 was used to obtain the aerodynamic stagnation point heating rates. Since the flight payload was still undergoing variations in angle of attack, the computed aerodynamic heating rates were corrected to give the variation of the heating at the geometric center of the nose face. The correction ratios $q_{gc}/(q_{gc})_{\alpha=0}$ shown in figure 32(b) were obtained by the procedure described in the appendix. The computed values of l ranged from 0 at $t = 438$ seconds, assumed start of ablation, to $l = 0.1877$ inch at $t = 459$ seconds at which time the computed value of q_{gc} becomes zero and ablation ends.

As was previously mentioned only measurements of total length changes (key of fig. 31) were obtained during flight; thus, a direct comparison with the computed variation of l cannot be made. However, the total length change at the geometric stagnation point may be compared with the value of l at t = 459 seconds. The measured geometric stagnation point value (sensor 3) is 0.185 inch as compared with a computed value of 0.1877 inch.

Blackout

The flight payload telemetry signals were blacked out during a portion of the reentry due to the formation of a plasma in the shock layer. This blackout resulted from absorption and reflection of the electromagnetic energy by the plasma layer. (See ref. 12.) Figure 33 shows the time histories of the received signal strength at the Bermuda tracking station. Figure 34 shows the time histories of the voltage standing-wave ratios (VSWR) for the payload antennas. Real-time data loss resulted from the drop in signal strength during the period from 425 seconds to 450 seconds after launch. During this period the increase in VSWR indicates an associated loss in antenna performance.

SUMMARY OF RESULTS

Measurements of heat transfer were obtained for reentry velocities up to 22,500 fps. The altitudes ranged from 390,000 to 200,000 feet. During this reentry period the penetration angle was -15°. The payload ballistic coefficient was approximately 150 lb/sq ft. The velocities during the ablation test period ranged from 22,000 fps at an altitude of 180,000 feet to 4,200 fps at an altitude of 60,000 feet.

During the heat-transfer period the payload underwent variations in angle-of-attack ranging from 10° to 40°. During the ablation period, the angle of attack varied from 2° to 20°. The angle-of-attack effects were evaluated through use of heat-transfer results obtained from wind-tunnel tests of scale models of the flight payload.

The three-dimensional stagnation point heating rates derived from the flight measurements were slightly higher than values computed from the empirical relationship of reference 7, and about 15 to 20 percent higher than values computed from the analysis of reference 8.

The heating rates measured on the forebody of the spinning payload were in good agreement with predictions based on the results of stationary model wind-tunnel measurements.

The predicted Teflon ablation was computed with the use of the quasi-steady-state effective heats of ablation given in reference 11. The heating rates were computed from the relationship of reference 7 and were adjusted for the angle-of-attack variation. The predicted value of ablated length was 0.1877 inch whereas the measured value was 0.185 inch.

The received signal strength from the telemeter transmitters and the forward and reflected transmission line voltage measurements delineated the reentry blackout boundaries for the present investigation.

Langley Research Center,
National Aeronautics and Space Administration,
Langley Station, Hampton, Va., February 5, 1964.

APPENDIX

STAGNATION POINT AND FOREBODY HEAT-TRANSFER ANALYSIS

The technique described in this appendix was used in the analysis of the stagnation point and afterbody heating. The technique makes use of the results of a series of wind-tunnel tests which were made prior to the actual flight. The wind-tunnel tests were conducted at Mach numbers of 5.96 and 9.6 for two configurations similar to the Scout payload configuration (sketch 1). Data were obtained at angles of attack from 0° to 30° and at angles of rotation from +90° (windward ray) to -90° (leeward ray) for locations on the nose face and along the forebody and have been published in reference 6.

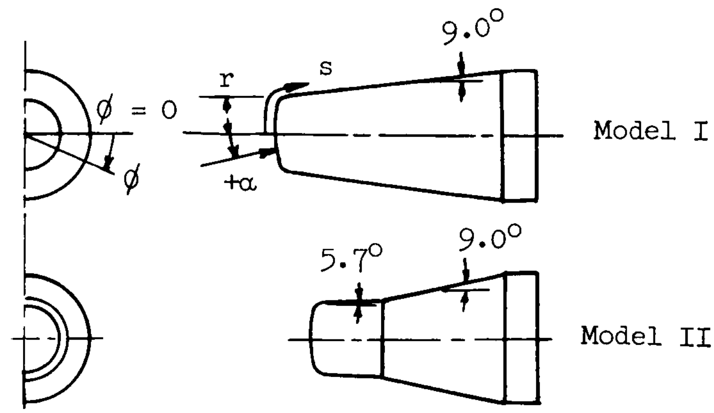

Sketch 1

Stagnation Point

Since test conditions remained constant during all runs, the measured value of the heat-transfer coefficient at the geometric center of the nose at zero angle of attack $\left((h_{gc})_{\alpha=0}\right)$ was taken as a reference value of aerodynamic heat-transfer coefficient. A plot of measured values of the ratio h_{gc} to $(h_{gc})_{\alpha=0}$ as a function of angle of attack extrapolated to 40° is shown in sketch 2. This curve also applies to a spinning body in which the spin axis passes through the geometric center point.

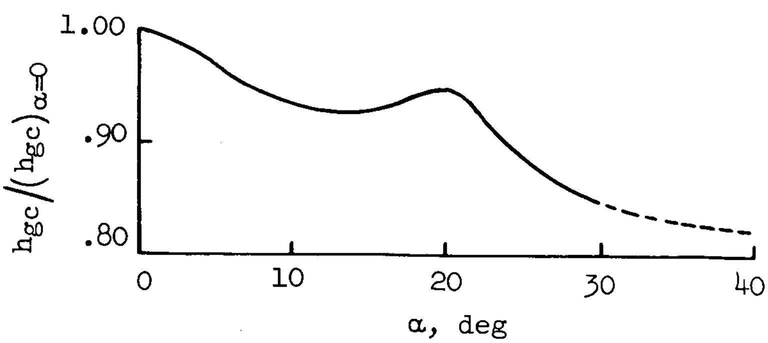

Sketch 2

[redacted]

By applying the angle-of-attack variation of $h_{gc}/(h_{gc})_{\alpha=0}$ shown in sketch 2 to the actual angle-of-attack time history (fig. 26), a time history of $h_{gc}/(h_{gc})_{\alpha=0}$ was obtained as shown in sketch 3. Examination of the thermal

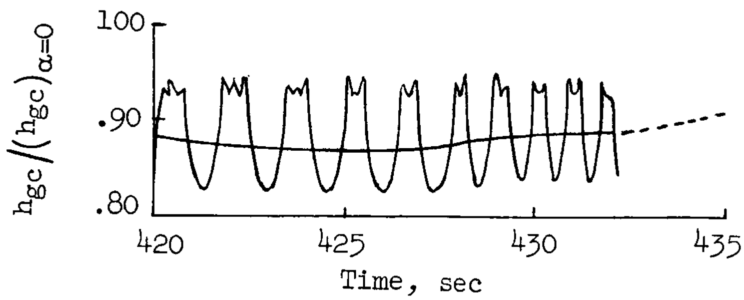

Sketch 3

capacitance and rates of oscillation indicates that the calorimeter cap was not sufficiently sensitive to record these high rate variations. Therefore, to simulate the actual behavior of the measuring devices, the time variation of $h_{gc}/(h_{gc})_{\alpha=0}$ was integrated and averaged over small intervals. The resulting time history of average integrated values of $h_{gc}/(h_{gc})_{\alpha=0}$ is given by the solid line in sketch 3. The dashed line represents an approximate extrapolation since the accelerometer and gyro data in this region are in doubt.

Forebody

In contrast to the wind-tunnel models, the flight model was undergoing spinning motions and severe angle-of-attack changes. In order to analyze the effects of spinning on the heating to the forebody of the model, plots were made of the circumferential heating distribution for each angle of attack at which wind-tunnel data were taken. A typical distribution is shown in sketch 4.

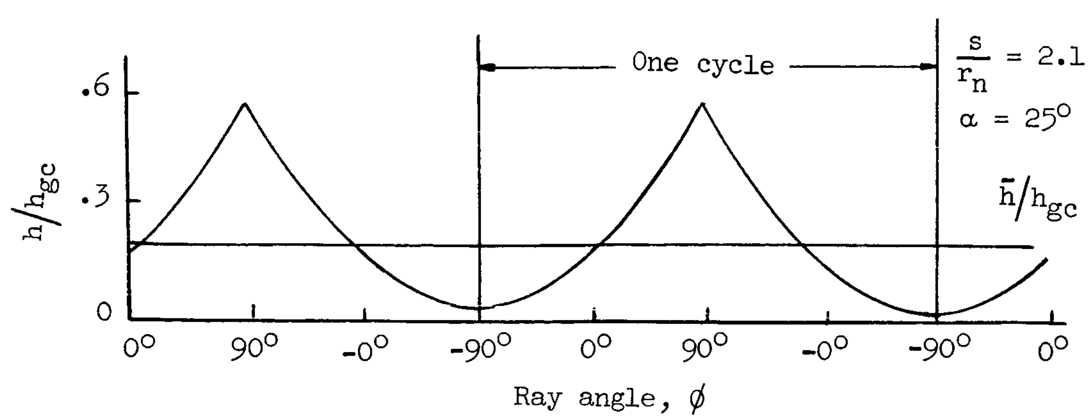

Sketch 4

[redacted]

[redacted]

The ordinate represents the ratio of local heat-transfer coefficient of a point on the periphery to the heat-transfer coefficient at the geometric center of the nose. The abscissa is the angle of rotation ϕ; 90° representing the windward position and -90° the leeward position.

From the characteristics of the heat path, the sampling rates and the spin rate (approximately 2.5 revolutions/sec) of the flight model, the flight data could not be expected to show the variation in heating rates caused by the rotation of the model. Therefore, as a net effect, the skin of the flight model was assumed to act so as to integrate the variation. To simulate this effect, the circumferential heating curves were integrated and an average value found. The average value for $\alpha = 25^\circ$ is shown in sketch 4 as $\bar{h}/h_{gc}$.

As a check on the error caused by this assumption, a temperature-response curve was plotted. For this comparison, the ratio h/h_{gc} was taken to be equal to q/q_{gc}. An arbitrary value of $q_{gc} = 80$ Btu/(sq ft)(sec) was assumed and the time interval for the plot was chosen as 0.4 second, the approximate period of the actual spinning motions. The resulting plot is shown in sketch 5.

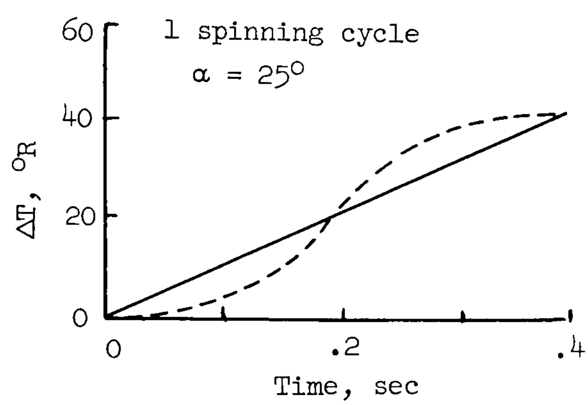

Sketch 5

The dashed line represents the temperature response computed when the values of h/h_{gc} are used and the solid line, when the integrated average value $\bar{h}/h_{gc}$ is used. The maximum discrepancy is on the order of 6° R.

Sketch 6 shows the variation of $\bar{h}/h_{gc}$ with angle of attack; again, the curve has been extraploated from $\alpha = 30^\circ$ to 40°.

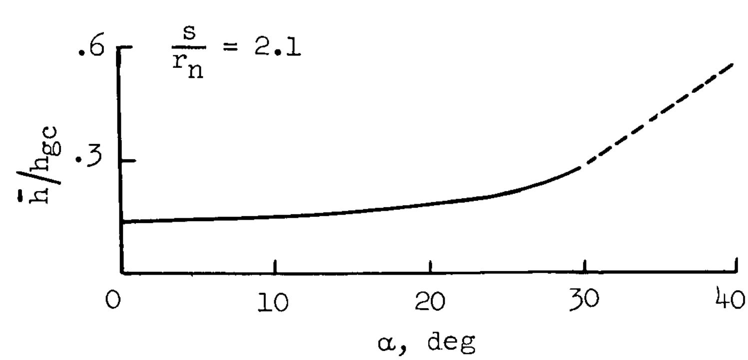

Sketch 6

The relationship between average heat-transfer coefficient and angle of attack was then applied to the angle-of-attack time history (fig. 26). Once again, the assumption was made that h/h_{gc} was equivalent

[redacted]

[redacted]

to q/q_{gc} in order to compare the results predicted by this method with the actual flight measurements. The results are presented in figure 30.

The calorimeter measuring device was not sensitive enough to determine the high rate fluctuation of the heating rates. Therefore, these computed oscillatory heating rates were also integrated and averaged in order to permit comparison with the flight data.

One assumption made in the text requires further justification; namely, the assumption that h/h_{gc} and q/q_{gc} are equivalent at any given station and instant of time.

Since reradiation was only of the order of 1 percent

$$q = h\left(T_{aw} - T_w\right)$$

$$\frac{q}{q_{gc}} = \frac{h}{h_{gc}}\left[\frac{\left(T_{aw} - T_w\right)_f}{\left(T_{aw} - T_w\right)_{gc}}\right]$$

Since for the data range covered, the quantities $\left(T_{aw} - T_w\right)_f$ and $\left(T_{aw} - T_w\right)_{gc}$ were nearly equal in numerical value,

$$\left[\frac{\left(T_{aw} - T_w\right)_f}{\left(T_{aw} - T_w\right)_{gc}}\right] \approx 1$$

therefore,

$$\frac{q}{q_{gc}} \approx \frac{h}{h_{gc}}$$

Finally, although the thermal capacity of the wall and the sampling rates do, to a great extent, tend to average the time variation of the heating rates, some variation is measured. Since the data received are in the form of temperature time histories and since the range of temperature fluctuations was within the inherent scatter of the temperature data, there was no way of actually determining the sizes and shapes of these fluctuations from the data. Therefore, integrating and averaging of the data was introduced when the temperature data were faired.

[redacted]

[redacted]

REFERENCES

1. Anon.: U.S. Standard Atmosphere, 1962. NASA, U.S. Air Force, and U.S. Weather Bureau, Dec. 1962.

2. Engler, Nicholas A.: Development of Methods To Determine Winds, Density, Pressure and Temperature from the Robin Falling Balloon. Contract AF 19(604)-7450, Univ. of Dayton Res. Inst., Oct. 1962.

3. Winters, Clyde W., and Bracalente, Emedio M.: A Sensor for Obtaining Ablation Rates. NASA TN D-800, 1961.

4. Winters, Clyde W., Witte, William G., Rashis, Bernard, and Hopko, Russell N.: A Free-Flight Investigation of Ablation of a Blunt Body to a Mach Number of 13.1. NASA TN D-1500, 1962.

5. Hill, P. R.: A Method of Computing the Transient Temperature of Thick Walls From Arbitrary Variation of Adiabatic-Wall Temperature and Heat-Transfer Coefficient. NACA Rep. 1372, 1958. (Supersedes NACA TN 4105.)

6. Holloway, Paul F., and Dunavant, James C.: Heat-Transfer and Pressure Distributions at Mach Numbers of 6.0 and 9.6 Over Two Reentry Configurations for the Five-Stage Scout Vehicle. NASA TN D-1790, 1963.

7. Detra, R. W., Kemp, N. H., and Riddell, F. R.: Addendum to "Heat Transfer to Satellite Vehicles Re-entering the Atmosphere." Jet Propulsion, vol. 27, no. 12, Dec. 1957, pp. 1256-1257.

8. Cohen, Nathaniel B.: Boundary-Layer Similar Solutions and Correlation Equations for Laminar Heat-Transfer Distribution in Equilibrium Air at Velocities up to 41,000 Feet Per Second. NASA TR R-118, 1961.

9. Feldman, Saul: Hypersonic Gas Dynamic Charts for Equilibrium Air. Res. Rep. 40, Avco-Everett Res. Lab., Jan. 1957.

10. Hansen, C. Frederick: Approximations for the Thermodynamic and Transport Properties of High-Temperature Air. NASA TR R-50, 1959. (Supersedes NACA TN 4150.)

11. Rashis, Bernard, and Hopko, Russell N.: An Analytical Investigation of Ablation. NASA TM X-300, 1960.

12. Huber, Paul W., and Nelson, Clifford H.: Plasma Frequency and Radio Attenuation. Proceedings of the NASA-University Conference on the Science and Technology of Space Exploration, Vol. 2, NASA SP-11, 1962, pp. 347-360. (Also available as NASA SP-25.)

[redacted]

TABLE I.- VELOCITY PACKAGE AND ADAPTOR WEIGHTS

Weights of fifth stage:	
Telemeter package, lb	50.60
Inconel cap, lb	8.48
Teflon nose cap with sensors, lb	14.27
Payload structure, lb	48.50
Motor support, lb	8.81
Ballast, lb	6.49
Motor at burnout, lb	18.30
Total components weight, lb	155.45
Propellant weight, lb	140.80
Loaded weight, lb	296.25
Weights of adaptor connecting fourth and fifth stages:	
Payload adaptor and separation device, lb	55.74
Attachment hardware, lb	0.13
Balance weight, lb	0.50
Total weight atop Scout, lb	352.62

[redacted]

TABLE II.- INCONEL INSIDE SURFACE TEMPERATURE MEASUREMENTS

t, sec	T, °R	t, sec	T, °R	t, sec	T, °R	t, sec	T, °R
Thermocouple 1							
407.756	550	414.106	533	420.428	555	426.366	748
407.956	548	414.306	539	420.626	565	427.356	812
408.148	535	414.498	537	420.826	582	427.548	828
408.346	535	414.696	548	421.026	572	427.746	837
408.546	539	414.896	543	421.218	577	427.946	879
408.746	535	415.096	548	421.416	588	428.146	886
408.946	534	415.296	550	421.616	591	428.536	902
409.336	529	415.686	546	421.816	602	428.736	916
409.536	527	415.886	542	422.016	602	429.128	946
409.736	521	416.086	534	422.208	611	429.326	968
409.936	531	416.286	537	422.406	606	429.726	998
410.336	532	416.478	542	422.606	607	429.926	1010
410.536	528	416.676	537	422.806	618	430.316	1047
410.728	537	416.876	539	423.006	620	430.708	1087
410.926	540	417.076	545	423.198	625	430.906	1094
411.126	539	417.268	543	423.396	625	431.306	1127
411.326	545	417.466	545	423.596	639	431.506	1163
411.526	544	417.666	543	423.788	645	433.086	1275
411.726	548	417.866	550	423.986	648	433.676	1366
411.918	543	418.058	554	424.186	666	433.876	1376
412.116	539	418.256	558	424.386	670	434.266	1398
412.316	534	418.456	554	424.586	675	434.466	1424
412.516	535	418.848	559	424.778	693	434.856	1502
412.716	532	419.046	556	424.976	689	435.646	1603
412.916	531	419.246	555	425.176	710		
413.116	532	419.446	553	425.376	710		
413.308	534	419.638	553	425.576	726		
413.506	532	419.836	550	425.768	734		
413.706	526	420.036	553	425.966	733		
413.906	532	420.236	560	426.166	738		
Thermocouple 10							
408.652	537	414.902	540	420.932	623	425.967	956
408.852	516	415.002	552	421.027	636	426.067	977
408.952	511	415.102	520	421.127	641	426.267	1003
409.147	521	415.202	545	421.227	636	426.567	963
409.247	521	415.302	542	421.327	650	427.257	1090
409.347	536	415.497	540	421.427	661	427.357	1116
409.447	526	415.597	536	421.527	658	427.457	1126
409.642	534	415.697	536	421.622	653	427.557	1162
409.742	520	415.792	544	421.722	672	427.752	1167
409.842	529	415.992	547	421.822	679	427.852	1179
410.242	520	416.092	524	421.917	702	427.952	1180
410.442	520	416.287	551	422.017	680	428.052	1191
410.742	536	416.387	559	422.117	698	428.347	1250
410.932	522	416.487	533	422.317	690	428.447	1225
411.079	541	416.591	559	422.412	689	428.547	1291
411.232	533	416.882	547	422.512	724	428.642	1300
411.432	528	417.077	545	422.612	718	428.937	1343
411.532	524	417.177	543	422.712	721	429.037	1367
411.632	518	417.377	558	422.812	720	429.137	1387
411.732	529	417.472	559	422.912	734	429.237	1402
411.827	530	417.572	558	423.012	741	429.432	1430
411.927	527	417.672	570	423.112	747	429.532	1441
412.122	524	417.772	566	423.202	765	429.632	1448
412.222	526	417.867	570	423.302	758	429.727	1465
412.422	545	417.967	558	423.402	769	429.827	1493
412.522	528	418.067	561	423.502	783	430.027	1521
412.622	530	418.162	558	423.602	779	430.131	1554
412.722	521	418.362	573	423.702	777	430.222	1576
413.017	531	418.462	578	423.797	782	430.322	1593
413.117	528	418.562	558	423.897	780	430.422	1649
413.217	539	418.757	582	423.997	802	430.617	1654
413.317	522	418.857	587	424.097	801	430.717	1688
413.417	528	419.052	578	424.192	5414	430.817	1713
413.512	525	419.252	585	424.297	814	430.917	1725
413.612	541	419.352	587	424.492	832	431.017	1739
413.712	528	419.452	572	424.592	825	431.159	1782
413.812	546	419.647	600	424.687	838	431.212	1782
413.912	525	419.747	604	424.882	861	431.307	1816
414.012	537	419.842	586	424.982	878	431.407	1840
414.112	533	419.942	611	425.082	889	431.507	1830
414.212	549	420.042	611	425.182	885	433.577	2416
414.307	538	420.142	600	425.282	907	433.677	2452
414.507	531	420.237	618	425.477	914	434.077	2579
414.607	536	420.437	617	425.577	918	434.177	2583
414.707	531	420.632	627	425.677	921	434.272	2603
414.807	536	420.732	636	425.777	931	434.372	2654

[redacted]

TABLE II.- INCONEL INSIDE SURFACE TEMPERATURE MEASUREMENTS - Continued

t, sec	T, °R	t, sec	T, °R	t, sec	T, °R	t, sec	T, °R	t, sec	T, °R
Thermocouple 2									
408.876	516	414.136	521	418.784	561	423.136	635	428.374	971
408.976	508	414.236	520	418.884	555	423.226	654	428.474	954
409.174	521	414.334	520	419.076	550	423.326	650	428.574	948
409.274	520	414.534	533	419.276	553	423.426	656	428.666	968
409.374	514	414.634	527	419.376	548	423.526	656	428.964	1009
409.474	526	414.734	524	419.476	548	423.626	665	429.064	1020
409.666	529	414.834	527	419.674	559	423.726	659	429.164	1010
409.766	505	414.926	543	419.774	547	423.824	658	429.264	1022
409.866	527	415.026	536	419.866	551	423.924	656	429.456	1059
410.266	513	415.126	522	419.966	578	424.024	666	429.556	1040
410.466	533	415.226	534	420.066	577	424.124	669	429.656	1045
410.766	531	415.326	532	420.166	555	424.216	281	429.754	1091
410.956	513	415.524	533	420.264	580	424.324	692	429.854	1082
411.130	536	415.624	540	420.464	567	424.516	684	430.054	1105
411.256	534	415.724	530	420.656	575	424.616	694	430.160.	1105
411.456	530	415.816	532	420.756	598	424.714	686	430.246	1138
411.556	514	416.016	545	420.956	559	424.906	702	430.346	1135
411.656	522	416.116	519	421.054	574	425.006	715	430.446	1154
411.756	523	416.314	545	421.154	570	425.106	729	430.644	1151
411.854	533	416.414	550	421.254	583	425.206	721	430.744	1144
411.954	520	416.514	535	421.354	586	425.306	732	430.844	1185
412.146	523	416.620	532	421.454	587	425.504	739	430.944	1189
412.246	521	416.906	525	421.554	583	425.604	765	431.044	1175
412.446	527	417.104	526	421.646	583	425.704	769	431.210	1206
412.546	524	417.204	529	421.746	594	425.804	749	431.236	1203
412.646	522	417.404	548	421.846	520	425.994	772	431.334	557
412.746	518	417.496	544	421.944	599	426.094	783	431.434	1249
413.044	529	417.596	545	422.044	607	426.294	791	431.534	1241
413.144	523	417.696	545	422.144	613	426.594	762	433.604	1489
413.244	529	417.796	561	422.344	594	427.284	859	433.704	1470
413.344	516	417.894	551	422.436	601	427.384	1057	434.104	1511
413.444	526	417.994	537	422.536	624	427.484	891	434.204	1510
413.536	521	418.094	536	422.636	632	427.584	917	434.296	1439
413.636	529	418.186	543	422.736	628	427.776	912	434.396	1464
413.736	517	418.386	543	422.836	633	427.876	943	434.494	1478
413.836	540	418.486	545	422.936	627	427.976	935	434.794	1578
413.936	527	418.586	541	423.036	646	428.076	941	434.894	1613
414.036	525								
Thermocouple 4									
408.670	538	413.930	527	418.480	560	422.930	705	427.970	1182
408.870	512	414.030	530	418.580	552	423.030	715	428.070	1183
408.970	512	414.130	518	418.777	566	423.130	722	428.367	1224
409.167	521	414.230	532	418.877	562	423.220	733	428.467	1199
409.267	514	414.327	524	419.070	565	423.320	721	428.567	1246
409.367	525	414.527	532	419.270	567	423.420	721	428.660	1267
409.467	526	414.627	534	419.370	571	423.520	737	428.957	1326
409.660	529	414.727	525	419.470	564	423.620	743	429.057	1336
409.760	511	414.827	532	419.667	575	423.720	753	429.157	1354
409.860	525	414.920	539	419.767	563	423.817	753	429.257	1351
410.260	511	415.020	549	419.860	569	423.917	750	429.450	1405
410.460	528	415.120	520	419.960	595	424.017	757	429.550	1393
410.760	536	415.220	540	420.060	595	424.117	774	429.650	1409
410.950	516	415.320	541	420.160	578	424.210	3427	429.747	1437
411.117	536	415.517	535	420.257	593	424.317	798	429.847	1461
411.250	533	415.617	542	420.457	593	424.510	846	430.047	1471
411.450	530	415.717	531	420.650	610	424.610	798	430.153	1505
411.550	527	415.810	533	420.750	628	424.707	812	430.240	1553
411.650	523	416.010	545	420.950	603	424.900	821	430.340	1566
411.750	521	416.110	522	421.047	601	425.000	830	430.440	1588
411.847	526	416.307	541	421.147	612	425.100	856	430.637	1612
411.947	520	416.407	550	421.247	611	425.200	852	430.737	1629
412.140	517	416.507	545	421.347	630	425.300	864	430.837	1635
412.240	525	416.613	541	421.447	628	425.497	876	430.937	1642
412.440	535	416.900	549	421.547	644	425.597	900	431.037	1669
412.540	524	417.097	537	421.640	619	425.697	902	431.197	1724
412.640	525	417.197	530	421.740	655	425.797	905	431.230	1717
412.740	518	417.397	551	421.840	609	425.987	920	431.327	1240
413.037	529	417.490	558	421.937	657	426.087	939	431.427	1744
413.137	520	417.590	548	422.037	645	426.287	962	431.527	1766
413.237	532	417.690	559	422.137	665	426.587	929	433.597	2277
413.337	530	417.790	554	422.337	650	427.277	1057	433.697	2332
413.437	527	417.887	564	422.430	657	427.377	1073	434.097	2393
413.530	520	417.987	549	422.530	682	427.477	1101	434.197	2412
413.630	537	418.087	554	422.630	683	427.577	1120	434.290	2386
413.730	517	418.180	542	422.730	701	427.770	1120	434.390	2499
413.830	540	418.380	549	422.830	705	427.870	1152	434.487	2528

[redacted]

TABLE II.- INCONEL INSIDE SURFACE TEMPERATURE MEASUREMENTS - Continued

t, sec	T, °R	t, sec	T, °R	t, sec	T, °R	t, sec	T, °R	t, sec	T, °R	t, sec	T, °R
Thermocouple 3						Thermocouple 5					
407.543	548	415.283	553	422.793	635	407.530	548	414.670	548	421.590	679
407.743	546	415.673	545	422.993	635	407.730	545	414.870	548	421.790	695
407.943	548	415.873	539	423.185	643	407.930	544	415.070	551	421.990	704
408.135	537	416.073	539	423.383	649	408.122	540	415.270	552	422.182	720
408.333	535	416.273	535	423.583	657	408.320	535	415.660	551	422.380	718
408.533	540	416.465	541	423.775	673	408.520	541	415.860	543	422.580	718
408.733	538	416.663	536	423.973	667	408.720	538	416.060	542	422.780	737
408.933	532	416.863	541	424.173	698	408.920	531	416.260	542	422.980	742
409.323	528	417.063	543	424.373	710	409.310	530	416.452	547	423.172	770
409.523	526	417.255	548	424.573	715	409.510	528	416.650	545	423.370	777
409.723	521	417.453	543	424.765	729	409.710	521	416.850	550	423.570	788
409.923	532	417.653	546	424.963	724	409.910	534	417.050	552	423.762	810
410.323	529	417.853	556	425.163	749	410.310	529	417.242	551	423.960	814
410.523	526	418.045	556	425.363	754	410.510	526	417.440	553	424.160	838
410.715	537	418.243	558	425.563	777	410.702	537	417.640	552	424.360	853
410.913	540	418.443	555	425.755	793	410.900	540	417.840	565	424.560	876
411.113	544	418.835	560	425.953	796	411.100	545	418.032	568	424.752	899
411.313	548	419.033	562	426.153	802	411.300	548	418.230	566	424.950	897
411.513	543	419.233	556	426.353	805	411.500	542	418.430	570	425.150	932
411.713	548	419.433	557	427.343	893	411.700	554	418.822	583	425.350	943
411.905	540	419.625	551	427.535	909	411.892	542	419.020	589	425.550	958
412.103	539	419.823	554	427.733	916	412.090	539	419.220	584	425.742	986
412.303	532	420.023	555	427.933	969	412.290	532	419.420	587	425.940	1003
412.503	532	420.223	560	428.133	981	412.490	532	419.612	590	426.140	1024
412.703	529	420.415	556	428.523	1006	412.690	535	419.810	595	426.340	1038
412.903	531	420.613	568	428.723	1020	412.890	534	420.010	601	427.330	1178
413.103	530	420.813	579	429.115	1064	413.090	532	420.210	612	427.522	1217
413.295	533	421.013	574	429.313	1101	413.282	536	420.402	612	427.720	1240
413.493	535	421.205	587	429.713	1128	413.480	539	420.600	623	427.920	1291
413.693	526	421.403	589	429.913	1146	413.680	527	420.800	636	428.120	1329
413.893	532	421.603	596	430.303	1189	413.880	536	421.000	637	428.510	1390
414.093	533	421.803	605	430.695	1234	414.080	536	421.192	654	428.710	1414
414.293	537	422.003	603	430.893	1237	414.280	542	421.390	663	429.102	1497
414.485	537	422.195	623	431.293	1278	414.472	540				
414.683	545	422.393	617	431.493	1316						
414.883	548	422.593	617	433.073	1446						
415.083	545										

t, sec	T, °R	t, sec	T, °R	t, sec	T, °R	t, sec	T, °R	t, sec	T, °R	t, sec	T, °R
Thermocouple 7						Thermocouple 9					
407.516	545	415.056	550	422.566	695	407.503	545	415.243	548	422.753	692
407.716	545	415.256	548	422.766	706	407.703	542	415.633	548	422.953	703
407.916	544	415.646	548	422.966	723	407.903	544	415.833	543	423.147	725
408.110	537	415.846	542	423.160	741	408.097	535	416.033	540	423.343	735
408.306	535	416.046	542	423.356	751	408.293	534	416.233	542	423.543	740
408.506	540	416.246	542	423.556	757	408.493	536	416.427	550	423.737	755
408.706	535	416.440	550	423.750	776	408.693	534	416.623	545	423.933	769
408.906	536	416.636	547	423.946	782	408.893	537	416.823	548	424.133	777
409.296	529	416.836	550	424.146	796	409.283	529	417.023	548	424.333	786
409.496	529	417.036	555	424.346	809	409.483	529	417.217	549	424.533	810
409.696	522	417.230	545	424.546	825	409.683	522	417.413	550	424.727	829
409.896	535	417.426	550	424.740	847	409.883	532	417.613	547	424.923	831
410.296	530	417.626	552	424.936	858	410.283	529	417.813	560	425.123	856
410.496	528	417.826	560	425.136	879	410.483	528	418.007	563	425.323	872
410.690	537	418.020	565	425.336	899	410.677	536	418.203	569	425.523	876
410.886	540	418.216	572	425.536	903	410.873	534	418.403	566	425.717	893
411.086	544	418.416	566	425.730	927	411.073	545	418.797	574	425.913	910
411.286	548	418.810	579	425.926	944	411.273	543	418.993	576	426.113	926
411.486	543	419.006	581	426.126	961	411.473	543	419.193	575	426.313	947
411.686	549	419.206	577	426.326	982	411.673	547	419.393	573	427.303	1046
411.880	542	419.406	577	427.316	1090	411.867	539	419.587	575	427.497	1078
412.076	542	419.600	580	427.510	1124	412.063	542	419.783	586	427.693	1107
412.276	532	419.796	590	427.706	1151	412.263	534	419.983	587	427.893	1135
412.476	532	419.996	591	427.906	1182	412.463	532	420.183	601	428.093	1158
412.676	534	420.196	604	428.106	1215	412.663	531	420.377	601	428.483	1215
412.876	535	420.390	608	428.496	1274	412.863	532	420.573	609	428.683	1246
413.076	533	420.586	615	428.696	1304	413.063	532	420.773	618	429.077	1314
413.270	536	420.786	623	429.090	1370	413.257	533	420.973	623	429.273	1343
413.466	539	420.986	631	429.286	1404	413.453	539	421.167	628	429.673	1405
413.666	530	421.180	637	429.686	1466	413.653	530	421.363	640	429.873	1446
413.866	540	421.376	651	429.886	1507	413.853	536	421.563	650	430.263	1509
414.066	537	421.576	657	430.276	1587	414.053	534	421.763	663	430.657	1587
414.266	540	421.776	673	430.670	1680	414.253	541	421.963	675	430.853	1624
414.460	540	421.976	686	430.866	1714	414.447	537	422.157	686	431.253	1708
414.656	549	422.170	698	430.266	1801	414.643	549	422.353	677	431.453	1748
414.856	545	422.366	697	431.466	1853	414.843	542	422.553	685	433.033	2129
						415.043	549				

[redacted]

[redacted]

TABLE II.- INCONEL INSIDE SURFACE TEMPERATURE MEASUREMENTS - Continued

t, sec	T, °R	t, sec	T, °R	t, sec	T, °R	t, sec	T, °R	t, sec	T, °R
Thermocouple 6									
408.664	538	413.824	544	418.080	554	422.424	691	426.580	1012
408.864	516	413.924	525	418.174	558	422.524	724	427.270	1140
408.964	512	414.024	529	418.374	567	422.624	728	427.370	1171
409.160	521	414.124	528	418.474	572	422.724	732	427.470	1181
409.260	523	414.224	531	418.574	558	422.824	746	427.570	1218
409.360	523	414.320	528	418.770	582	422.924	741	427.764	1231
409.460	530	414.520	533	418.870	577	423.024	759	427.864	1241
409.654	528	414.620	534	419.064	574	423.124	754	427.964	1271
409.754	516	414.720	531	419.264	571	423.214	779	428.064	1282
409.854	533	414.820	533	419.364	583	423.314	770	428.360	1331
410.254	515	414.914	542	419.464	571	423.414	785	428.460	1304
410.454	521	415.014	548	419.660	585	423.514	786	428.560	1369
410.754	536	415.114	532	419.760	599	423.614	794	428.654	1383
410.944	519	415.214	540	419.854	582	423.714	785	428.950	1428
411.104	541	415.314	542	419.954	621	423.810	808	429.050	1458
411.244	533	415.510	547	420.054	609	423.910	798	429.150	1465
411.444	532	415.610	536	420.154	608	424.010	822	429.250	1479
411.544	528	415.710	536	420.250	609	424.110	816	429.444	1528
411.644	527	415.804	533	420.450	625	424.204	5187	429.544	1545
411.744	521	416.004	544	420.644	611	424.310	833	429.644	1551
411.840	526	416.104	522	420.744	635	424.504	847	429.740	1585
411.940	526	416.300	551	420.944	623	424.604	852	429.840	1599
412.134	521	416.400	551	421.040	639	424.700	863	430.040	1633
412.234	524	416.500	544	421.140	641	424.894	881	430.146	1660
412.434	536	416.606	550	421.240	639	424.994	905	430.234	1702
412.534	525	416.894	548	421.340	651	425.094	907	430.334	1724
412.634	527	417.090	542	421.440	666	425.194	922	430.434	1769
412.734	520	417.190	543	421.540	659	425.294	928	430.630	1803
413.030	524	417.390	559	421.634	659	425.490	933	430.730	1826
413.130	528	417.484	559	421.734	677	425.590	953	430.830	1838
413.230	528	417.584	558	421.834	644	425.690	963	430.930	1854
413.330	524	417.684	565	421.930	701	425.790	969	431.030	1874
413.430	528	417.784	563	422.030	686	425.980	996	431.184	1944
413.524	524	417.880	570	422.130	702	426.080	1003	431.224	1935
413.624	536	417.980	558	422.330	691	426.280	1037	431.320	1734
413.724	527								
Thermocouple 8									
408.658	538	413.818	544	418.168	558	422.618	702	427.364	1074
408.858	516	413.918	525	418.368	567	422.718	705	427.464	1106
408.958	512	414.018	533	418.468	577	422.818	724	427.564	1131
409.154	521	414.118	528	418.568	553	422.918	713	427.758	1153
409.254	523	414.218	531	418.764	582	423.018	727	427.858	1164
409.354	523	414.314	536	418.864	576	423.118	737	427.958	1173
409.454	531	414.514	527	419.058	574	423.208	748	428.058	1191
409.648	534	414.614	534	419.258	579	423.308	744	428.354	1225
409.748	519	414.714	531	419.358	583	423.408	749	428.454	1212
409.848	535	414.814	536	419.458	581	423.508	754	428.554	1263
410.248	519	414.908	546	419.654	586	423.608	768	428.648	1277
410.448	523	415.008	550	419.754	599	423.708	758	428.944	1322
410.748	536	415.108	531	419.848	582	423.804	767	429.044	1348
410.938	512	415.208	541	419.948	601	423.904	768	429.144	1358
411.092	541	415.308	542	420.048	602	424.004	780	429.244	1362
411.238	533	415.504	540	420.148	592	424.104	783	429.438	1407
411.438	536	415.604	530	420.244	609	424.198	6197	429.538	1421
411.538	528	415.704	536	420.444	618	424.304	794	429.638	1424
411.638	530	415.798	536	420.638	611	424.498	817	429.734	1444
411.738	528	415.998	541	420.738	631	424.598	814	429.834	1466
411.834	530	416.098	525	420.938	623	424.694	821	430.034	1504
411.934	524	416.294	551	421.034	626	424.888	842	430.138	1524
412.128	517	416.394	560	421.134	618	424.988	858	430.228	1546
412.228	528	416.494	550	421.234	632	425.088	872	430.328	1560
412.428	541	416.598	551	421.334	635	425.188	865	430.428	1612
412.528	529	416.888	542	421.434	654	425.288	892	430.624	1643
412.628	527	417.084	529	421.534	649	425.484	893	430.724	1656
412.728	517	417.184	543	421.628	653	425.584	893	430.824	1681
413.024	531	417.384	559	421.728	666	425.684	919	430.924	1692
413.124	528	417.478	554	421.828	681	425.784	913	431.024	1702
413.224	539	417.578	559	421.924	677	425.974	932	431.172	1758
413.324	525	417.678	563	422.024	668	426.074	957	431.218	1757
413.424	528	417.778	566	422.124	682	426.274	983	431.314	1785
413.518	525	417.874	570	422.324	677	426.574	944	431.414	1799
413.618	530	417.974	558	422.418	678	427.264	1078	431.514	1796
413.718	524	418.074	548	422.518	708				

[redacted]

TABLE II.- INCONEL INSIDE SURFACE TEMPERATURE MEASUREMENTS - Continued

t, sec	T, °R	t, sec	T, °R	t, sec	T, °R	t, sec	T, °R	t, sec	T, °R	t, sec	T, °R
Thermocouple 13						Thermocouple 15					
407.476	540	414.816	542	422.132	699	407.463	540	415.593	545	423.303	689
407.676	540	415.016	549	422.326	697	407.663	536	415.793	539	423.503	696
407.876	540	415.216	545	422.526	707	407.863	536	415.993	534	423.699	705
408.072	534	415.606	548	422.726	716	408.059	531	416.193	539	423.893	724
408.266	534	415.806	534	422.926	730	408.253	534	416.389	541	424.093	737
408.466	534	416.006	537	423.122	747	408.453	530	416.583	541	424.293	743
408.666	533	416.206	540	423.316	762	408.653	532	416.783	540	424.493	759
408.866	534	416.402	548	423.516	768	408.853	534	416.983	546	424.689	775
409.256	529	416.596	548	423.712	778	409.243	531	417.179	546	424.883	778
409.456	527	416.796	548	423.906	797	409.443	527	417.373	544	425.083	791
409.656	518	416.996	549	424.106	809	409.643	518	417.573	546	425.283	810
409.856	532	417.192	549	424.306	817	409.843	532	417.773	551	425.483	835
410.256	529	417.386	550	424.506	838	410.243	530	417.969	552	425.679	844
410.456	526	417.586	550	424.702	863	410.443	524	418.163	558	425.873	864
410.652	536	417.786	558	424.896	867	410.639	533	418.363	553	426.073	876
410.846	534	417.982	559	425.096	891	410.833	534	418.759	558	426.273	891
411.046	539	418.176	562	425.296	910	411.033	543	418.953	560	427.263	986
411.246	542	418.376	564	425.496	919	411.233	540	419.153	555	427.459	1005
411.446	540	418.772	574	425.692	931	411.433	536	419.353	557	427.653	1041
411.646	547	418.966	579	425.886	946	411.633	543	419.549	559	427.853	1067
411.842	535	419.166	582	426.086	973	411.829	535	419.743	565	428.053	1070
412.036	539	419.366	576	426.286	1001	412.023	537	419.943	560	428.443	1145
412.236	531	419.562	581	427.276	1107	412.223	531	420.143	571	428.643	1174
412.436	534	419.756	586	427.472	1137	412.423	534	420.339	572	429.039	1225
412.636	531	419.956	593	427.666	1181	412.623	529	420.533	584	429.233	1282
412.836	532	420.156	602	427.866	1205	412.823	532	420.733	584	429.633	1309
413.036	532	420.352	605	428.066	1228	413.023	532	420.933	591	429.833	1325
413.232	533	420.546	626	428.456	1302	413.219	533	421.129	604	430.223	1422
413.426	542	420.746	623	428.656	1335	413.413	534	421.323	605	430.619	1463
413.626	527	420.946	631	429.052	1383	413.613	526	421.523	615	430.813	1511
413.826	536	421.142	642	429.246	1449	413.813	540	421.723	625	431.213	1579
414.026	537	421.336	647	429.646	1513	414.013	532	421.923	631	431.413	1604
414.226	540	421.536	661	429.846	1546	414.213	537	422.119	643	432.993	1917
414.422	537	421.736	677	430.236	1637	414.409	534	422.313	635	433.583	2013
414.616	543	421.936	688			414.603	540	422.513	651	433.783	2052
						414.803	534	422.713	658	434.173	2181
						415.003	548	422.913	665	434.373	2251
						415.203	543	423.109	684		
Thermocouple 17						Thermocouple 19					
407.450	540	415.780	534	423.686	635	407.437	539	415.967	530	423.674	618
407.650	534	415.980	530	423.880	656	407.637	534	416.167	534	423.867	630
407.850	535	416.180	534	424.080	660	407.837	535	416.364	537	424.067	636
408.046	529	416.376	543	424.280	663	408.034	529	416.557	543	424.267	645
408.240	534	416.570	543	424.480	676	408.227	534	416.757	535	424.467	648
408.440	529	416.770	540	424.676	685	408.427	529	416.957	540	424.664	659
408.640	534	416.970	540	424.870	685	408.627	531	417.154	537	424.857	657
408.840	534	417.166	542	425.070	692	408.827	534	417.347	535	425.057	665
409.230	532	417.360	541	425.270	709	409.217	529	417.547	539	425.257	677
409.430	529	417.560	542	425.470	720	409.417	527	417.747	543	425.457	687
409.630	521	417.760	548	425.666	728	409.617	521	417.944	543	425.654	691
409.830	532	417.956	548	425.860	745	409.817	533	418.137	548	425.847	709
410.230	531	418.150	556	426.060	749	410.217	529	418.337	545	426.047	711
410.430	524	418.350	545	426.260	762	410.417	523	418.734	545	426.247	717
410.626	533	418.746	550	427.250	812	410.614	526	418.927	552	427.237	764
410.820	534	418.940	556	427.446	824	410.807	534	419.127	549	427.434	778
411.020	537	419.140	553	427.640	839	411.007	535	419.327	546	427.627	783
411.220	537	419.340	548	427.840	856	411.207	535	419.524	545	427.827	807
411.420	536	419.536	550	428.040	864	411.407	536	419.717	555	428.027	811
411.620	540	419.730	555	428.430	904	411.607	539	419.917	548	428.417	846
411.816	532	419.930	548	428.630	919	411.804	531	420.117	553	428.617	854
412.010	537	420.130	550	429.026	952	411.997	532	420.314	552	429.014	884
412.210	531	420.326	552	429.220	986	412.197	527	420.507	559	429.207	915
412.410	532	420.520	566	429.620	999	412.397	529	420.707	568	429.607	929
412.610	527	420.720	563	429.820	1004	412.597	527	420.907	566	429.807	926
412.810	532	420.920	568	430.210	1067	412.797	532	421.104	574	430.197	991
413.010	529	421.116	578	430.606	1084	412.997	532	421.104	574	430.594	998
413.206	536	421.310	576	430.800	1118	413.194	536	421.297	571	430.787	1027
413.400	539	421.510	580	431.200	1153	413.387	535	421.497	572	431.187	1063
413.600	526	421.710	589	431.400	1159	413.587	527	421.697	587	431.387	1070
413.800	532	421.910	598	432.980	1332	413.787	532	421.897	583	432.967	1222
414.000	532	422.106	599	433.570	1361	413.987	532	422.094	593	433.557	1251
414.200	534	422.300	591	433.770	1377	414.187	531	422.287	585	433.757	1275
414.396	534	422.500	602	434.160	1437	414.384	529	422.487	596	434.147	1326
414.590	540	422.700	609	434.360	1462	414.577	537	422.687	596	434.347	1356
414.790	534	422.900	621	434.750	1491	414.777	535	422.887	607	434.737	1385
414.990	542	423.096	627	435.540	1613	414.977	542	423.084	611	435.527	1463
415.190	537	423.290	629	435.930	1762	415.177	539	423.277	613	435.917	1546
415.580	539	423.490	634			415.567	539	423.477	616	436.707	1700
						415.767	531				

[redacted]

TABLE II.- INCONEL INSIDE SURFACE TEMPERATURE MEASUREMENTS - Concluded

t, sec	T, °R	t, sec	T, °R	t, sec	T, °R	t, sec	T, °R
Thermocouple 14							
408.640	537	414.794	535	420.620	632	425.464	950
408.840	514	414.890	540	420.720	631	425.564	956
408.940	511	414.990	552	420.920	628	425.664	968
409.134	520	415.090	529	421.014	638	425.764	954
409.234	521	415.190	540	421.114	637	425.954	988
409.334	529	415.290	542	421.214	653	426.054	1007
409.434	528	415.484	539	421.314	648	426.254	1033
409.630	540	415.584	536	421.414	659	426.554	990
409.730	520	415.684	536	421.514	658	427.244	1137
409.830	528	415.780	537	421.610	661	427.344	1194
410.230	522	415.980	545	421.710	677	427.444	1181
410.430	525	416.080	524	421.810	680	427.544	1198
410.730	535	416.274	547	421.904	691	427.740	1235
410.920	517	416.374	552	422.004	694	427.840	1255
411.054	541	416.474	533	422.104	702	427.940	1247
411.220	531	416.577	558	422.304	691	428.040	1247
411.420	532	416.870	548	422.400	690	428.334	1333
411.520	525	417.064	544	422.500	725	428.434	1311
411.620	530	417.164	543	422.600	733	428.534	1361
411.720	529	417.364	560	422.700	723	428.630	1385
411.814	530	417.460	552	422.800	728	428.924	1394
411.914	527	417.560	558	422.900	734	429.024	1441
412.110	522	417.660	567	423.000	771	429.124	1497
412.210	531	417.760	559	423.100	759	429.224	1498
412.410	545	417.854	567	423.190	770	429.420	1526
412.510	524	417.954	565	423.290	768	429.520	1538
412.610	522	418.054	549	423.390	785	429.620	1546
412.710	521	418.150	558	423.490	792	429.714	1561
413.004	531	418.350	574	423.590	787	429.814	1574
413.104	526	418.450	577	423.690	776	430.014	1644
413.204	537	418.550	555	423.784	784	430.117	1705
413.304	517	418.744	582	423.884	799	430.210	1701
413.404	528	418.844	572	423.984	819	430.310	1701
413.500	525	419.040	575	424.084	823	430.410	1758
413.600	539	419.240	580	424.180	5578	430.604	1764
413.700	528	419.340	587	424.284	825	430.704	1770
413.800	546	419.440	574	424.480	854	430.804	1810
413.900	530	419.634	601	424.580	857	430.904	1855
414.000	543	419.734	593	424.674	875	431.004	1857
414.100	533	419.830	587	424.870	884	431.134	1897
414.200	533	419.930	615	424.970	899	431.200	1892
414.294	524	420.030	605	425.070	908	431.294	1940
414.494	533	420.130	592	425.170	901	431.394	1945
414.594	532	420.224	619	425.270	925	431.494	1946
414.694	531	420.424	617				

[redacted]

[redacted]

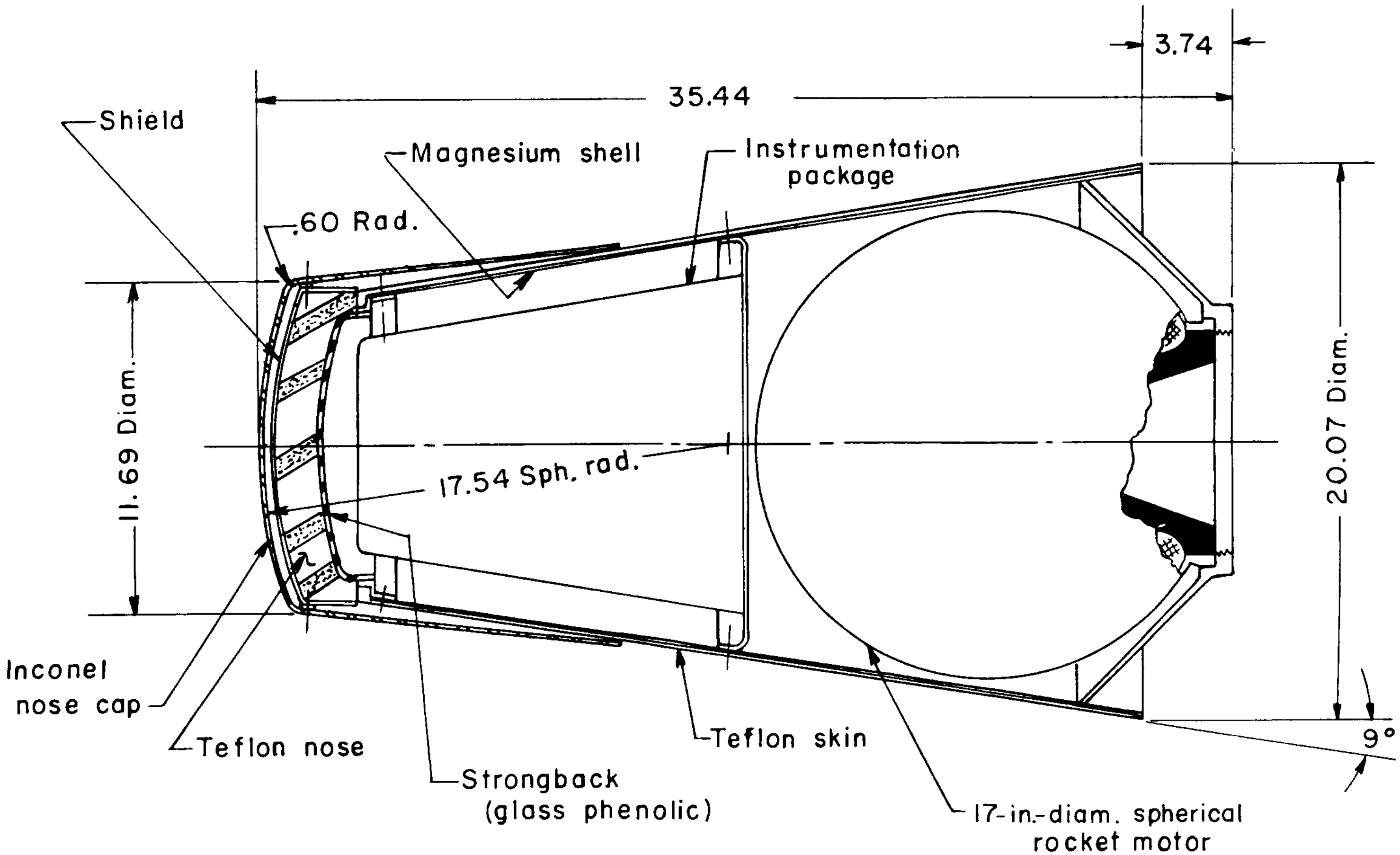

(a) Configuration. All dimensions are in inches.

Figure 1.- Velocity package.

[redacted]

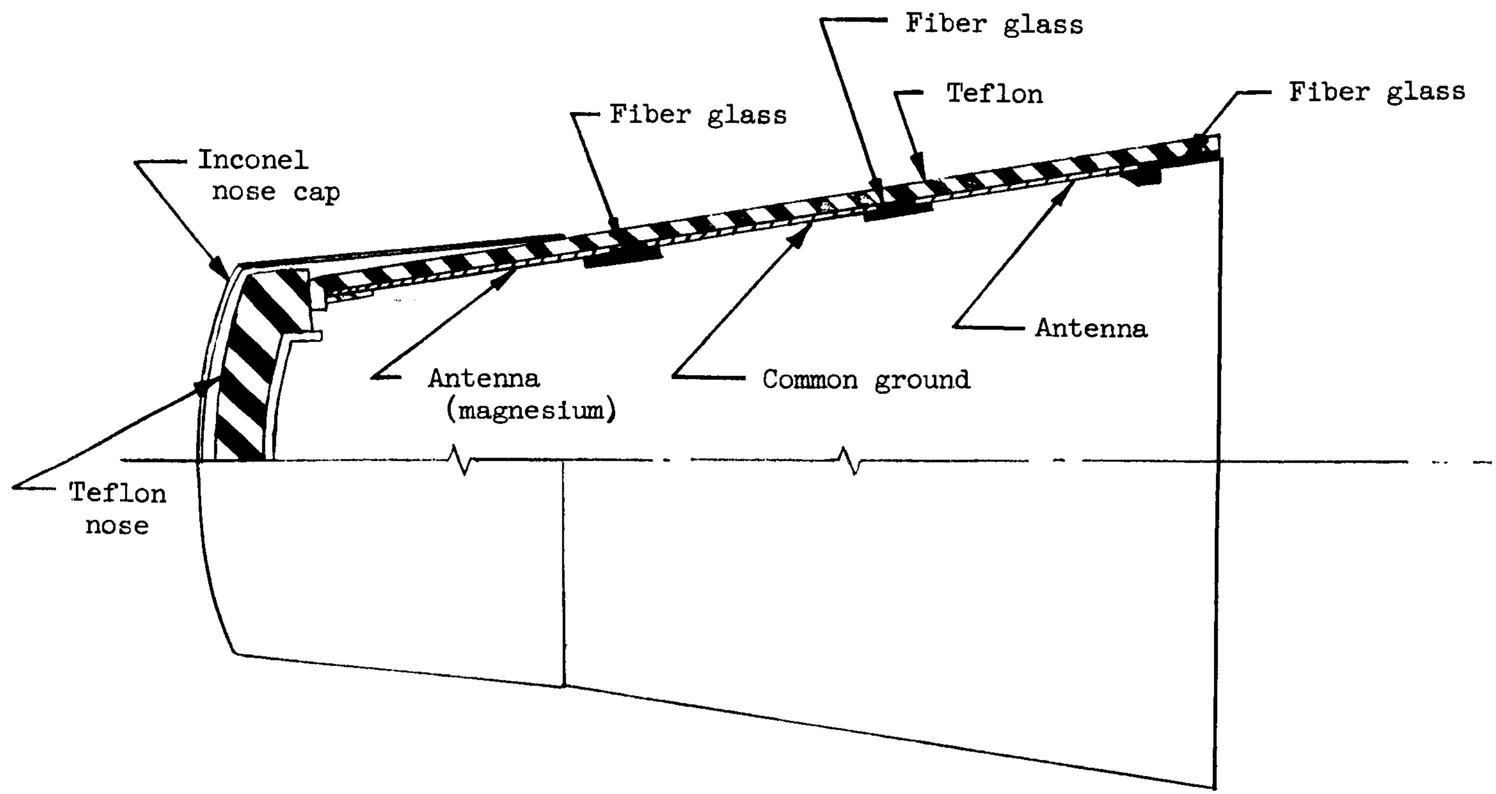

(b) Antenna arrangement.

Figure 1.- Concluded.

[redacted]

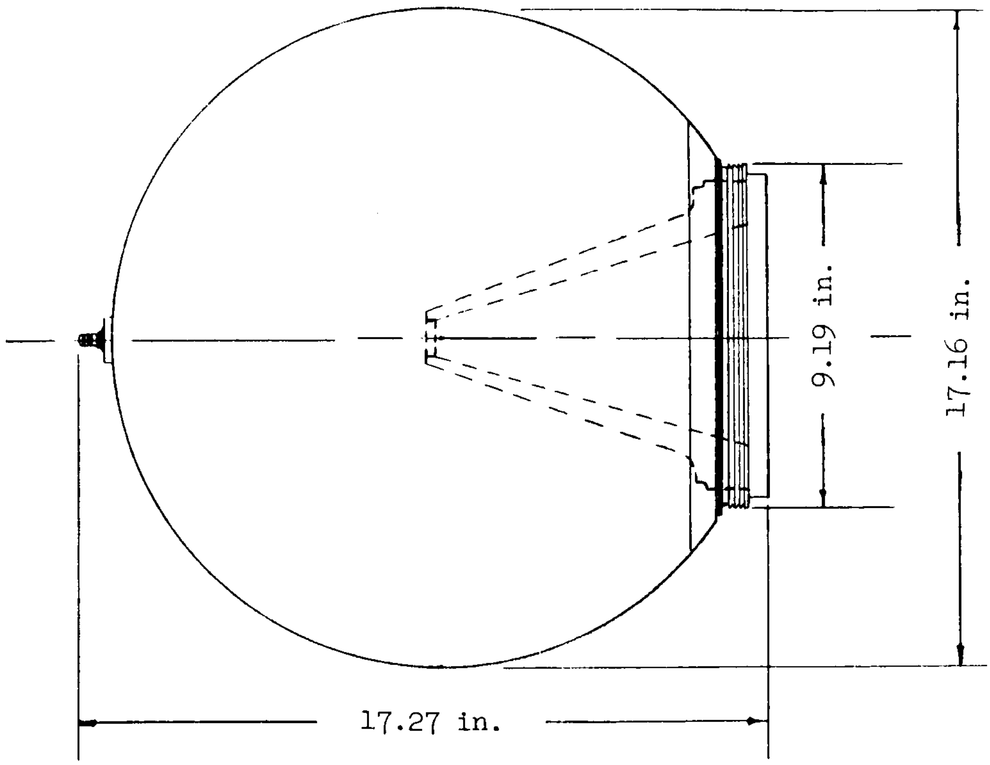

Dimensions		Weights		Performance	
Diameter, in.	17.16	Chamber, lb	10.00	Average pressure, lb/sq in.	500
Overall length, in.	17.27	Liner and insulation, lb	3.60	Average thrust, lb	860
Wall thickness, in.	0.03	Nozzle, lb	5.29	Total burning time, sec	43
Throat diameter, in.	1.10	Snap ring, lb	0.13	Total impulse, lb-sec	37,000
Exit diameter, in.	6.02	Igniter, lb	0.47	Propellant specific impulse, sec	265
Expansion ratio	30:1	Propellant, lb	139.6	Motor specific impulse, sec	233
		Burnout, lb	18.3		
		Total, lb	159.1		

Figure 2.- Cetus-I characteristics.

[redacted]

[redacted]

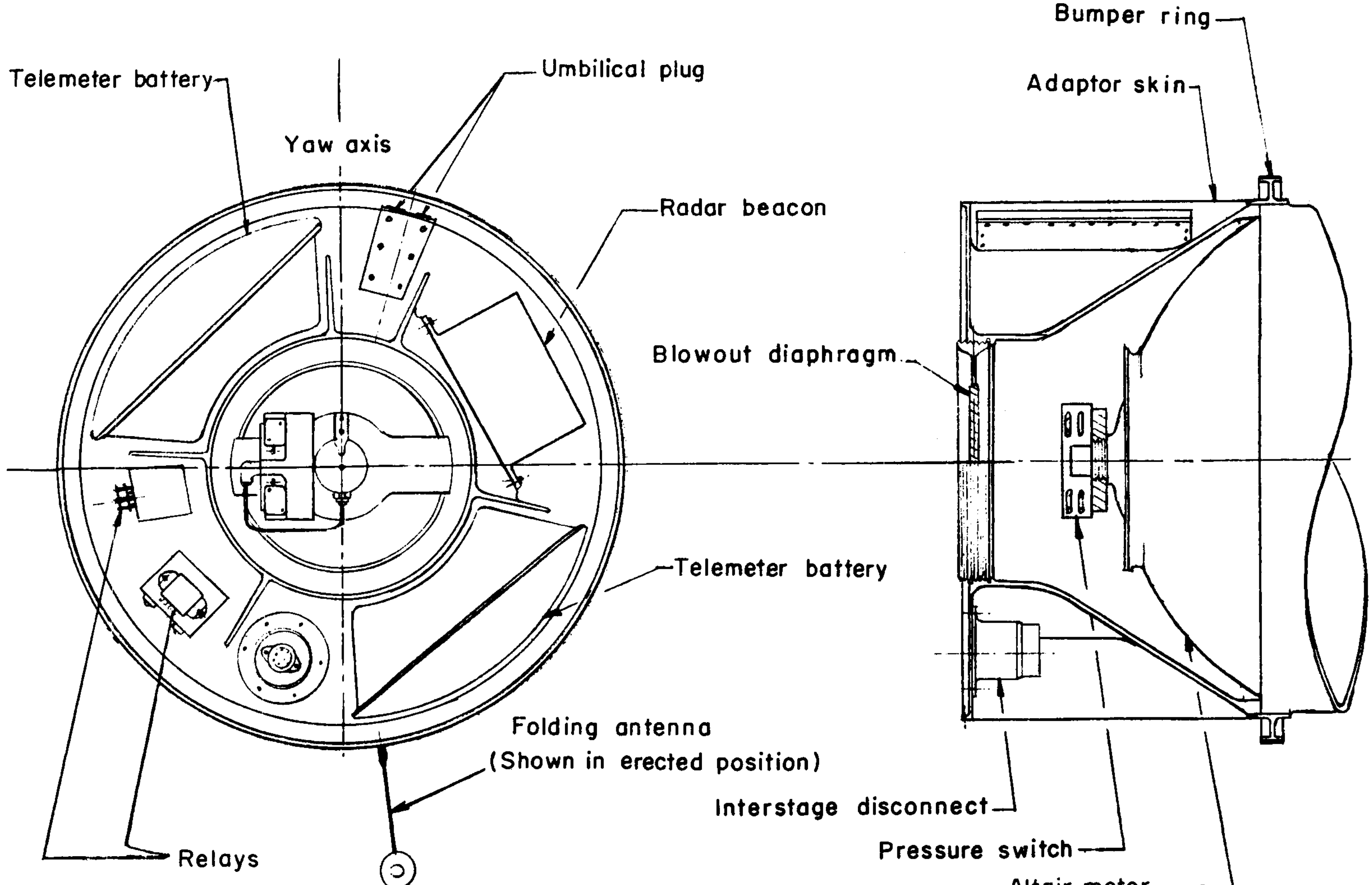

Figure 3.- Adaptor connecting fourth and fifth stages.

[redacted]

[redacted]

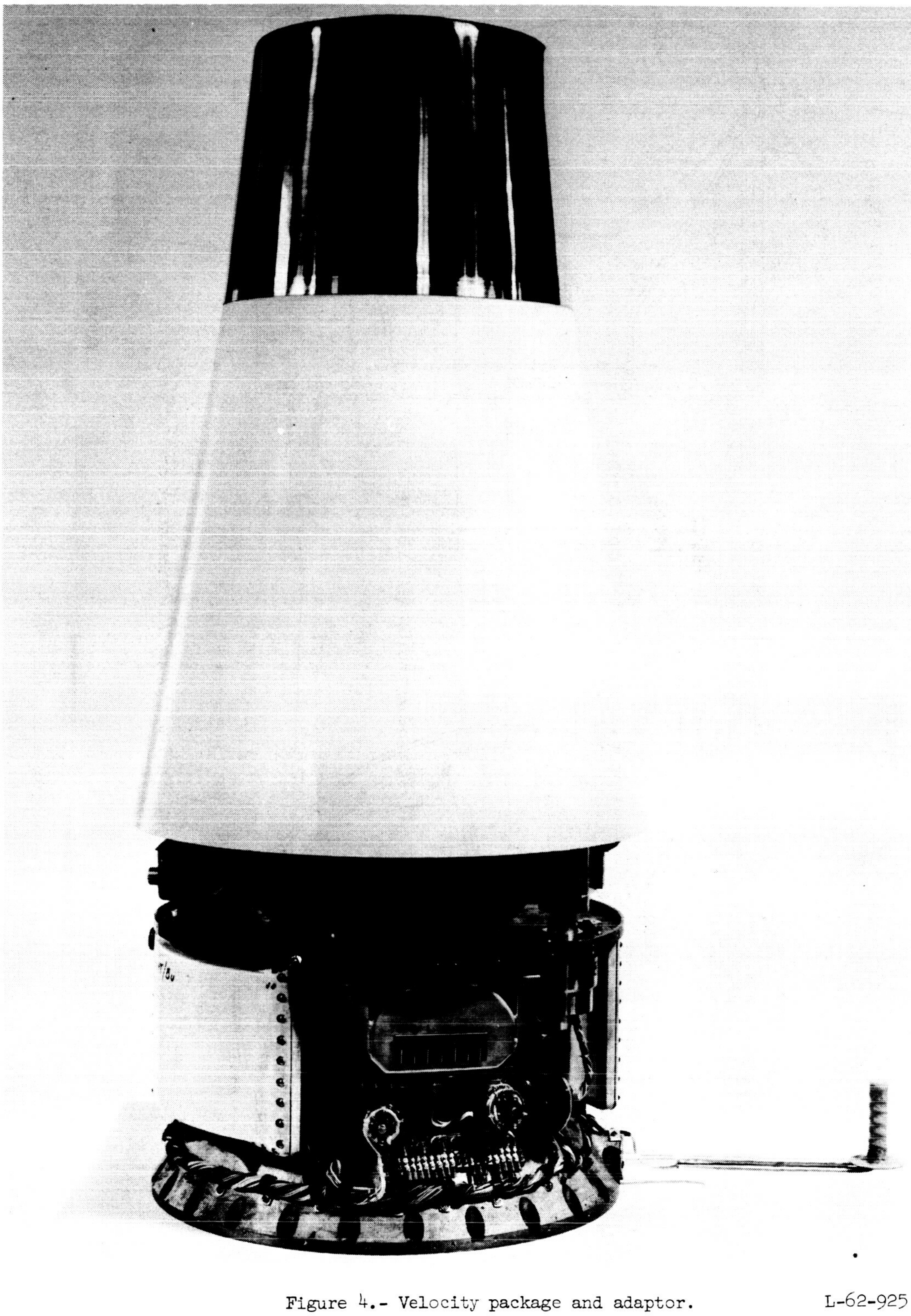

Figure 4.- Velocity package and adaptor. L-62-925

[redacted]

[redacted]

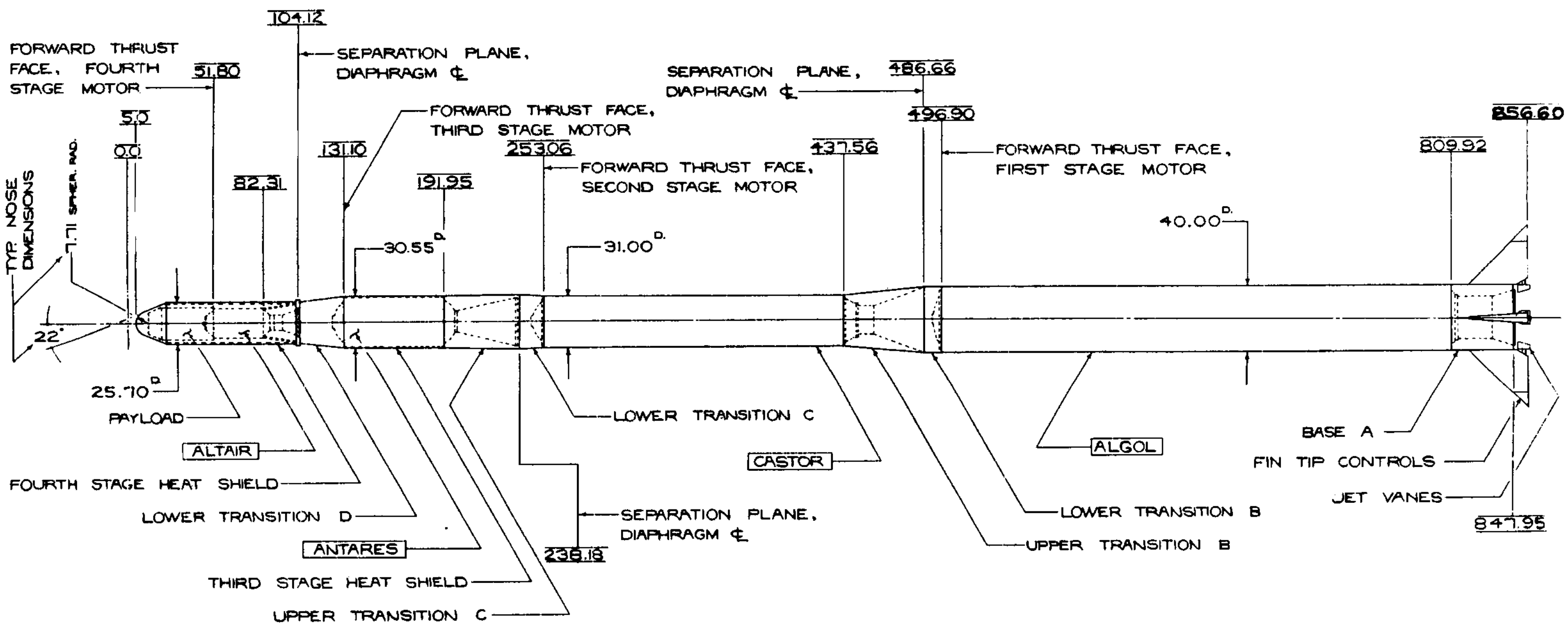

Figure 5.- Scout configuration. All dimensions are in inches.

[redacted]

[redacted]

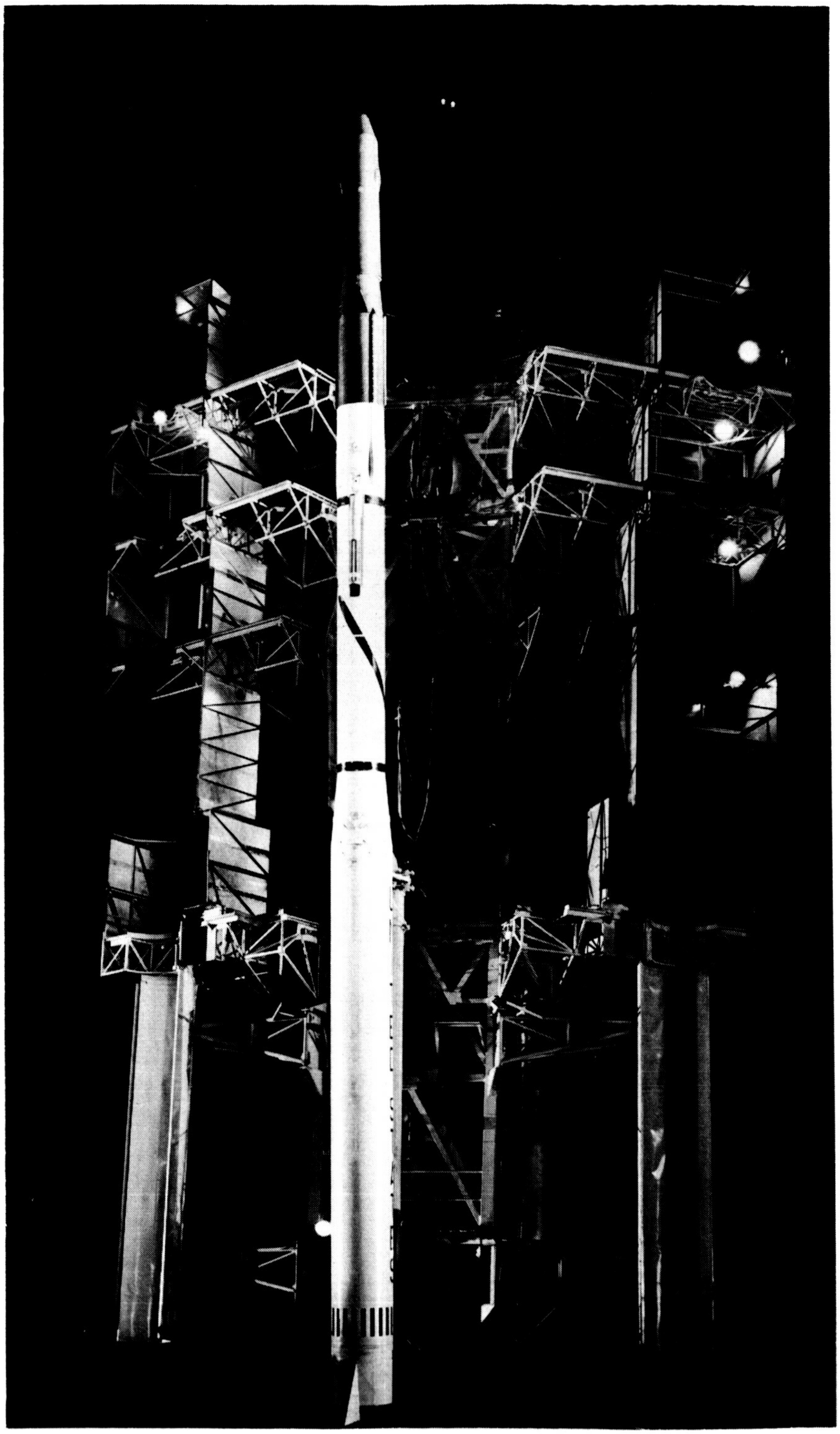

Figure 6.- Vehicle prior to launch. L-62-944

[redacted]

[redacted]

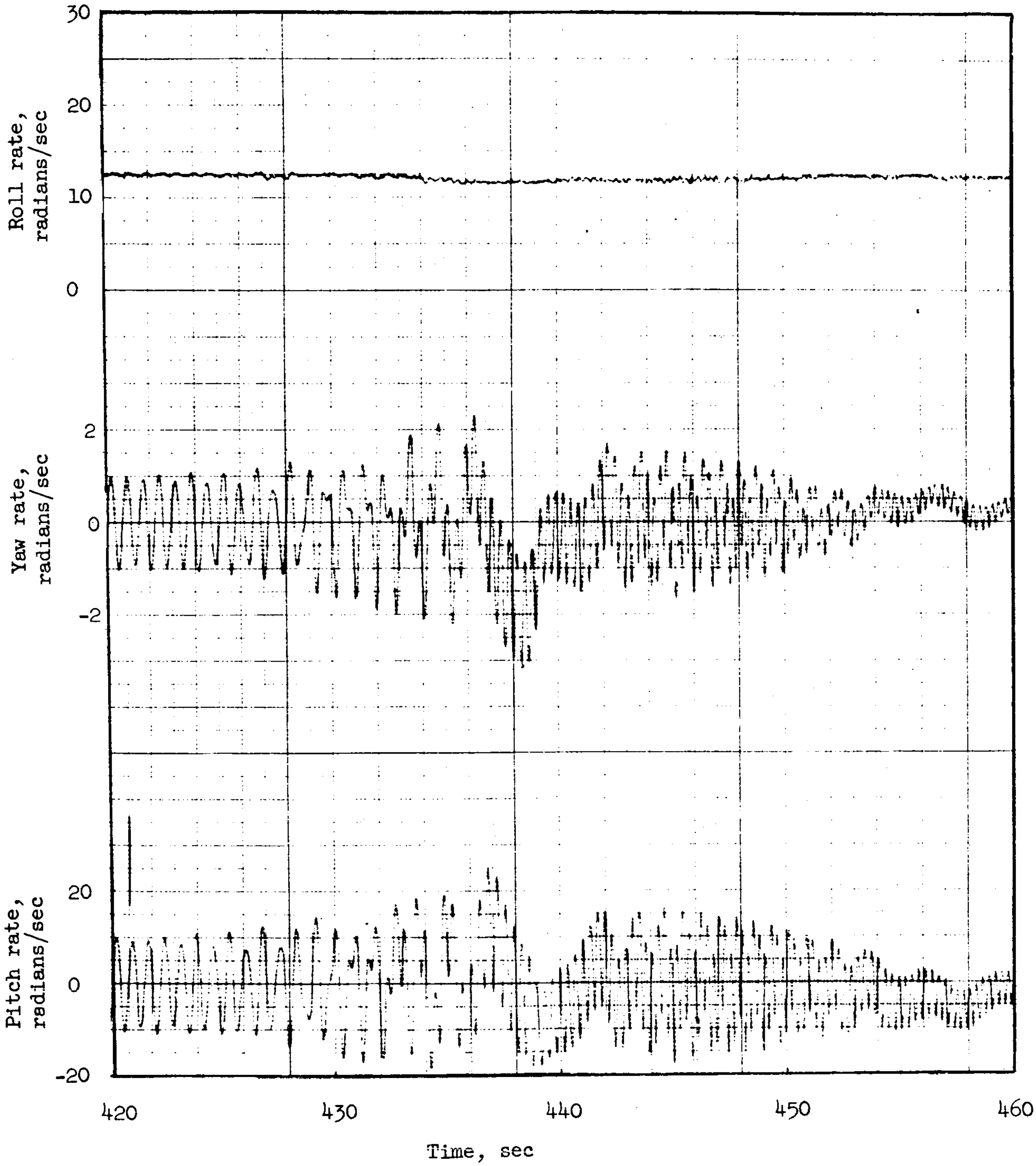

Figure 7.- Time histories measured by rate gyros.

[redacted]

[redacted]

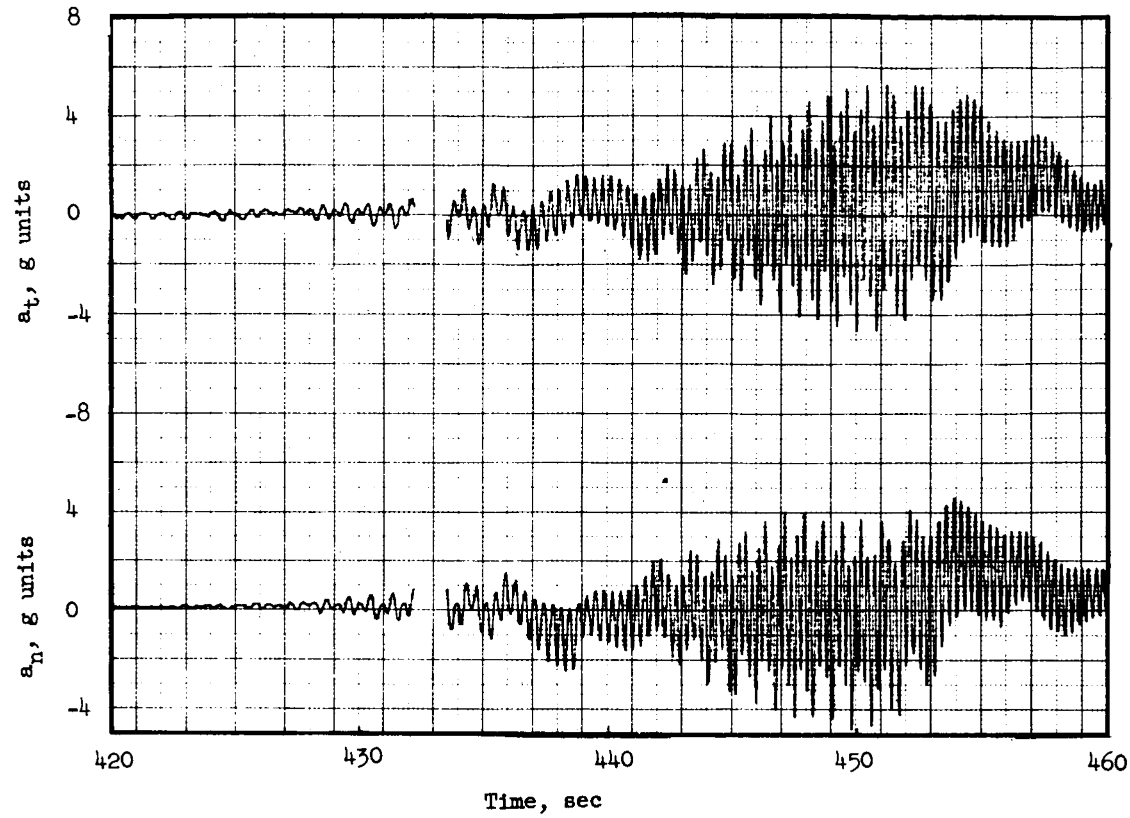

(a) Normal and transverse accelerometer time histories.

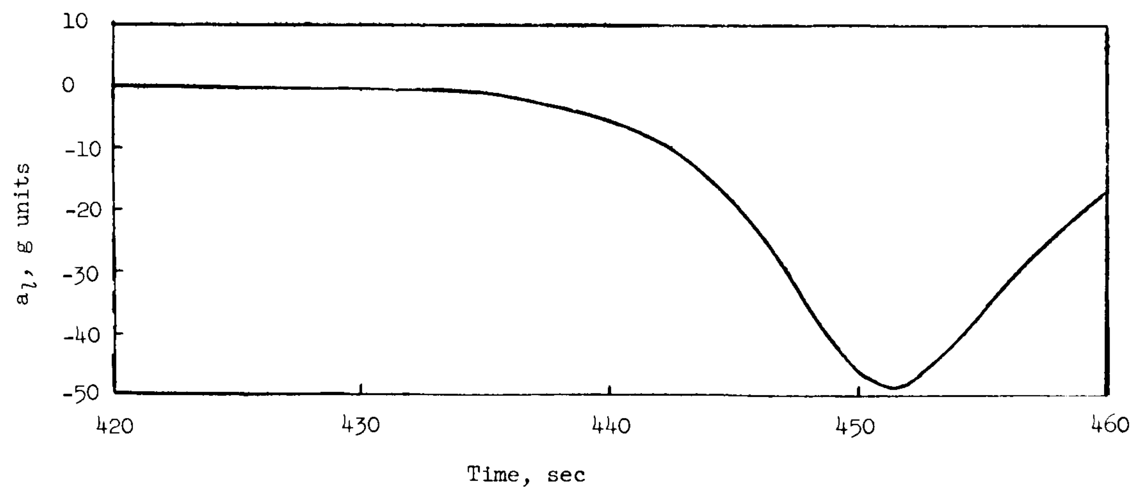

(b) Longitudinal accelerometer time history.

Figure 8.- Time histories of linear accelerometers.

[redacted]

[redacted]

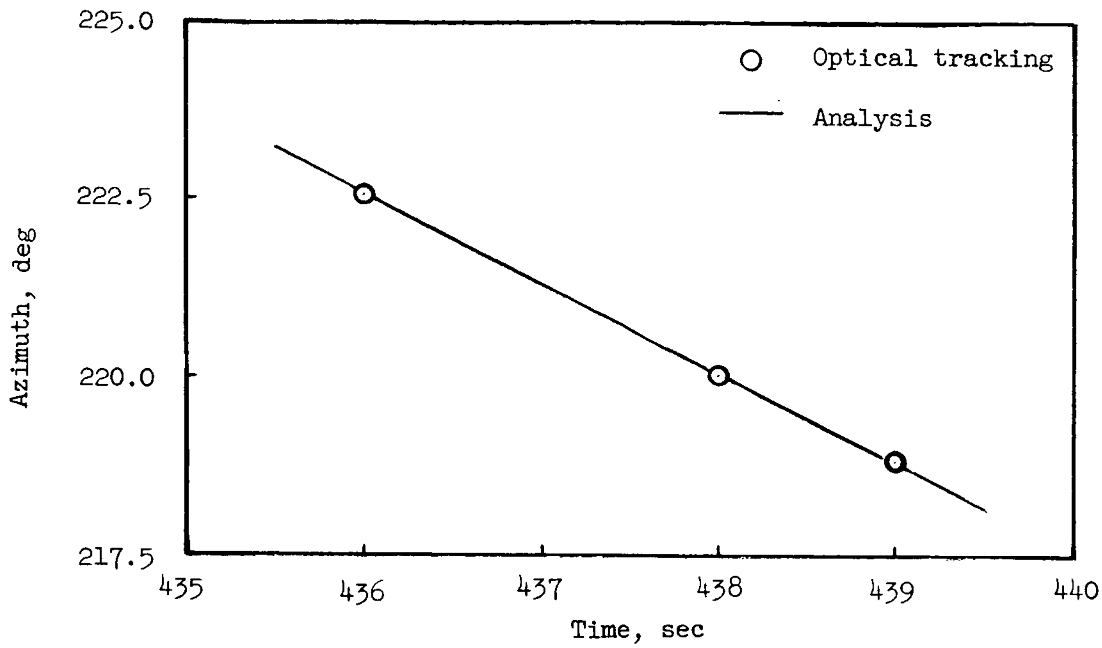

(a) Azimuth as a function of flight time.

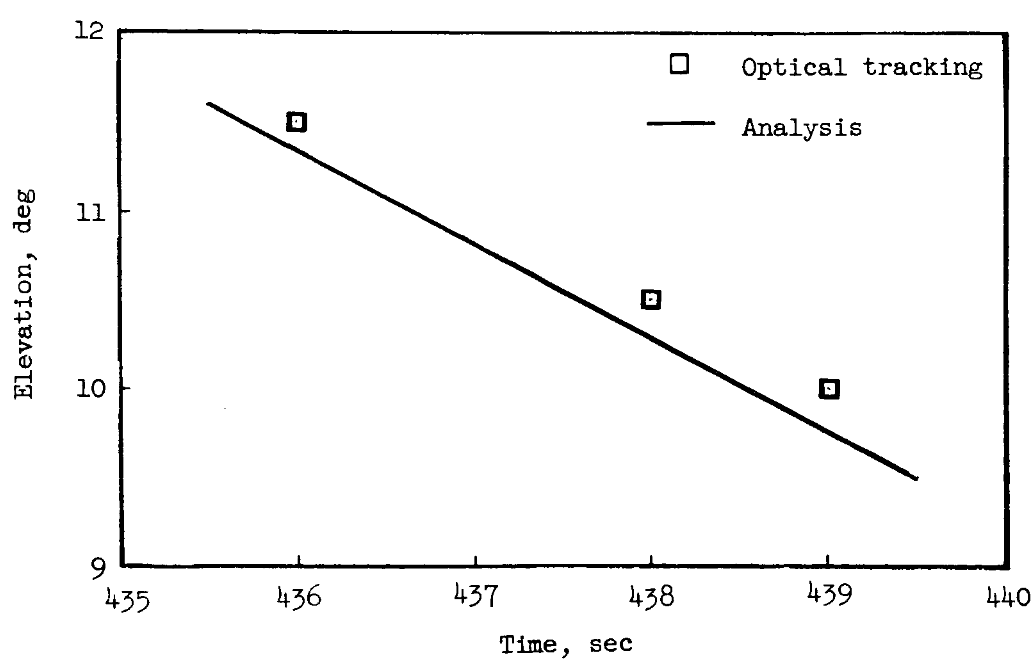

(b) Elevation as a function of flight time.

Figure 9.- Comparison of optical tracking measurements with dynamic trajectory analysis.

[redacted]

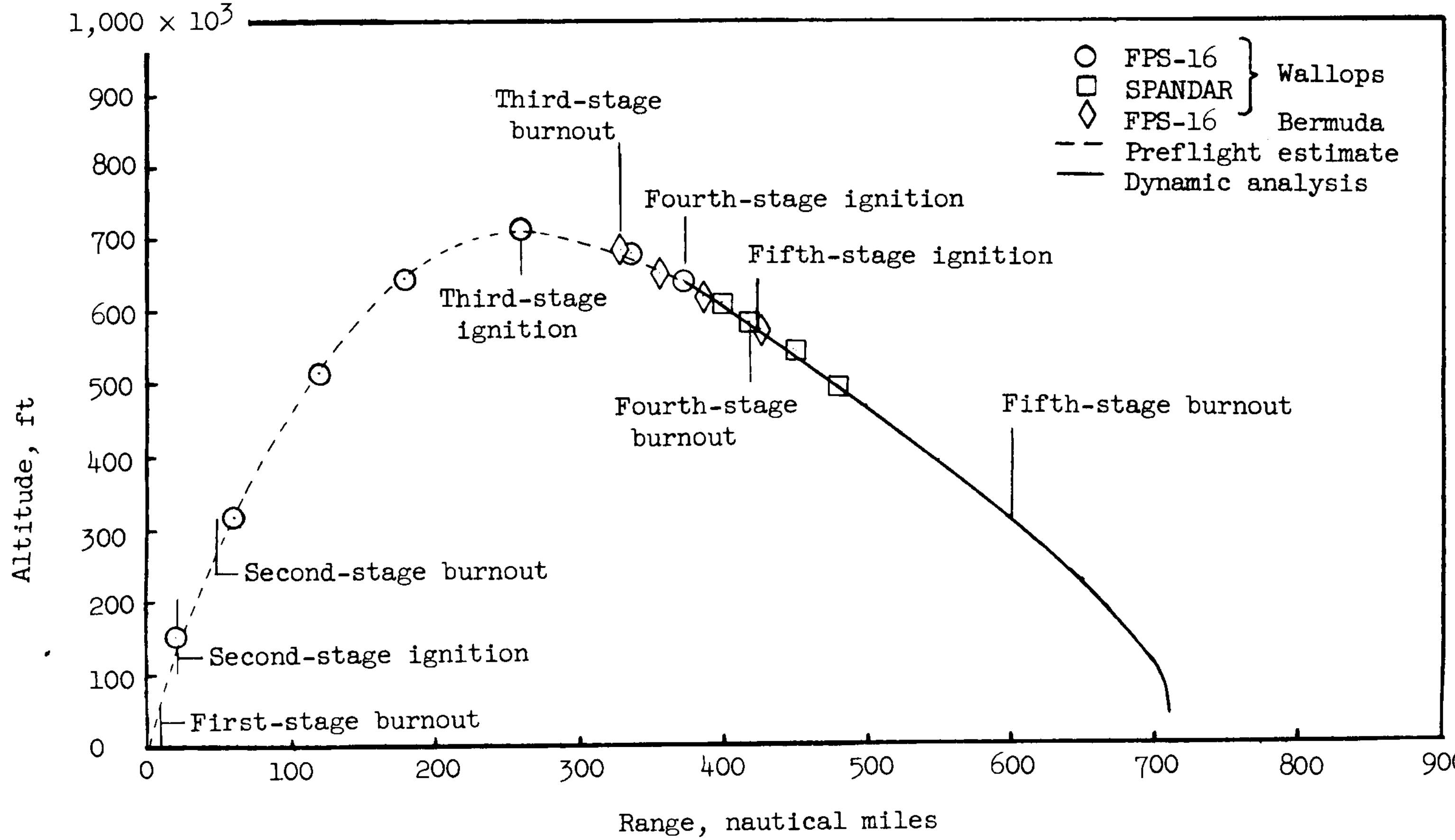

Figure 10.- Altitude-range trajectory.

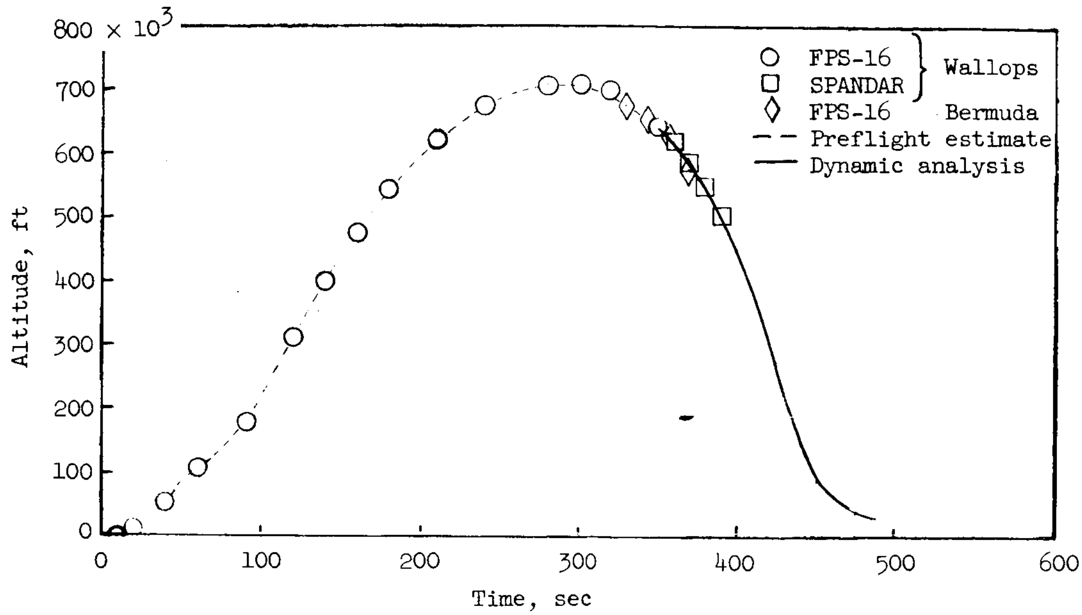

Figure 11.- Altitude-time trajectory.

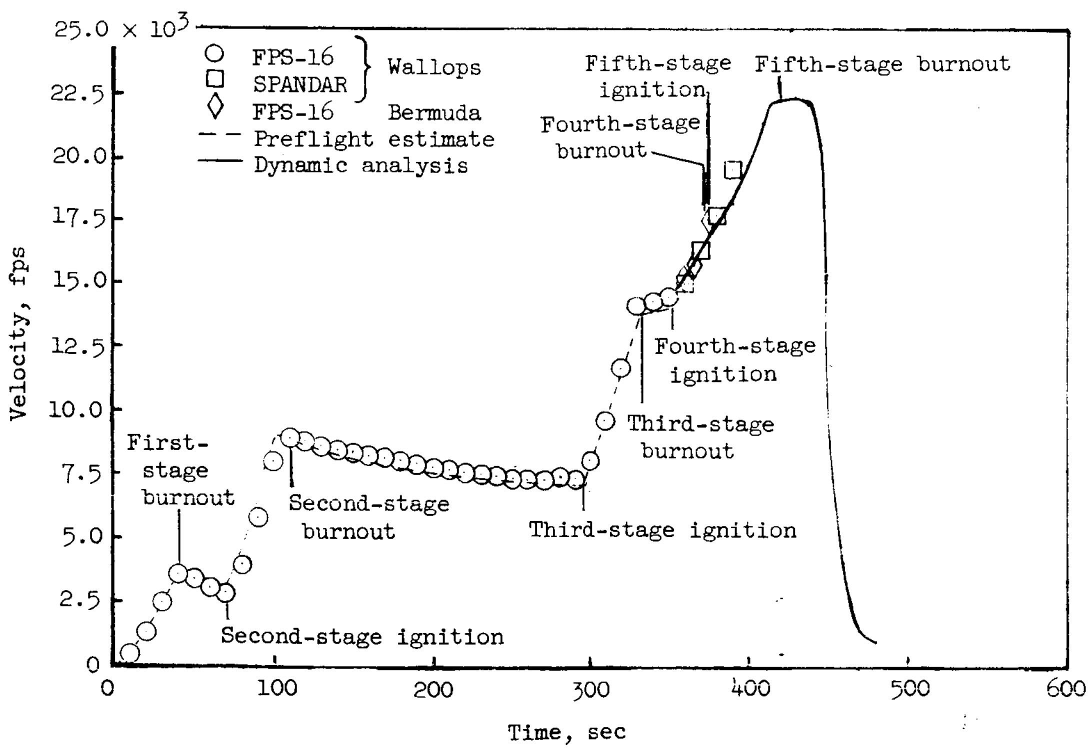

Figure 12.- Velocity-time trajectory.

[redacted]

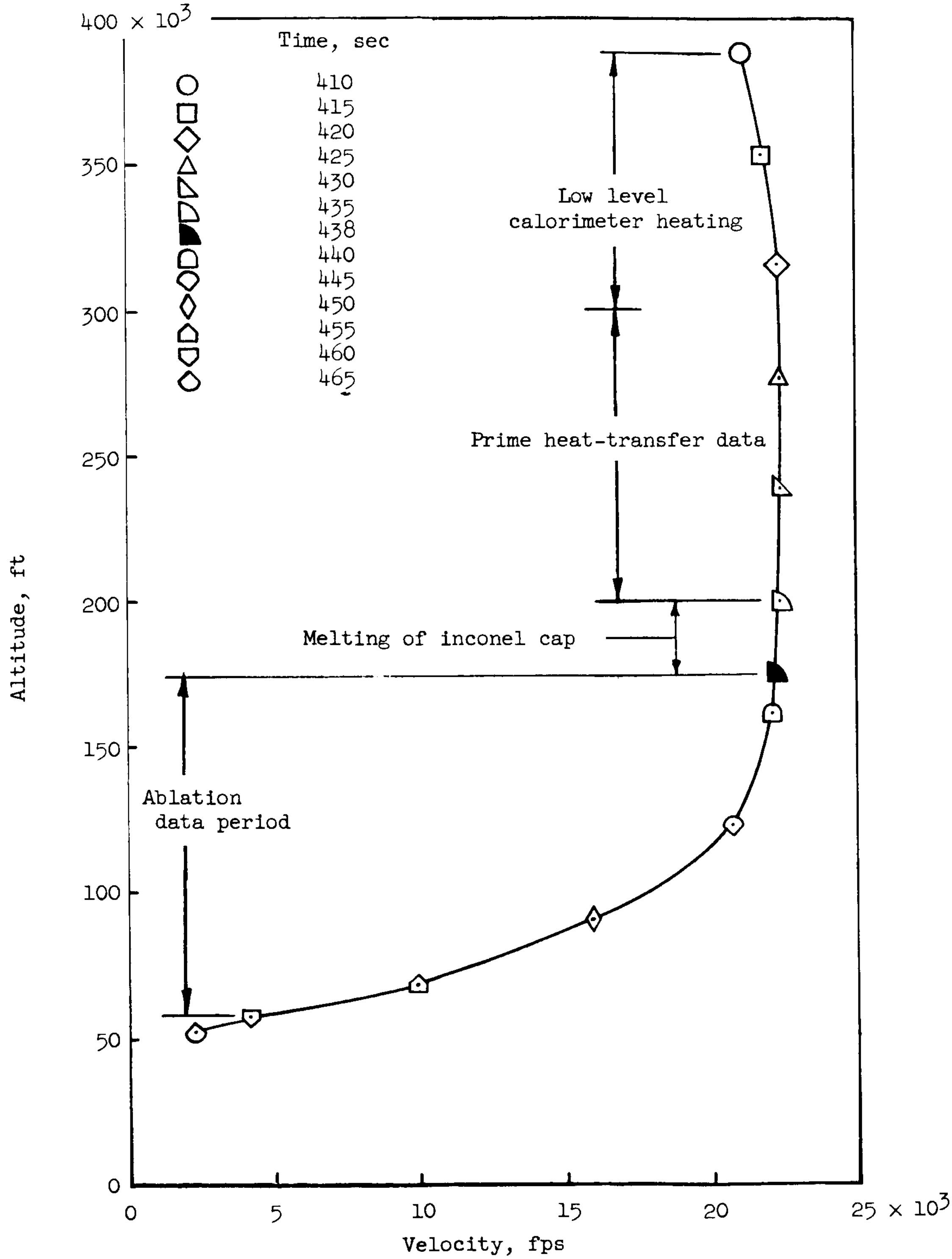

Figure 13.- Variation of flight test altitude with velocity.

[redacted]

[redacted]

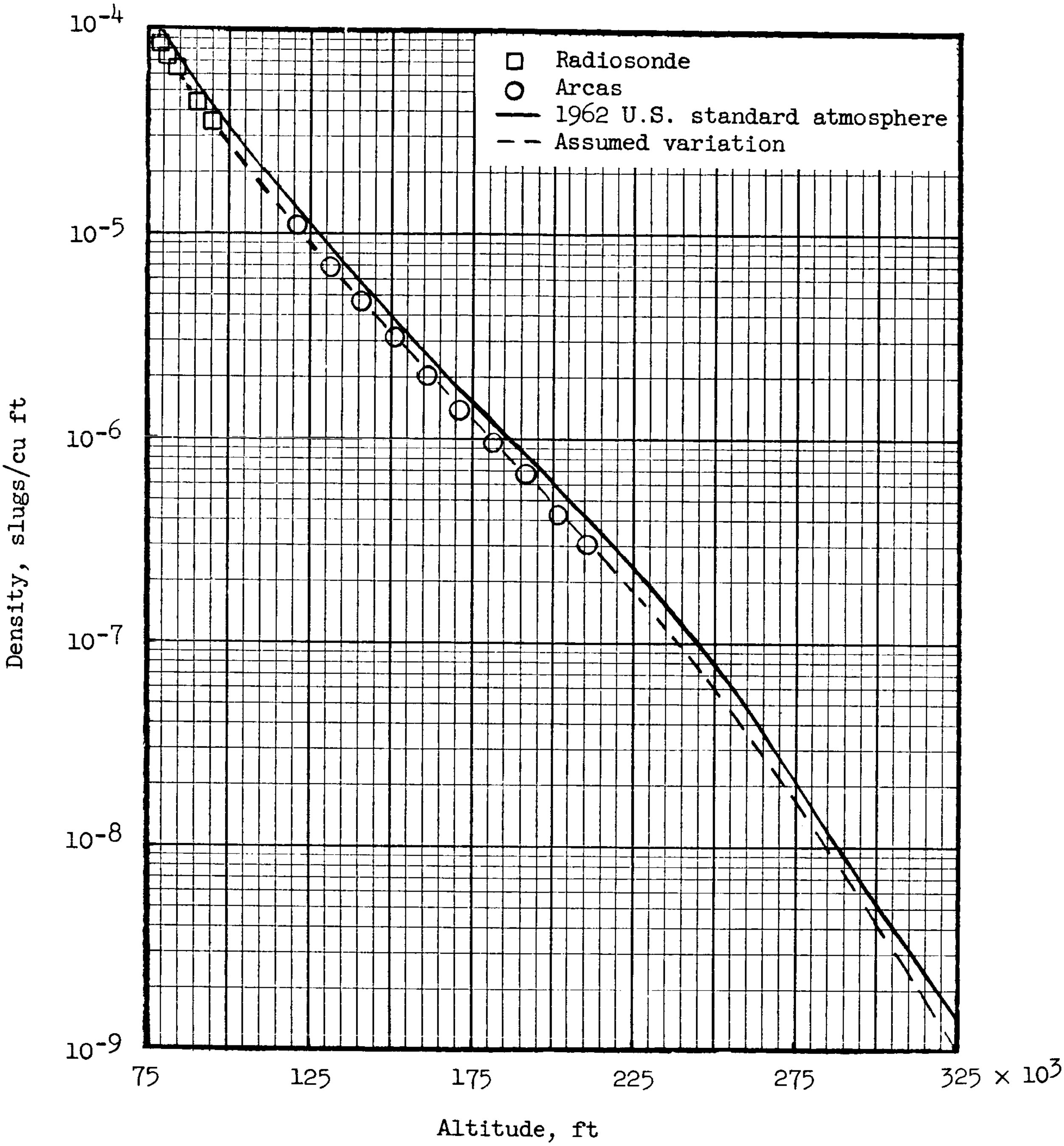

Figure 14.- Variation of flight test density with altitude.

[redacted]

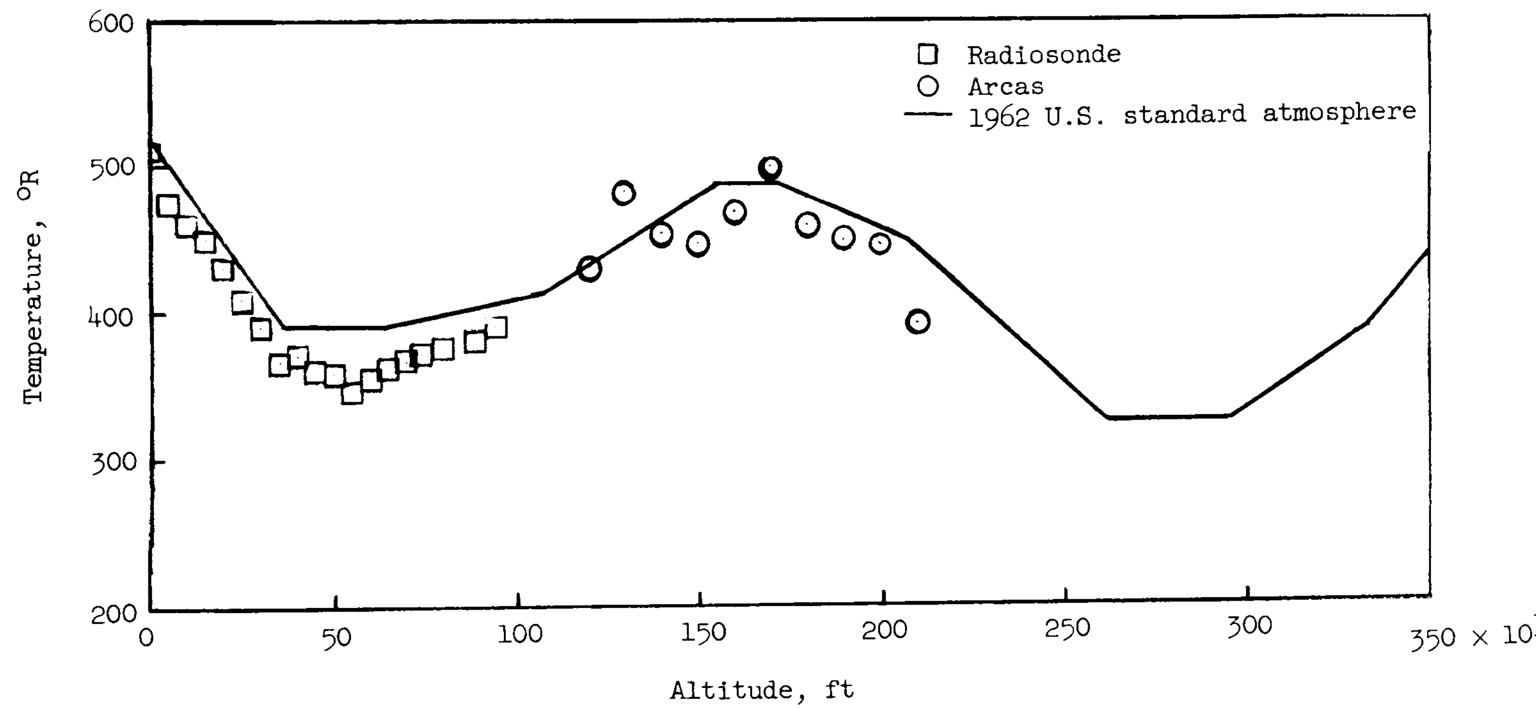

Figure 15.- Variation of flight test temperature with altitude.

[redacted]

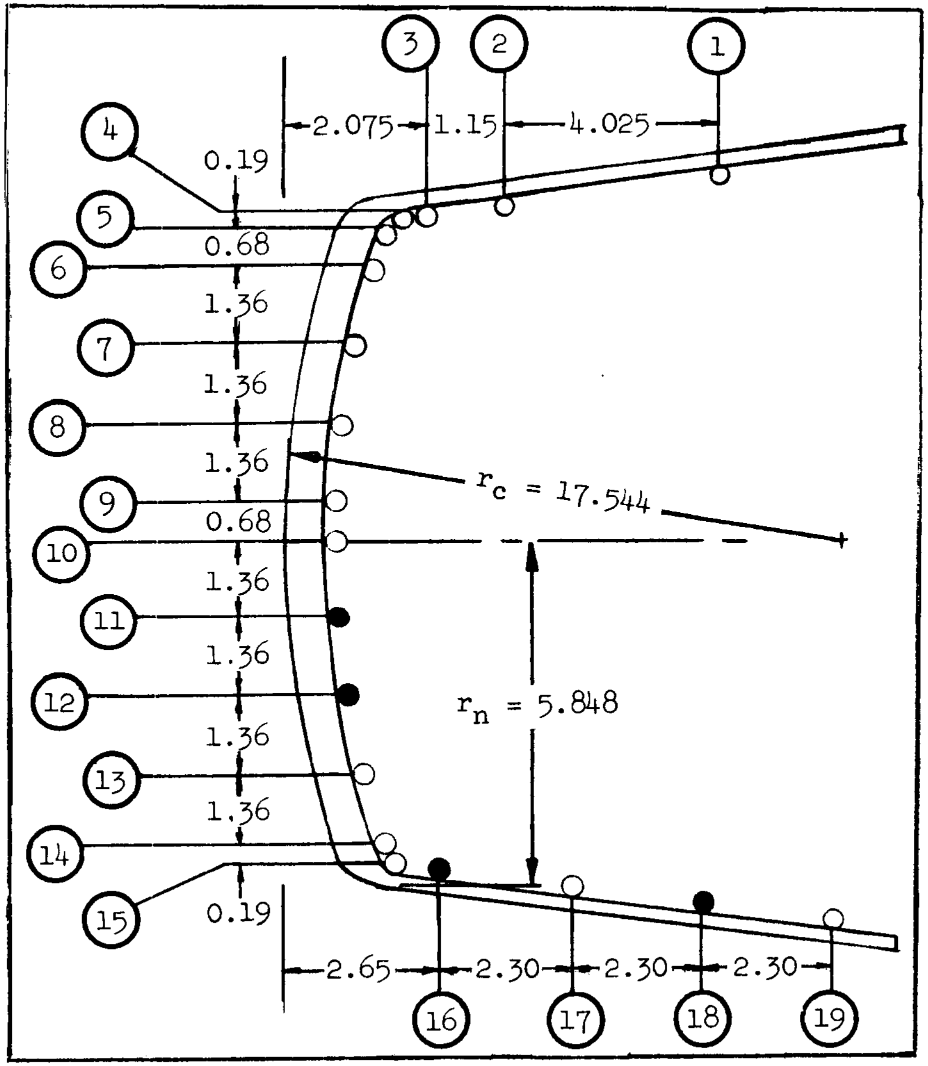

Thermocouple	Location	s/r_n	Inconel thickness, in.
1	Afterbody	2.1324	0.029
2	Afterbody	1.4411	.029
3	Afterbody	1.2436	.029
4	Corner	.9834	.055
5	Corner	.9444	.050
6	Front face	.8250	.050
7	Front face	.5827	.055
8	Front face	.3470	.058
9	Front face	.1163	.058
10	Front face	0	.058
*11	Front face	.2327	.058
*12	Front face	.4703	.058
13	Front face	.7044	.056
14	Corner	.9444	.049
15	Corner	.9834	.052
*16	Afterbody	1.3423	.029
17	Afterbody	1.7374	.029
*18	Afterbody	2.1324	.029
19	Afterbody	2.5275	.029

*Inoperative thermocouples.

Figure 16.- Inconel calorimeter thermocouple locations and wall thicknesses. All dimensions are in inches.

[redacted]

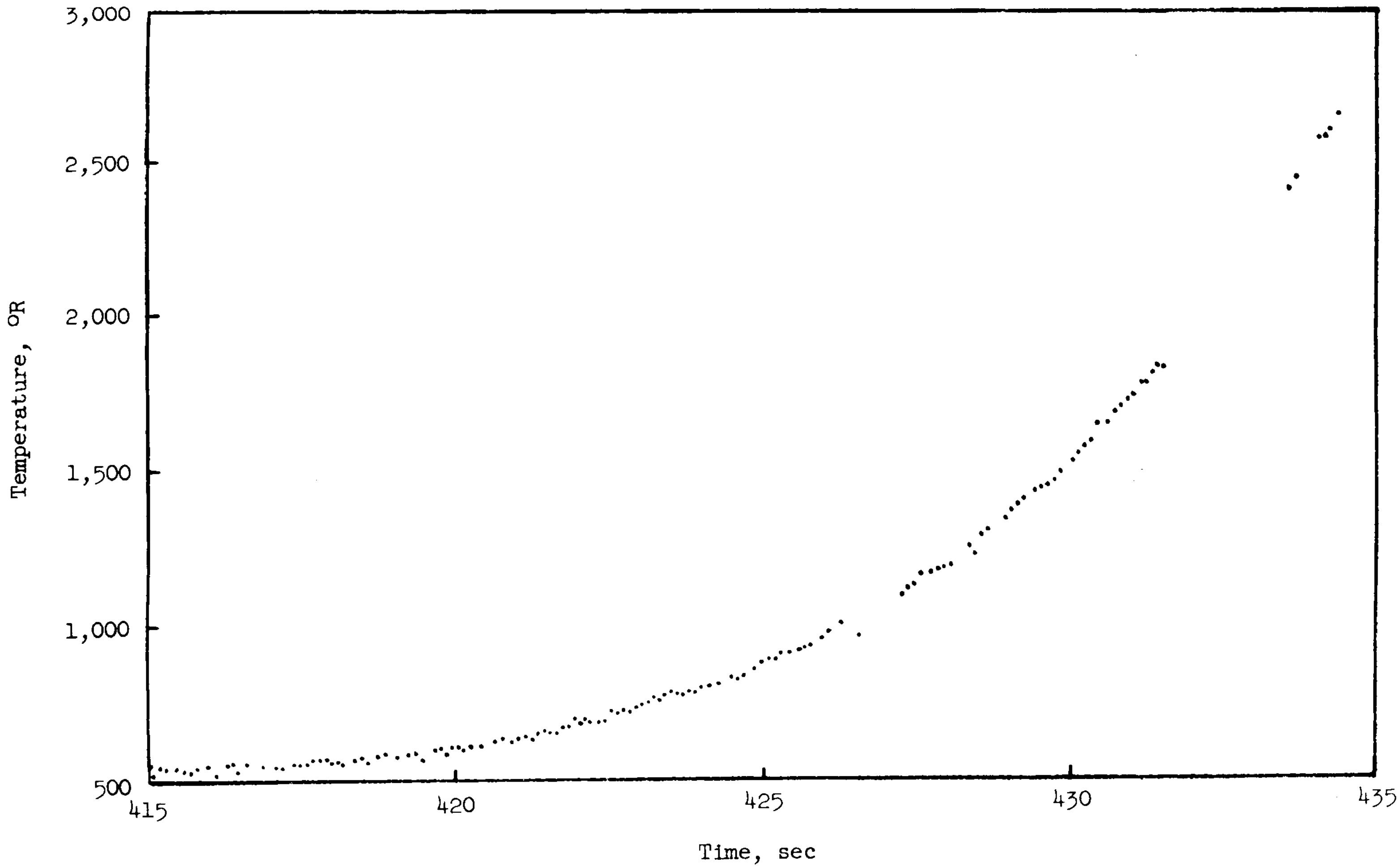

Figure 17.- Typical measured inside surface temperature time history. Thermocouple 10.

[redacted]

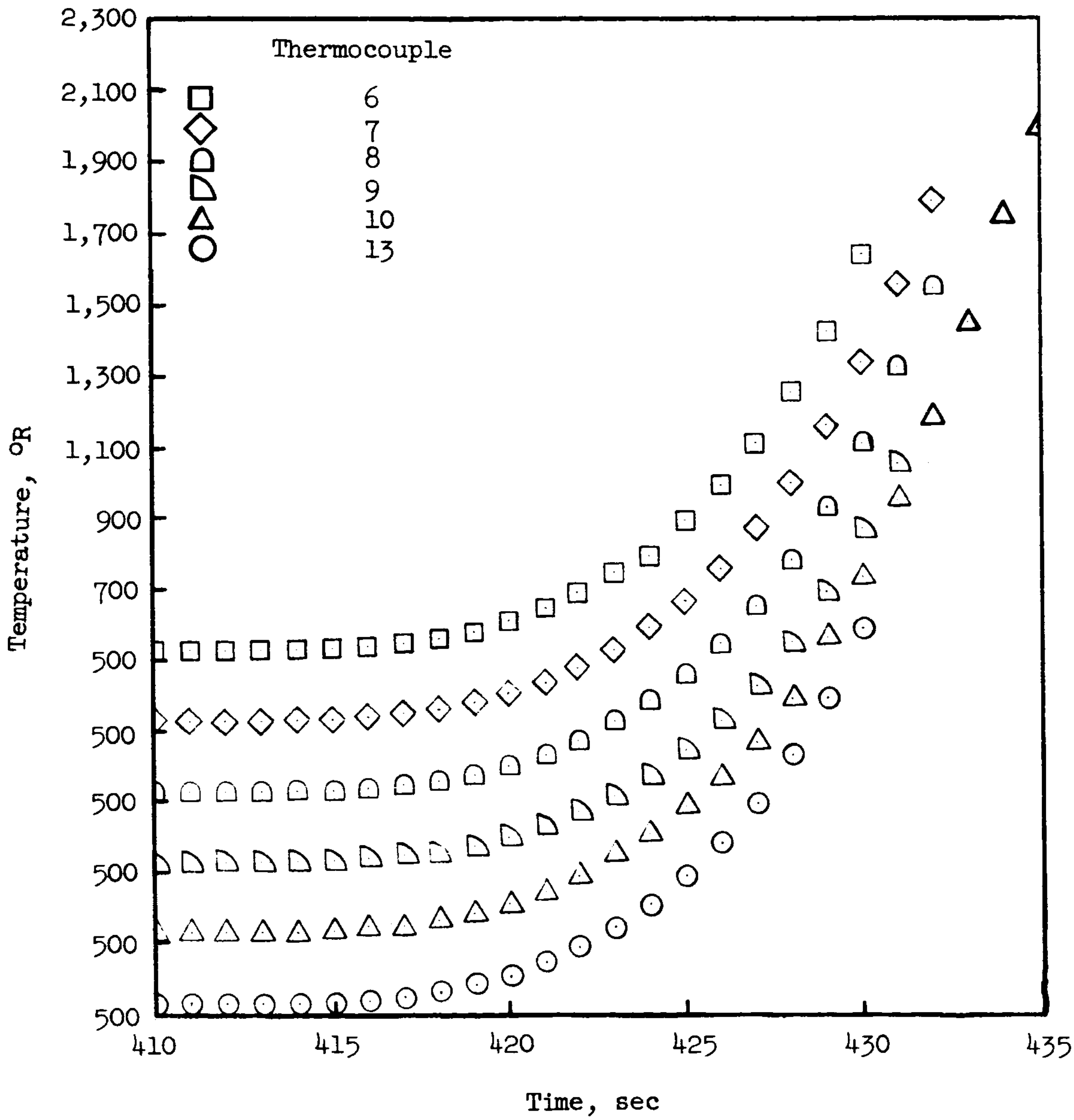

(a) Nose face locations.

Figure 18.- Computed outside surface temperature histories.

[redacted]

[redacted]

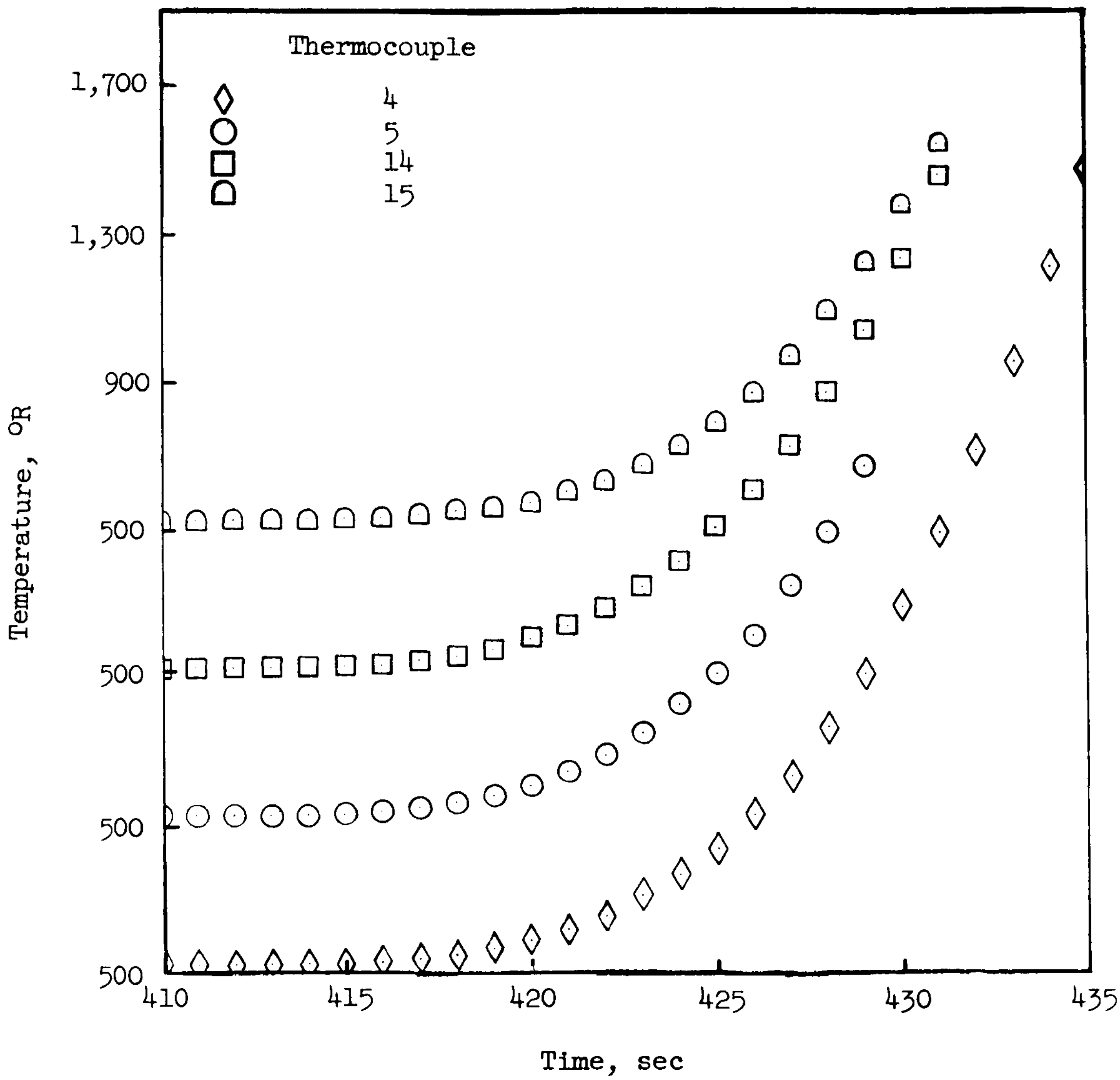

(b) Corner locations.

Figure 18.- Continued.

[redacted]

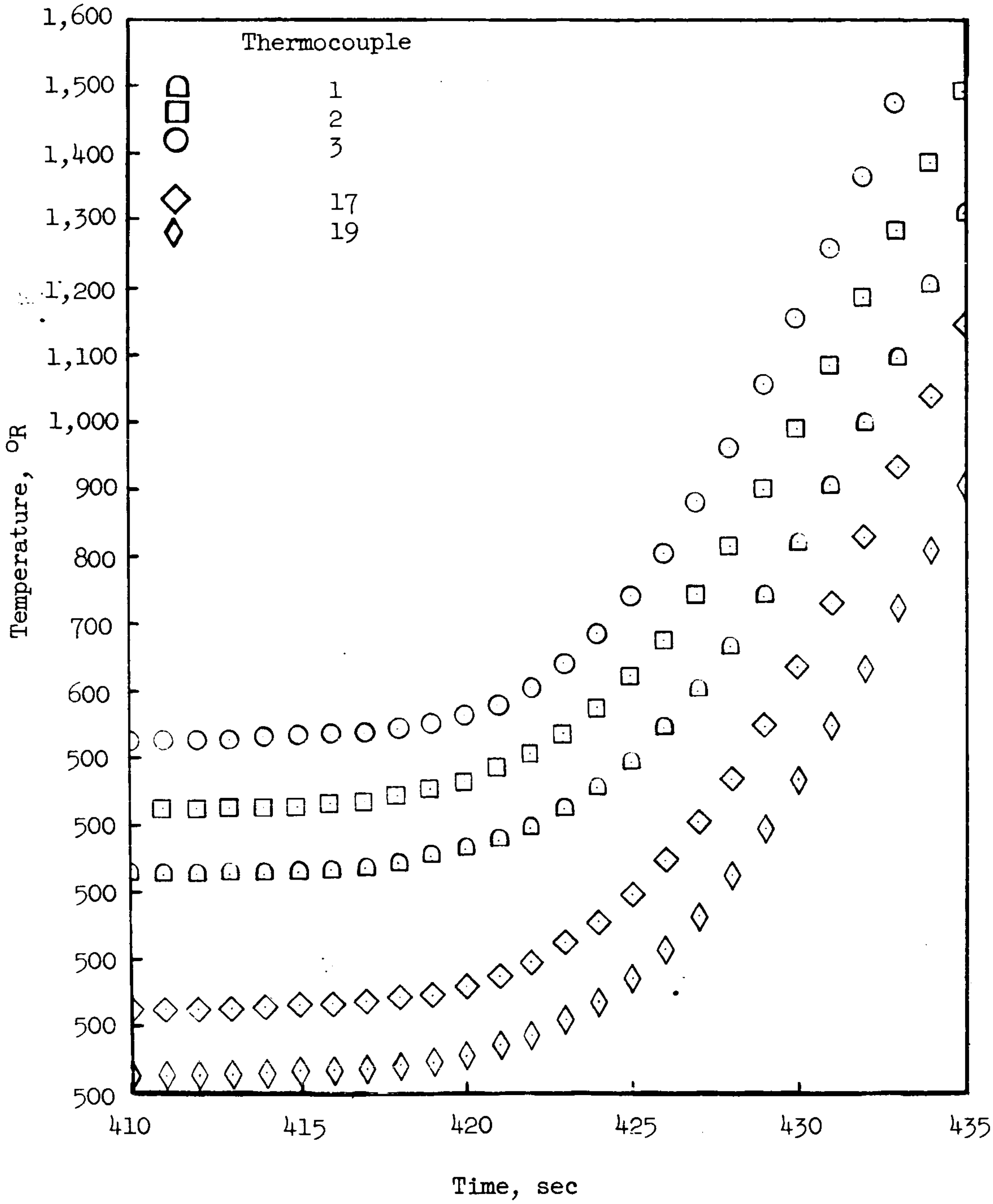

(c) Forebody locations.

Figure 18.- Concluded.

[redacted]

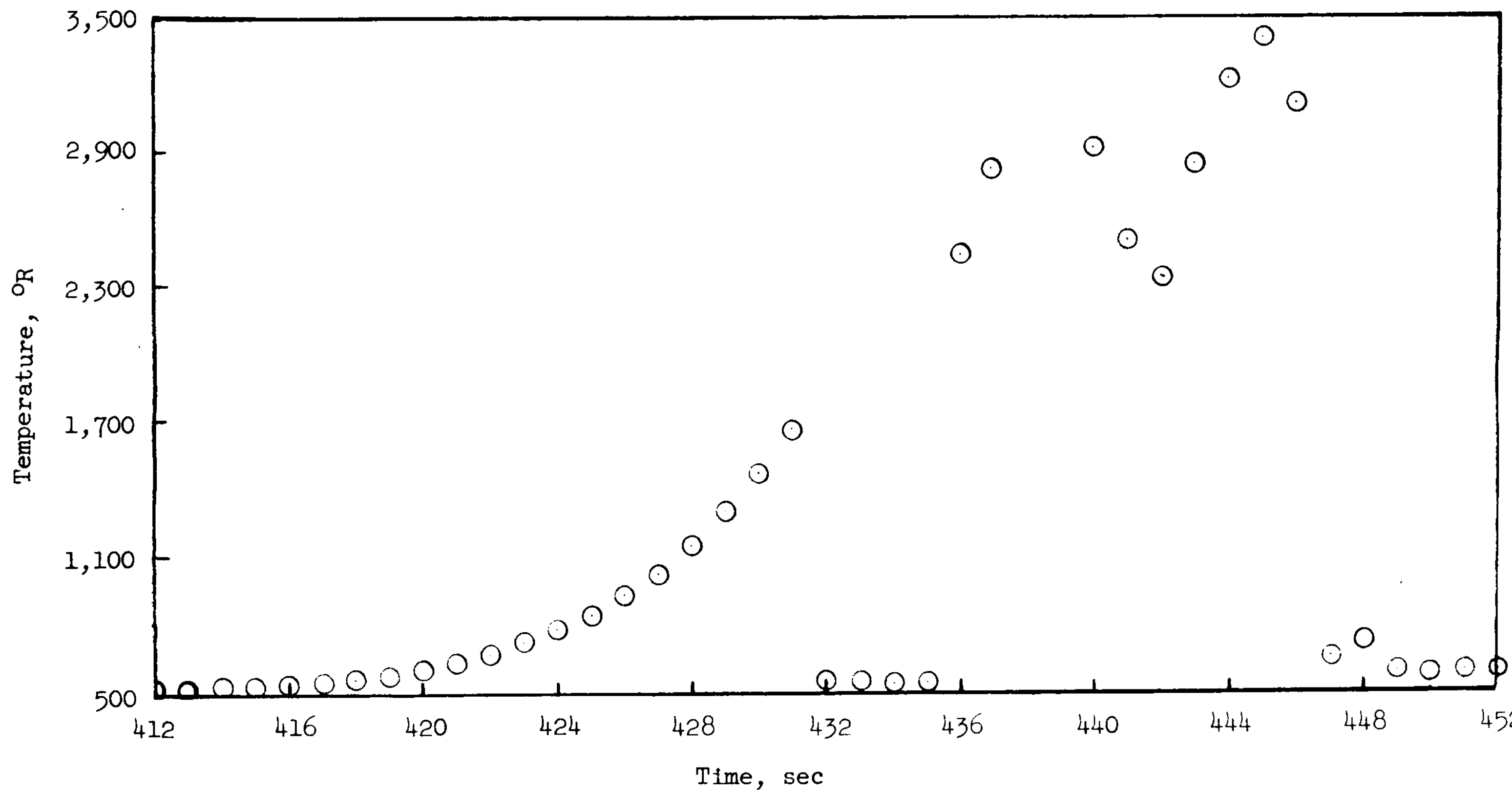

Figure 19.- Anomaly effect in thermocouple measurements. Thermocouple 7.

[redacted]

[redacted]

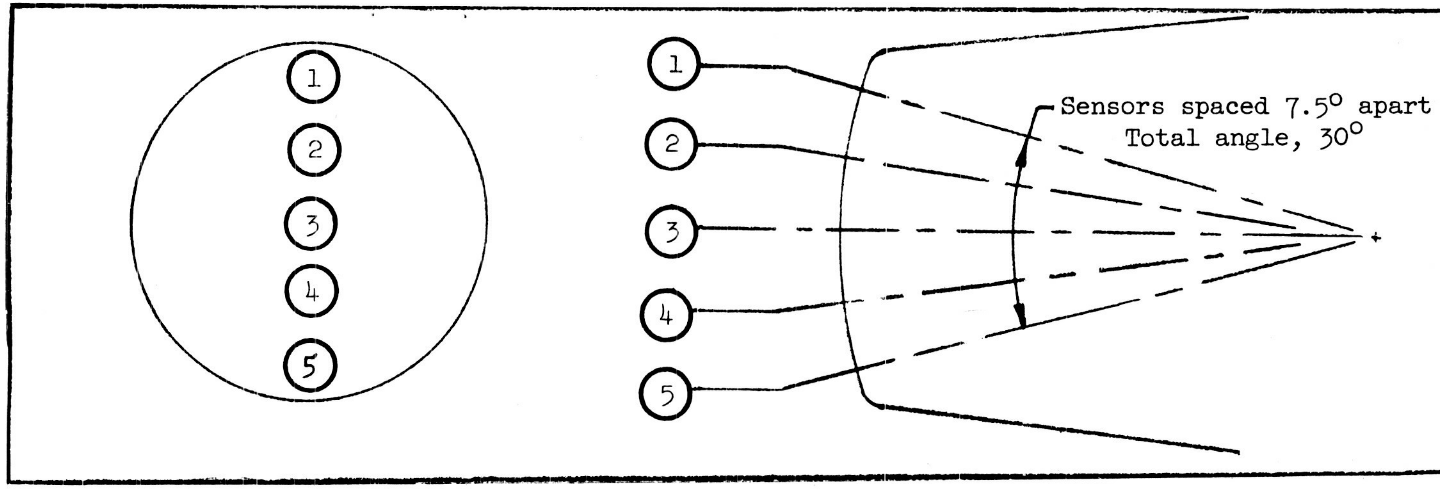

Figure 20.- Ablation sensor locations.

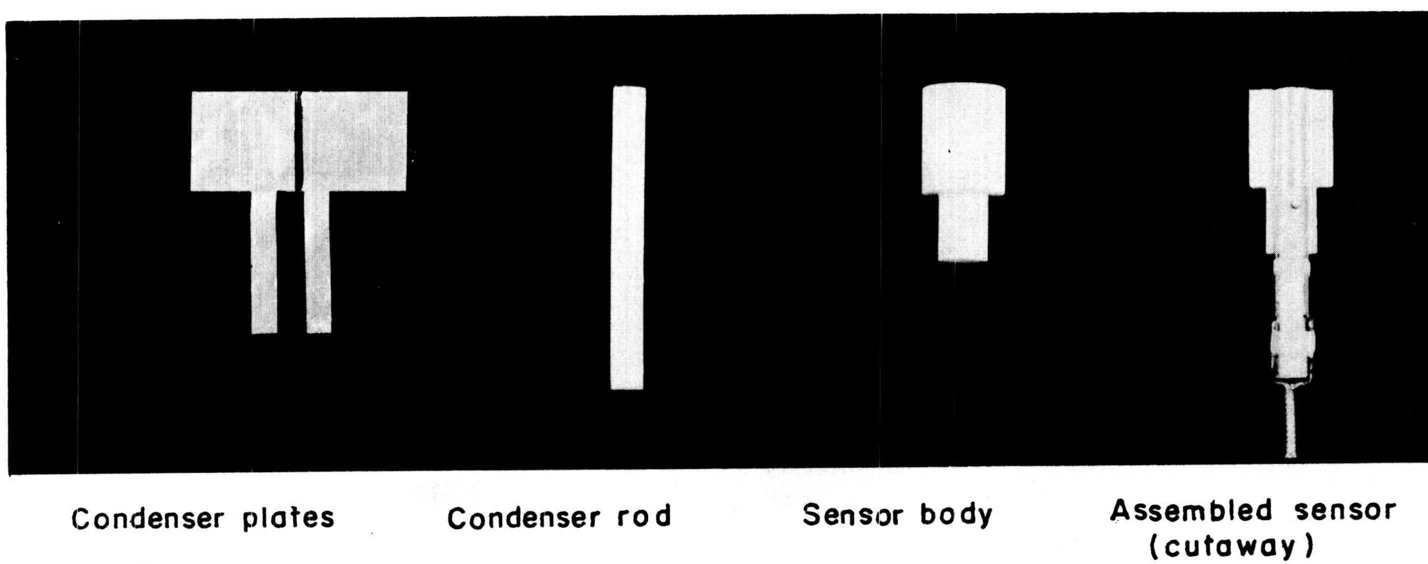

Figure 21.- Ablation sensor components.

L-59-4102

[redacted]

[redacted]

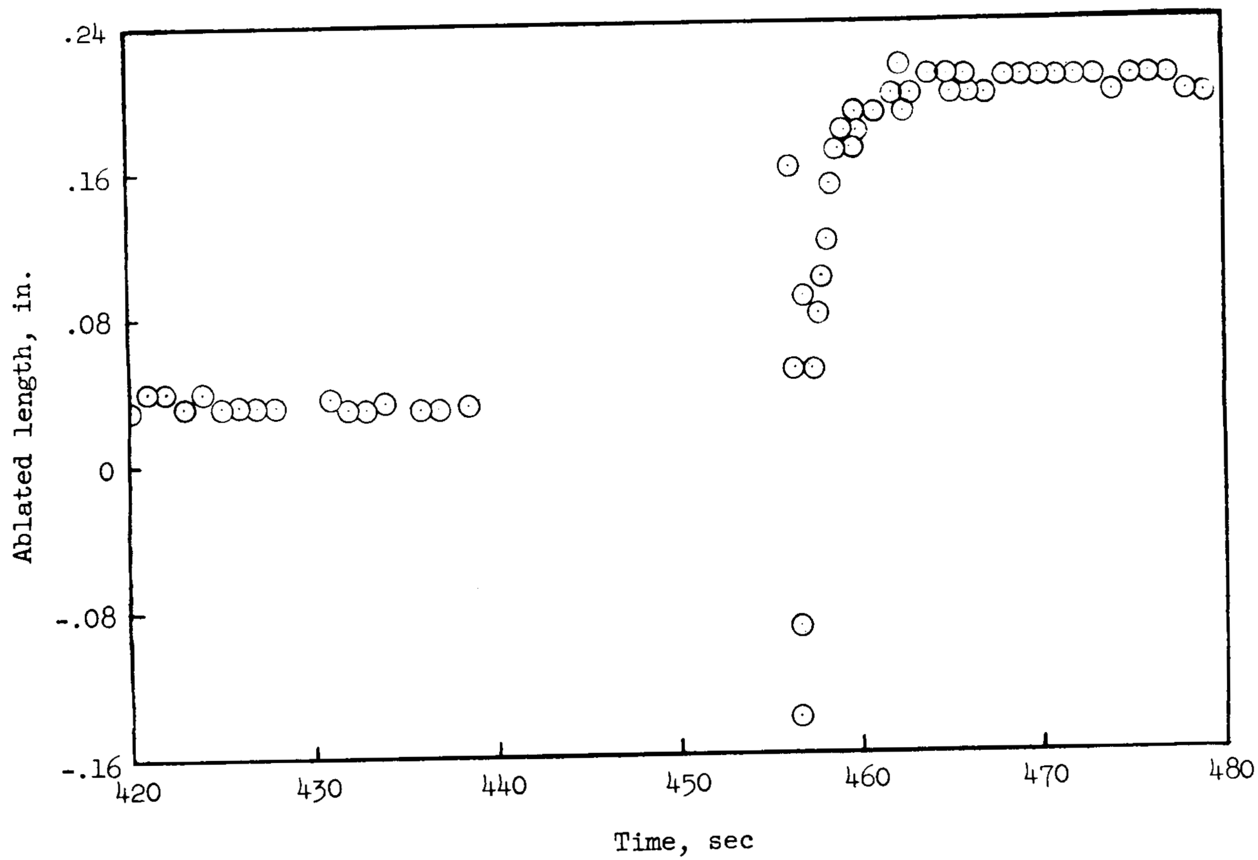

Figure 22.- Typical ablation sensor measurements.

[redacted]

[redacted]

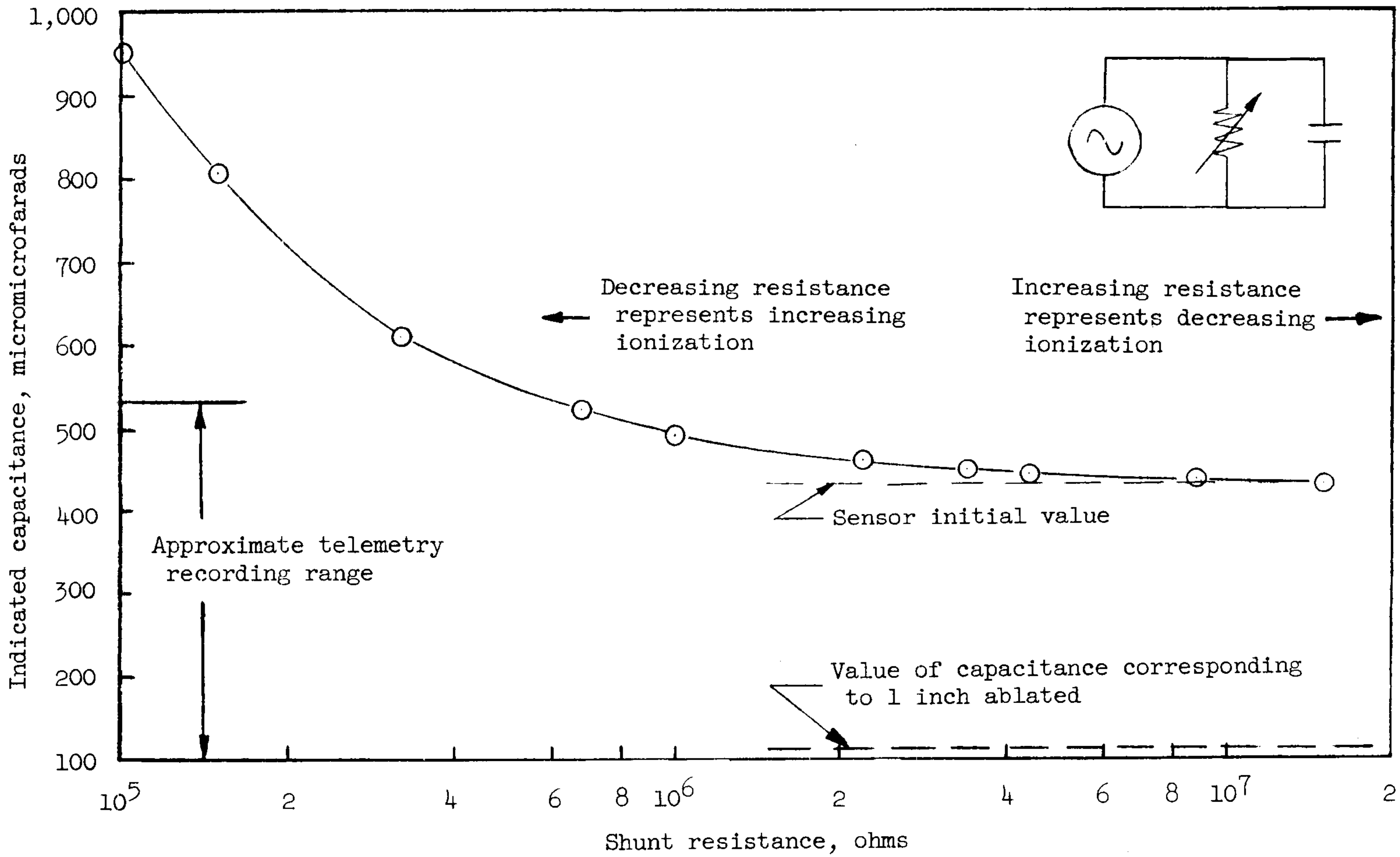

Figure 23.- Ablation sensor circuit test results.

[redacted]

[redacted]

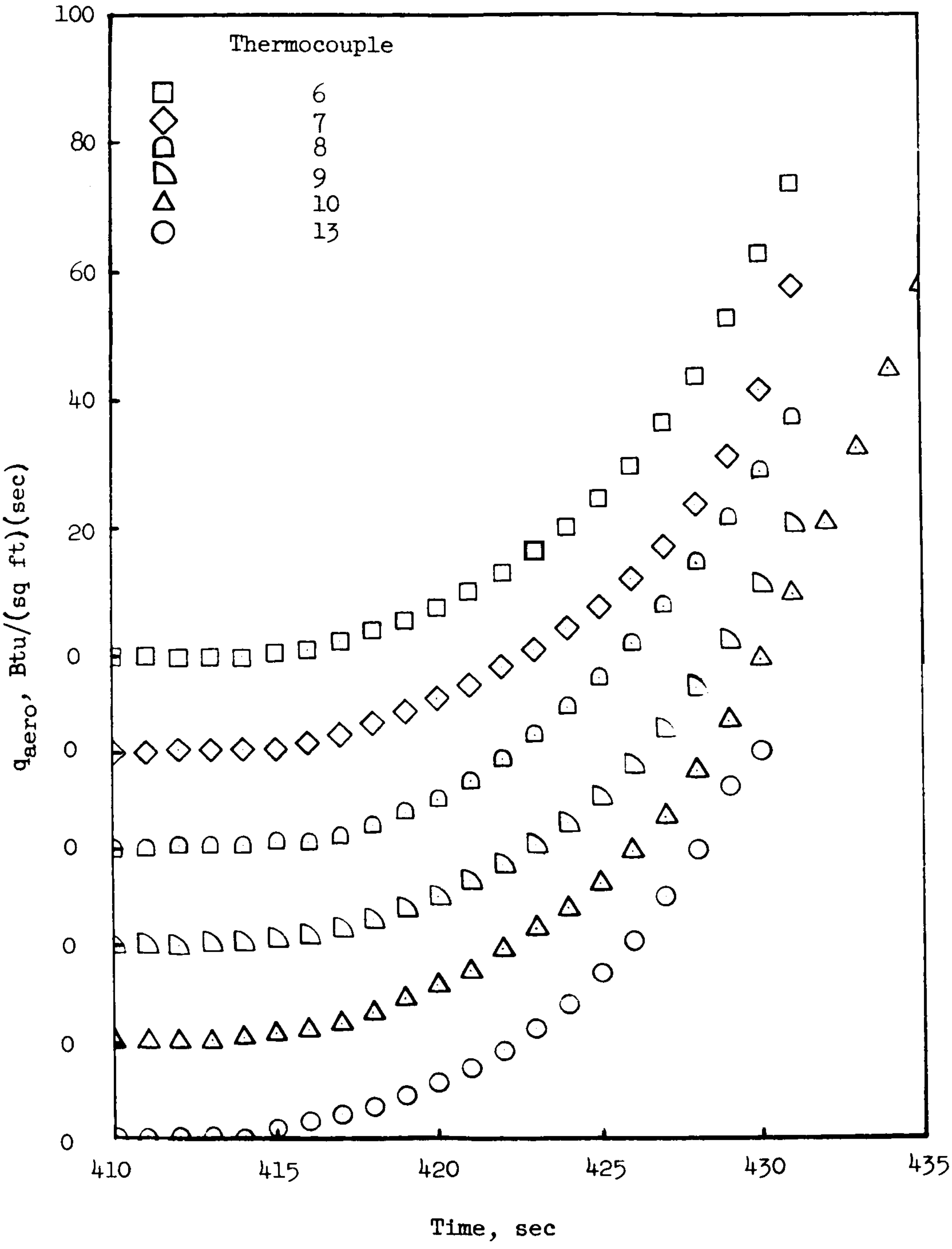

(a) Nose face locations.

Figure 24.- Flight test convective heating rate time histories.

[redacted]

[redacted]

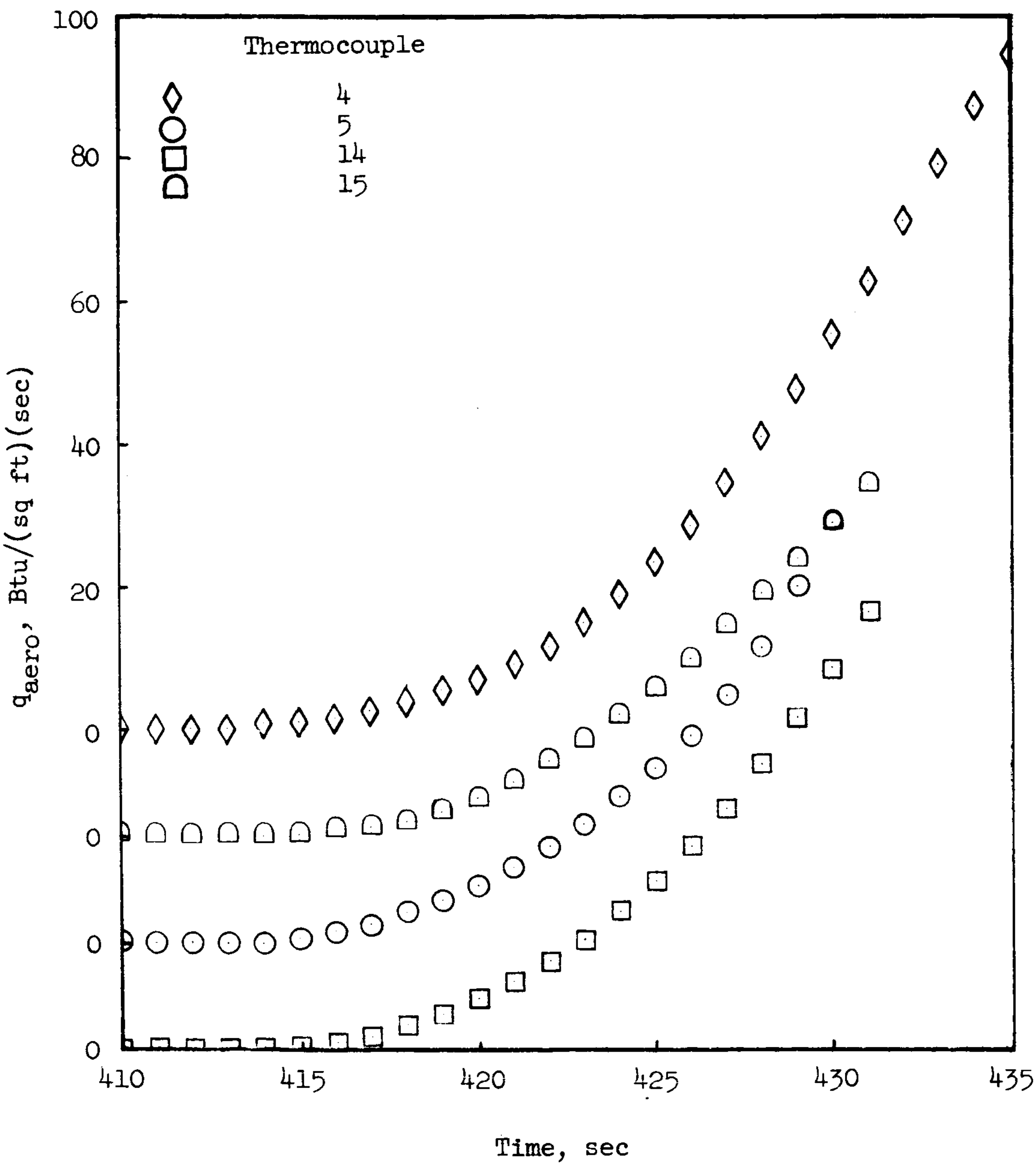

(b) Corner locations.

Figure 24.- Continued.

[redacted]

[redacted]

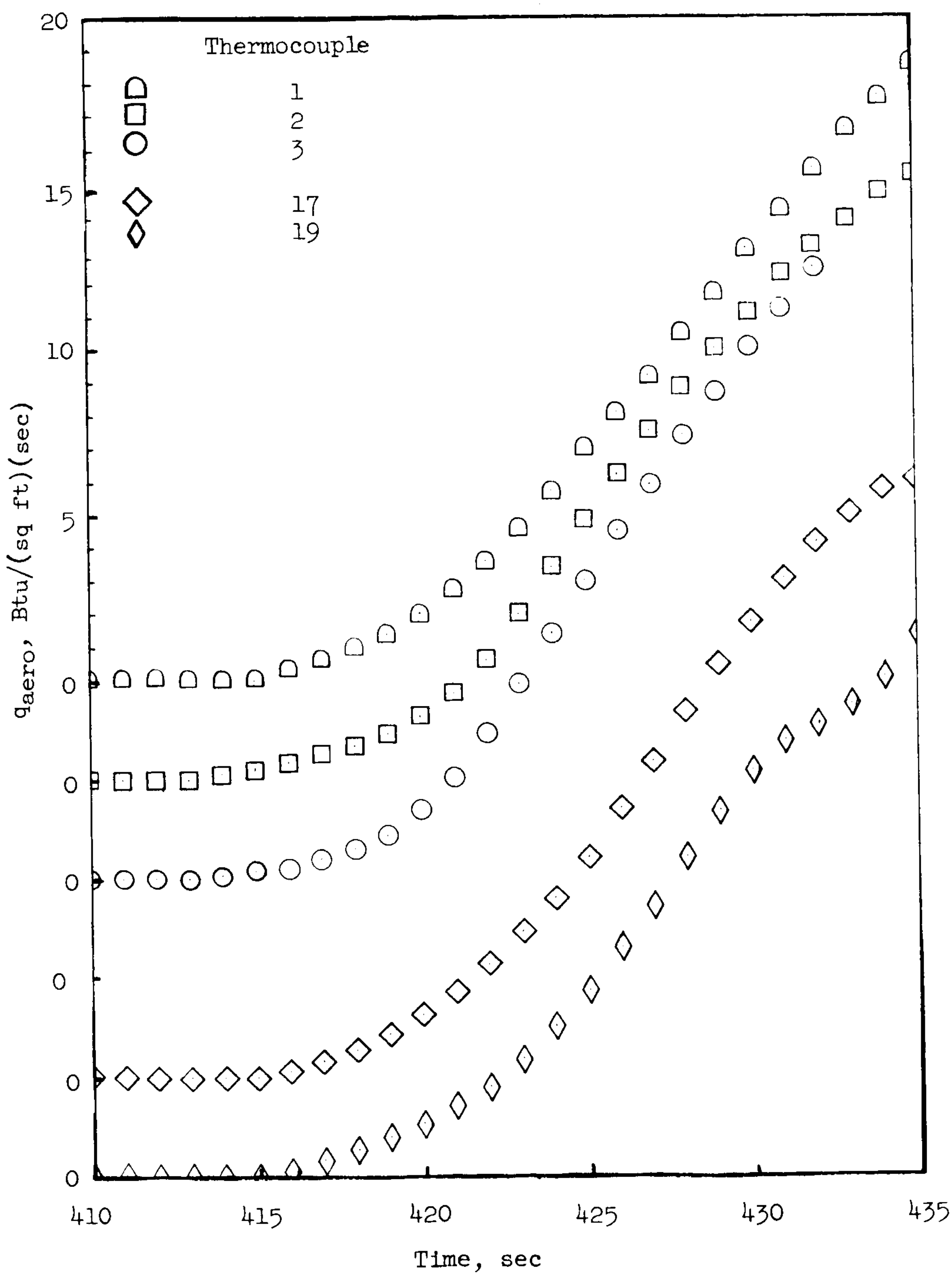

(c) Forebody locations.

Figure 24.- Concluded.

[redacted]

[redacted]

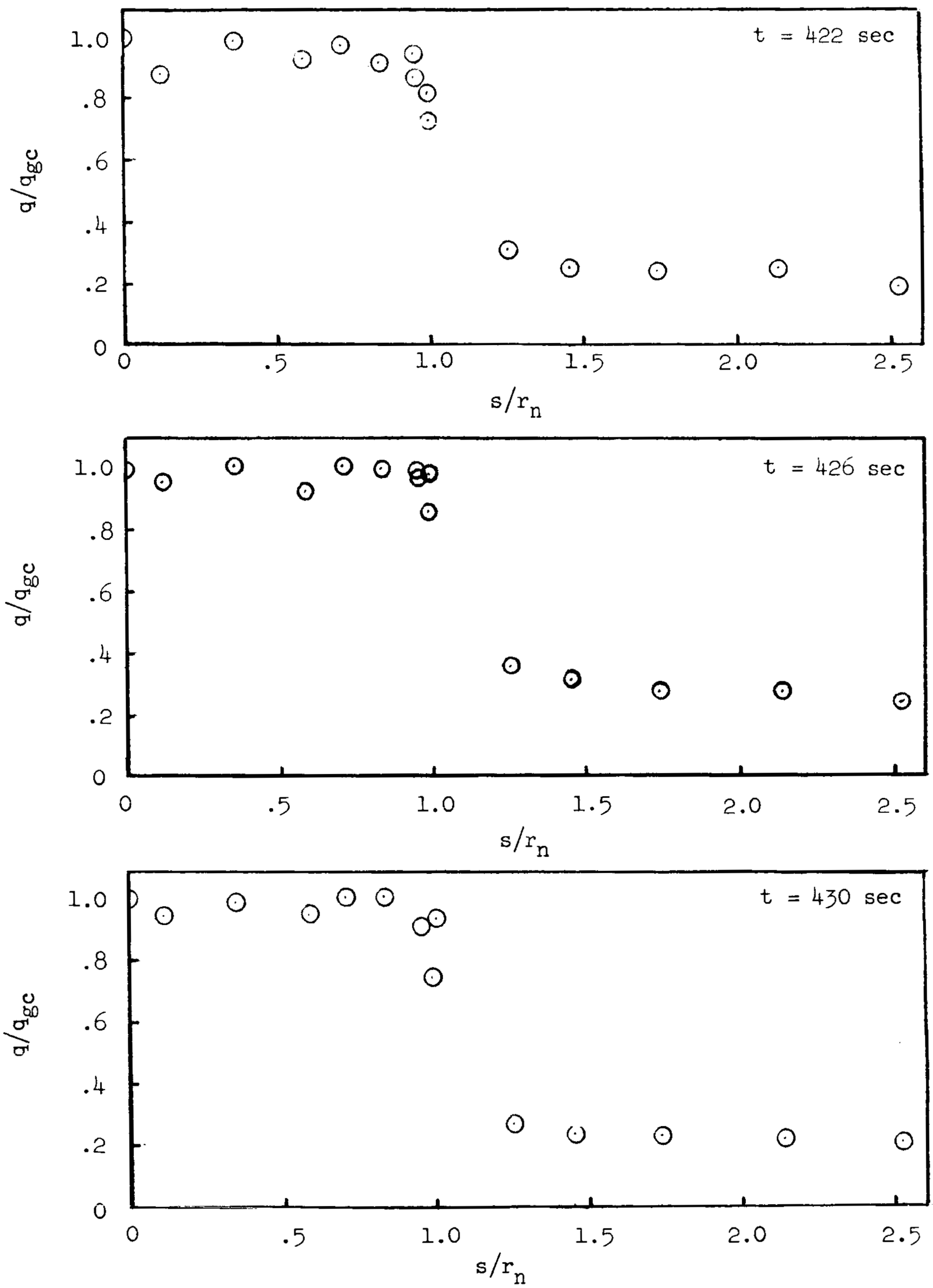

Figure 25.- Distribution of heating rates along inconel calorimeter.

[redacted]

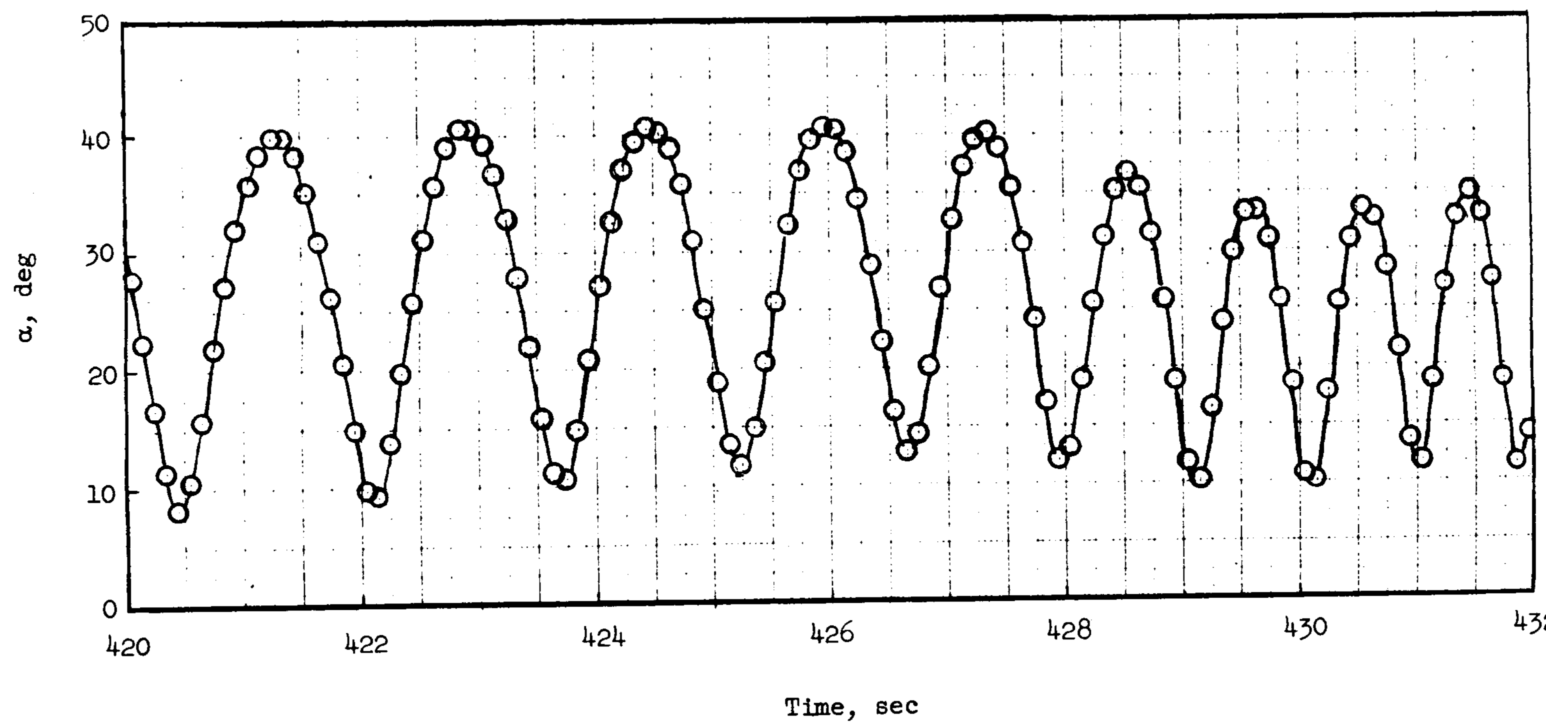

Figure 26.- Time history of angle of attack for flight payload.

[redacted]

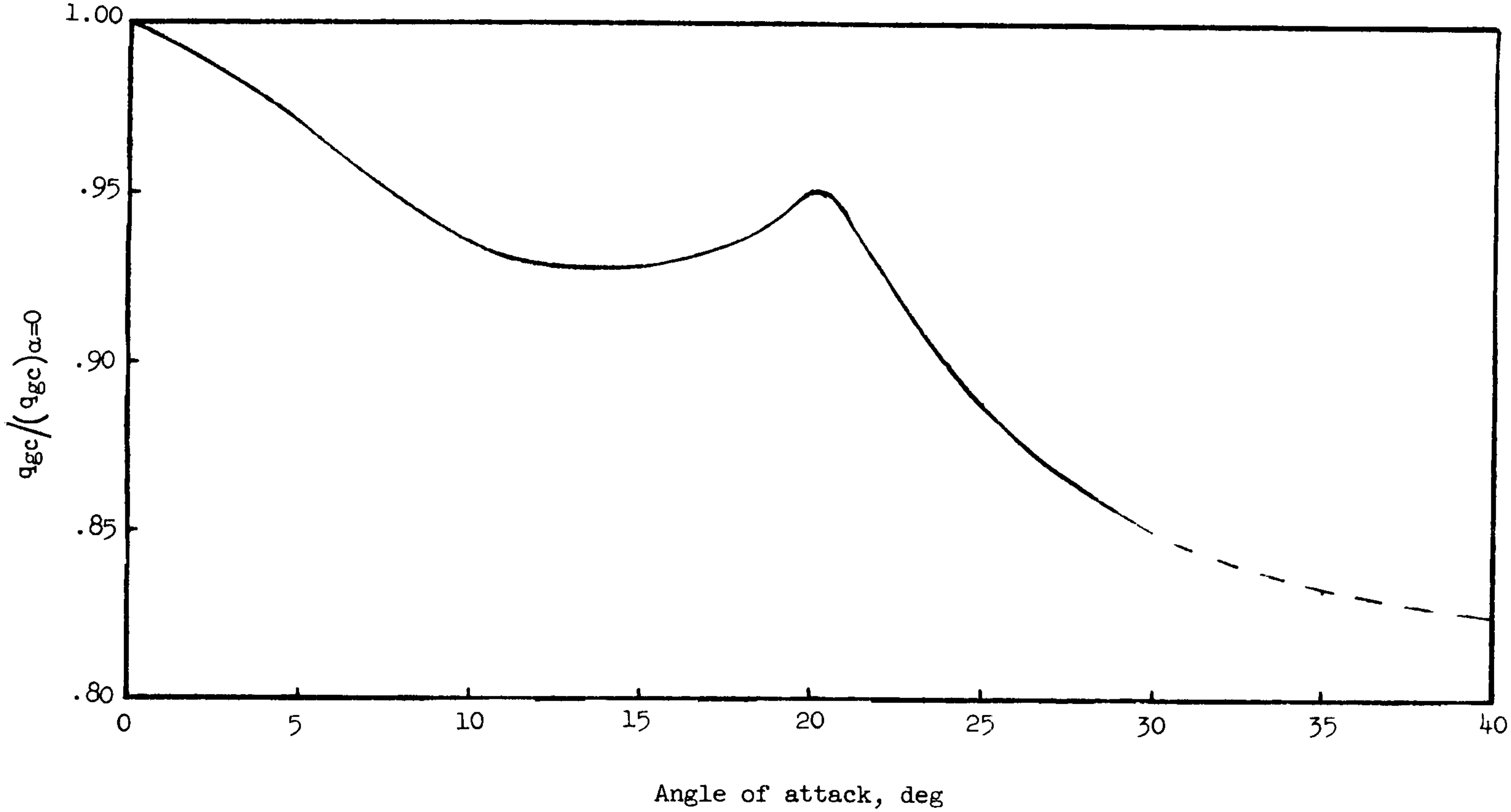

Figure 27.- Variation of nose heating with angle of attack.

[redacted]

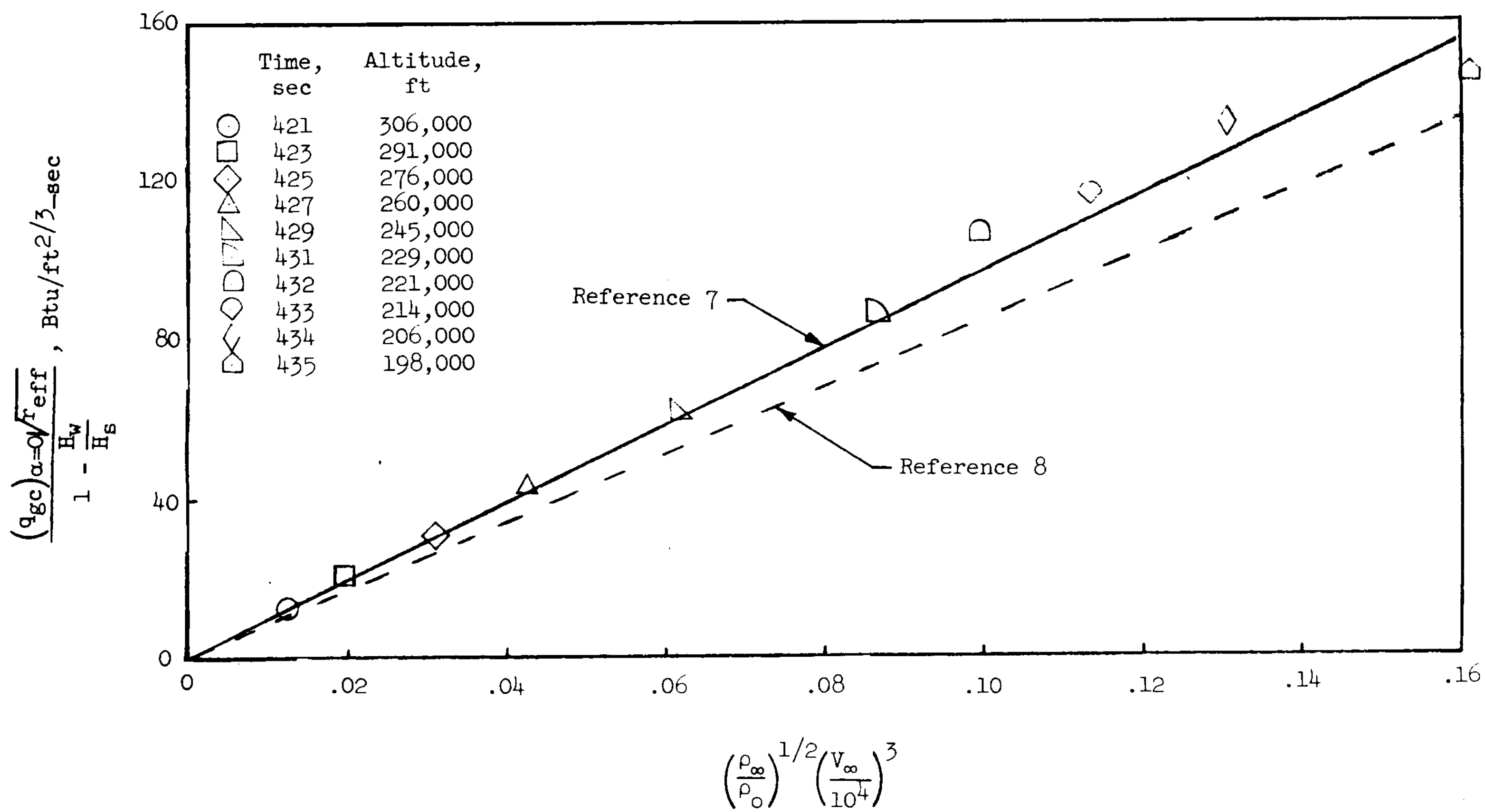

Figure 28.- Variation of aerodynamic stagnation point heating with density and velocity.

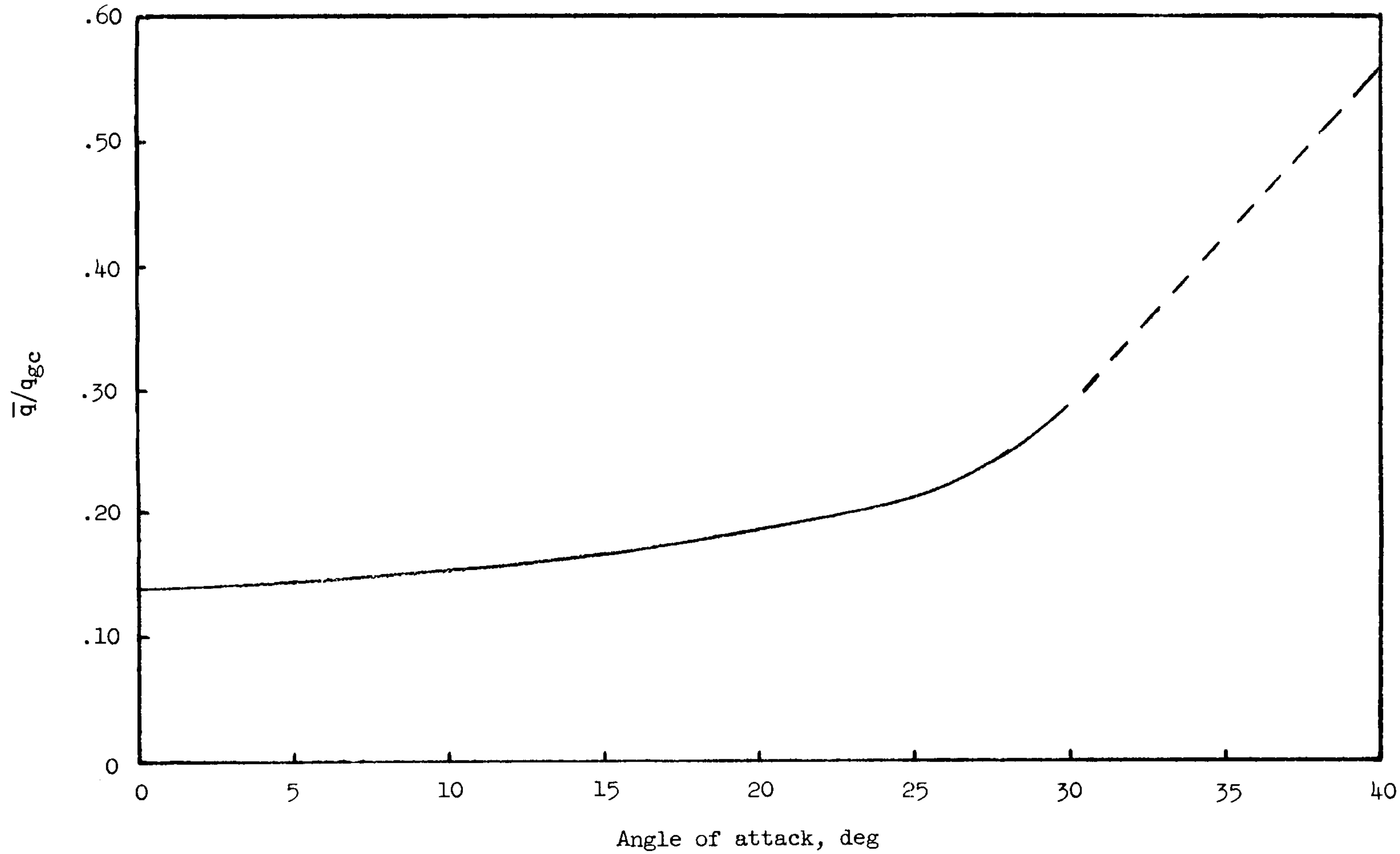

Figure 29.- Effect of angle of attack on average heat-transfer rate. $s/r_n = 2.1$.

[redacted]

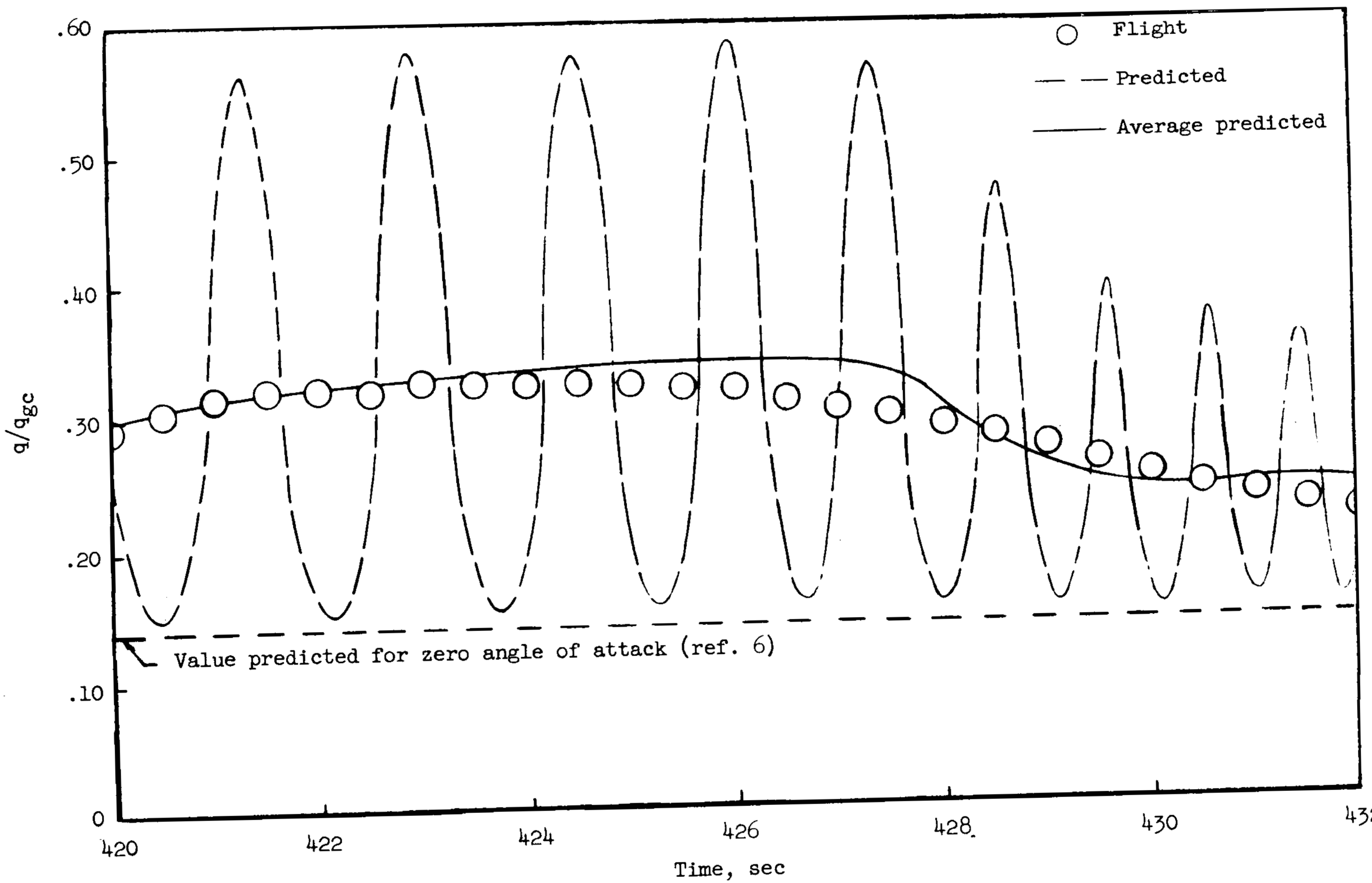

Figure 30.- Time history of forebody heating at location $s/r_n = 2.13$.

[redacted]

[redacted]

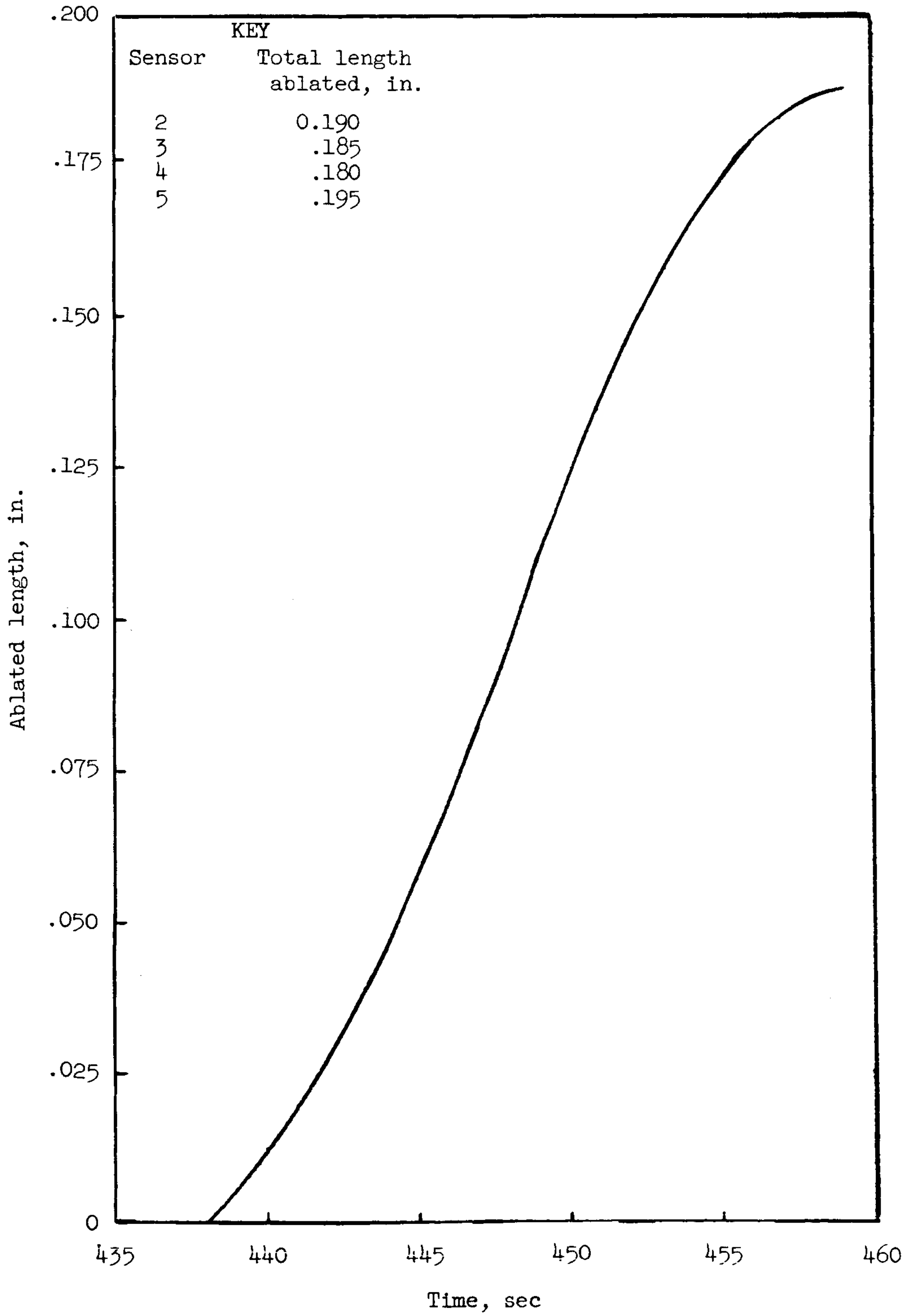

Figure 31.- Computed Teflon ablation variation with flight time for the geometric center point.

[redacted]

[redacted]

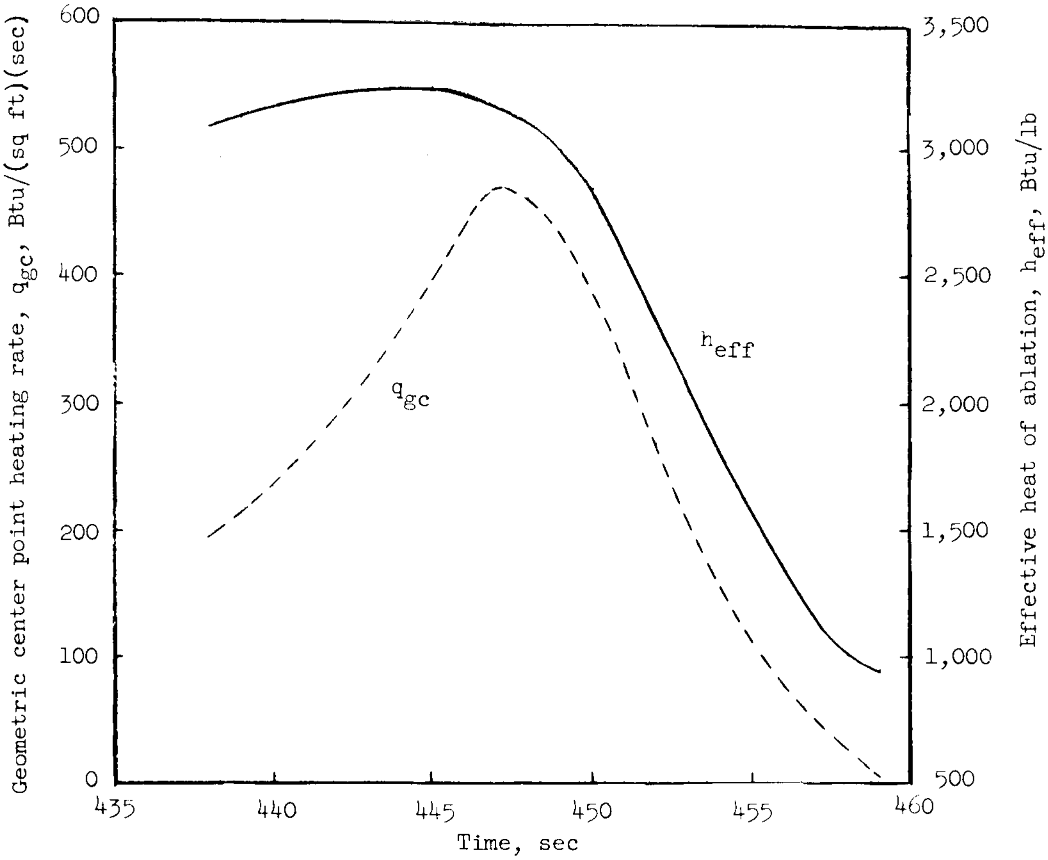

(a) Time histories of q_{gc} and h_{eff}.

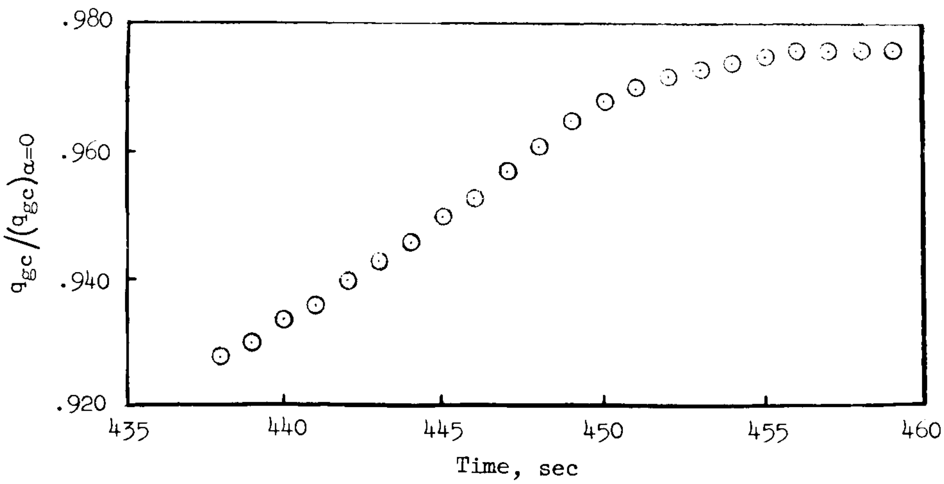

(b) Time history of $q_{gc}/(q_{gc})_{\alpha=0}$.

Figure 32.- Time histories of parameters used in ablation analysis.

[redacted]

[redacted]

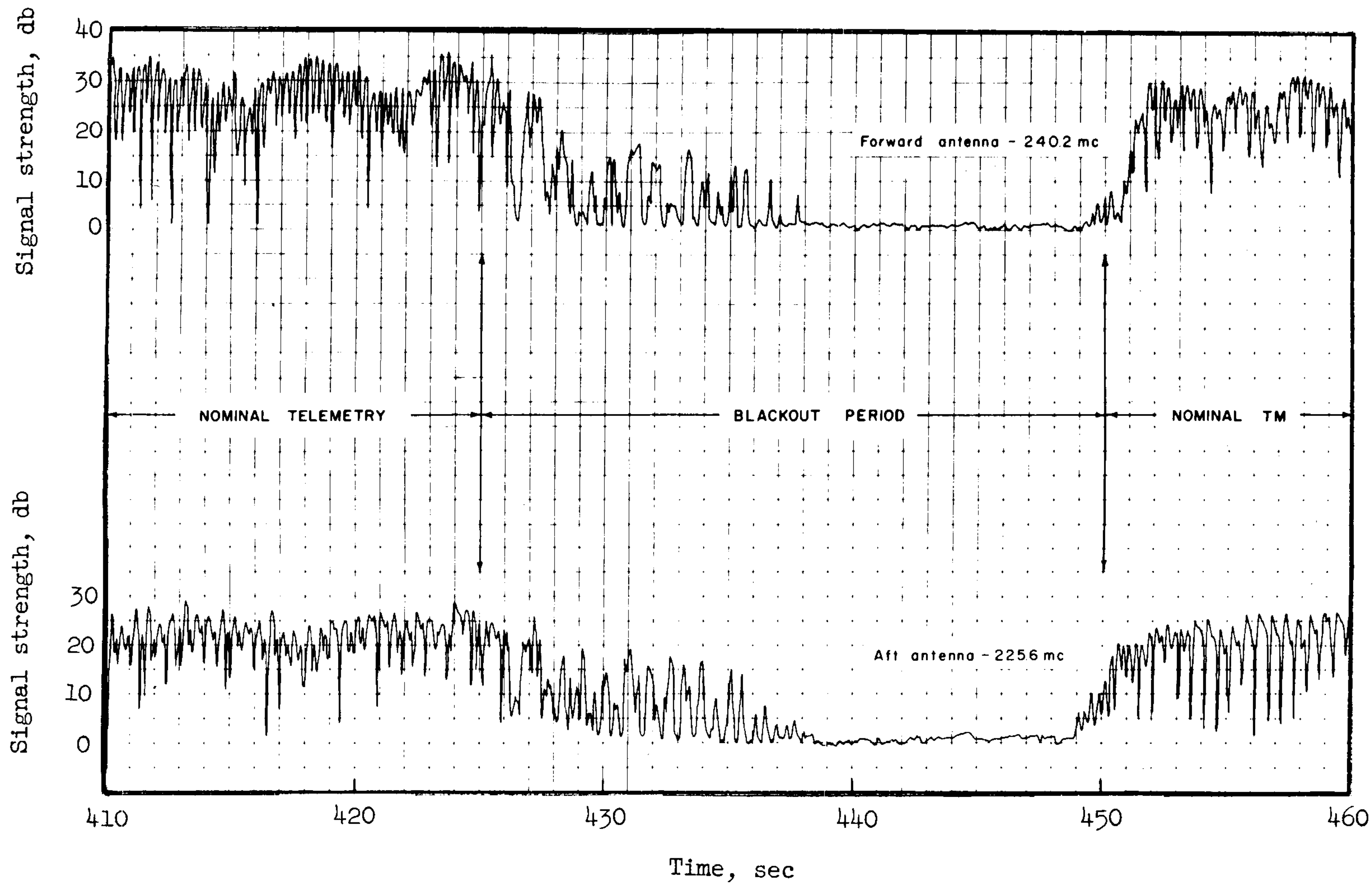

Figure 33.- Time histories of received signal strength.

[redacted]

[redacted]

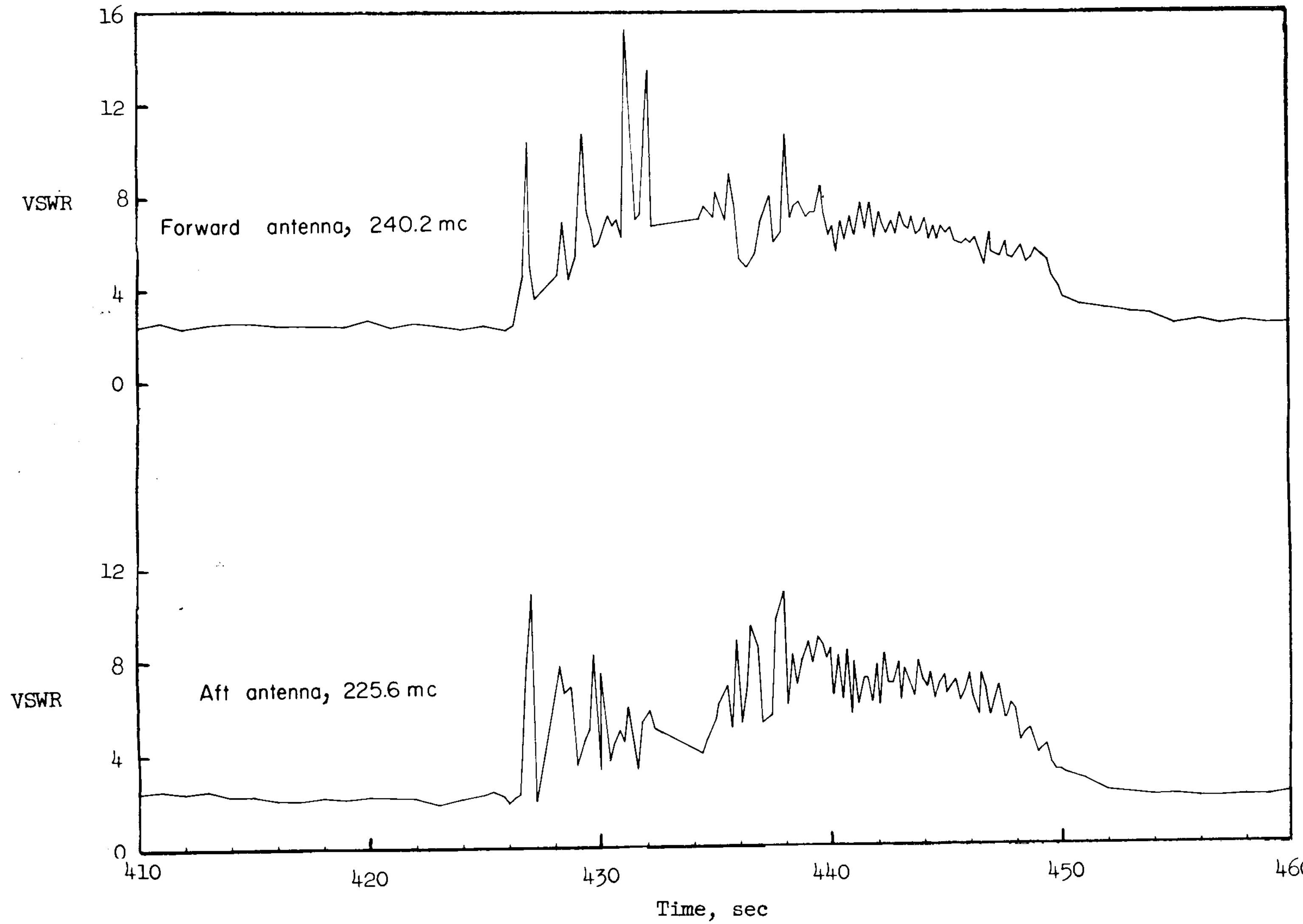

Figure 34.- Time histories of VSWR for the payload antennas.

[redacted]

NASA-Langley, 1964 L-3763